Exotic Resonances and Higgs Production at the LHC

Paul Mullen[1]

November 27, 2016

[1]Email:p.mullen@cern.ch

Declaration

I declare that the results presented here are my own work unless otherwise stated. This thesis is the result of research carried out as part of the Experimental Particle Physics group in the School of Physics & Astronomy within the University of Glasgow between October 2012 and April 2016. It has not been submitted as part of any other degree at the University of Glasgow or any other institution.

Acknowledgements

I would like to thank my supervisors Aidan Robson and Tony Doyle for their guidance and advice, the entire Experimental Particle Physics group at Glasgow as well as my colleagues at CERN. I would also like to thank my girlfriend Rebecca for putting up with my complaining.

Authors Contributions

Modern high energy physics experiments are collaborations between many people from a variety of countries around the world. Thus the work presented in this thesis relies on work done by many people. The contributions made by the author are described below:

- Chapter 5: The author performed the multijet modelling validation studies, impact parameter studies and generator comparison studies presented in this section.

- Chapter 6: The author performed the cut optimisation studies in the one lepton channel presented, helped to define the final selection, ran some early fit studies and produced the postfit plots shown in all three lepton channels.

The author also did some work in heavy flavour overlap removal in Monte Carlo generators as a service work task that is not presented in this thesis.

Contents

List of Figures

List of Tables

Sometimes science is more art than science. A lot of people don't get that.

Dr. Rick Sanchez

Part I

Chapter 1

Theory

This thesis concerns the search for the Higgs boson and other previously-unobserved heavy particles. The currently-known elementary particles and their interactions are described by the Standard Model, which is a quantum field theory containing electromagnetism, the weak force, and the strong force. The following sections will introduce the elementary particles, their interactions, and the need for spontaneous symmetry breaking in the theory.

1.1 The Elementary Particles

Particles in the Standard Model can be categorised as fermions or bosons. Fermions have half-integer spin, are described by Fermi-Dirac statistics, and constitute the matter particles. Bosons are mainly force-carrying particles (e.g. Higgs), have integer spin, and are described by Bose-Einstein statistics [19].

1.1.1 Fermions

Fermions are divided up into two groups: quarks, and leptons; each of which have three generations. Each generation of leptons comprises a doublet of a charged and neutral particle. The first generation is the electron and electron neutrino, the second generation is the muon and muon neutrino, and the third generation is the tau and tau neutrino. Each generation has a higher mass than the last and each particle also has a corresponding anti-particle with opposite charge. The first generation of quarks consists of the up with charge $\frac{2}{3}$ and the down with charge -$\frac{1}{3}$, the second generation consists of the strange and charm quarks with the same corresponding charges as the first, and the third generation consists of the bottom and top again with the same corresponding charges. As with the leptons, each particle has a corresponding anti-particle with opposite electric charge. Quarks also come with a "colour" with three possible values of red, green, and blue (and each colour also has a corresponding anti-colour) [19].

1.1.2 Bosons

Bosons mediate the four fundamental forces. Electromagnetism, which describes the interaction of electrically charged particles, is mediated by the photon. The strong nuclear force which is responsible for quark confinement is mediated by the gluon. The weak nuclear force which governs unstable particle decays is mediated by the W and Z bosons. Finally gravity is theorised to be governed by the graviton. A summary of all the known fundamental particles can be found in Table 1.1.

Name	Symbol	Charge	Mass
Fermions			
Quarks		$J^P = 1/2^+$	
Up	u	+2/3	2.3 MeV
Down	d	-1/3	4.8 MeV
Charm	c	+2/3	1.275 GeV
Strange	s	-1/3	95 MeV
Top	t	+2/3	173.21 GeV
Bottom	b	-1/3	4.18 GeV
Leptons		$J^P = 1/2^+$	
Electron	e	-1	0.511 MeV
Electron neutrino	ν_e	0	< 2 eV
Muon	μ	-1	105.65 MeV
Muon neutrino	ν_μ	0	< 2 eV
Tau	τ	-1	1776.82 MeV
Tau neutrino	ν_τ	0	< 2 eV
Bosons			
Vector		$J^P = 1^-$	
Gluon	g	0	0
Photon	γ	0	0
W boson	$W^\pm$	± 1	80.385 GeV
Z boson	Z^0	0	91.188 GeV
Scalar		$J^P = 0^+$	
Higgs boson	H	0	125.7 GeV

Table 1.1: Table of the standard model particles. J denotes the spin and P the parity. Values taken from [19]

1.2 The Standard Model

The Standard Model is based on the product of three gauge groups:

$$SU(3)_c \times SU(2)_L \times U(1)_Y \tag{1.1}$$

Gauge groups can be constructed from the principle of local gauge invariance and can be abelian (commutative algebra) or non-abelian (non-commutative). $SU(3)_c$, which describes QCD, and $SU(2)_L$, which describes the electroweak sector, are both non-abelian whereas $U(1)_Y$, which describes hypercharge, is abelian. Each theory is defined by a Lagrangian from which the equations of motion describing the properties and interactions of fundamental particles can be derived. No significant experimental deviation from theory predictions have been observed [21].

1.2.1 Quantum Electrodynamics

It is understood that a gauge invariance leads to a conservation law [22] and since charge is conserved in electromagnetism, demanding local gauge invariance can be used to embed this conservation into a field theory description of QED. Starting from the Dirac Lagrangian:

$$\mathcal{L} = i\bar{\psi}\gamma^{\mu}\partial_{\mu}\psi - m\bar{\psi}\psi\,, \tag{1.2}$$

and the definition of a local gauge transformation

$$\psi(x) \to \psi'(x) = e^{i\alpha(x)}\psi(x),\ \bar{\psi}(x) \to \bar{\psi}'(x) = e^{-i\alpha(x)}\bar{\psi}(x)\,, \tag{1.3}$$

it is trivial to show that the Lagrangian is not invariant under this transformation. To solve this problem a covariant derivative is defined

$$D_\mu = \partial_\mu + ieA_\mu \,, \tag{1.4}$$

where the addition of the local gauge field, A^μ that transforms as

$$A_\mu \to A'_\mu = A_\mu - \frac{1}{e}\partial_\mu \alpha(x) \tag{1.5}$$

gives a Lagrangian that is invariant under a local gauge transformation. The addition of a term describing the kinetic energy of the photon field gives the QED Lagrangian that describes the interactions of fermions mediated by the photon:

$$\mathcal{L} = -\frac{1}{4}F_{\mu\nu}F^{\mu\nu} + i\bar{\psi}\gamma^\mu D_\mu \psi - m\bar{\psi}\psi \,. \tag{1.6}$$

Using this Lagrangian and perturbation theory [23] a set of interactions can be derived. Since perturbation theory is a method for finding an approximate solution expressed as a power series the interactions calculated are always to a particular "order". The order describes the accuracy of the solution, which is a function of the number of terms in the series for which interactions are calculated. These interactions can be expressed using Feynman diagrams, which are a way of diagramatically expressing the terms in the series. For example, Figure 1.1 shows electron-electron scattering interaction mediated by a photon that corresponds to the term

$$\bar{\psi}(x)\gamma^\mu\psi(x)\bar{\psi}(x')\gamma^\nu\psi(x')A_\mu(x)A_\nu(x') \tag{1.7}$$

in the expansion of the Lagrangian [21].

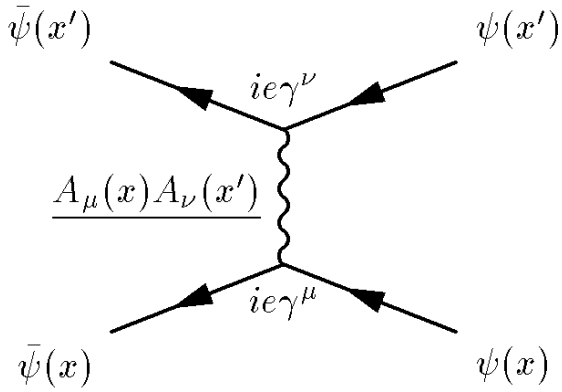

Figure 1.1: Feynman diagram of electron electron scattering being mediated by a photon. The terms from the perturbative expansion of the Lagrangian that correspond to lines and vertices are shown.

1.2.2 Quantum Chromodynamics

QCD describes the interaction of quarks and gluons. It is a non-abelian gauge theory of the group SU(N_c) where there are N_c^2-1 gluons. The Lagrangian is defined as:

$$\mathcal{L}_{QCD} = \bar{\psi}(i\gamma^{\mu}\partial_{\mu} - m)\psi + g_s(\bar{\psi}\gamma^{\mu}T_a\psi)G_{\mu}^{a} - \frac{1}{4}G_{\mu\nu}^{a}G_{a}^{\mu\nu} \tag{1.8}$$

where a represents the N_c^2-1 gauge group generators with $N_c = 3$ as has been observed experimentally (representing the number of colour charges), $\psi(x)$ is a triplet representing the three colour fields (red, green and blue), and $\bar{\psi}$ represents the anti-colours. $G_{\mu\nu}^{a}$ is the field strength tensor, that is a more complicated version of that used in QED in order to represent the self interaction present in gluons that is not present in photons due to the non-abelian nature.

The self interaction of gluons leads to an increase in coupling strength of the strong interaction as distance increases giving rise to the asymptotic freedom which prevents the observation of free quarks or gluons [21].

1.2.3 Electroweak Theory

The electroweak theory unifies the weak nuclear force and the electromagnetic force into one force described by an $SU(2)_L \times U(1)_Y$ gauge group. The Lagrangian is

$$\mathcal{L} = \sum_{l=e,\mu,\tau} \mathcal{L}(l) + \mathcal{L}_W + \mathcal{L}_B + \mathcal{L}(q)\,. \tag{1.9}$$

The first term describes the standard model leptons and the next two are the kinetic energy terms in the model for the four electroweak fields and the latter term describes the electroweak quark sector. The fermion interactions are expressed in the first term by constructing a weak isospin doublet with a left handed lepton and corresponding neutrino:

$$\chi_L = \begin{pmatrix} \nu_L \\ e_L \end{pmatrix}. \tag{1.10}$$

This is incorporated into a Lagrangian with a term of the form

$$\mathcal{L}(e) = \bar{\chi}_L \gamma^\mu [i\partial_\mu - g(\frac{1}{2})\vec{\tau}\cdot\vec{W}_\mu - \frac{g'}{2}(-1)B_\mu]\chi_L + \bar{e}_R\gamma^\mu[i\partial_\mu - \frac{g'}{2}(-2)B_\mu]e_R \tag{1.11}$$

for each fermion. This describes the interaction between the leptons and the gauge bosons, which are described by the W^i_μ and B_μ terms. The coupling parameters for these bosons are g and g' respectively and $\vec{\tau}$ are the Pauli matrices.

The second and third terms in the Lagrangian are the kinetic energy terms for the weak fields described by:

$$\mathcal{L}_B = -\frac{1}{4}B_{\mu\nu}B^{\mu\nu} \tag{1.12}$$

$$\mathcal{L}_W = -\frac{1}{4}\sum_i (W_{\mu\nu})^i (W^{\mu\nu})^i\,. \tag{1.13}$$

The four weak fields can be expressed in terms of the physical fields (the W and

Z bosons and the photon):

$$W_\mu^1 = \frac{1}{\sqrt{2}}(W_\mu^+ + W_\mu^-) \tag{1.14}$$

$$W_\mu^2 = \frac{i}{\sqrt{2}}(W_\mu^- - W_\mu^+) \tag{1.15}$$

$$W_\mu^3 = \cos\theta_\omega Z_\mu + \sin\theta_\omega A_\mu \tag{1.16}$$

$$B_\mu = \cos\theta_\omega A_\mu - \sin\theta_\omega Z_\mu \,. \tag{1.17}$$

The quark sector is also constructed using an isospin double analogous to the lepton case of the form

$$\chi_L = \begin{pmatrix} U_f \\ D'_f \end{pmatrix}. \tag{1.18}$$

where f represents the three generations of quarks and D'_f is a flavour rotation matrix of the form

$$D'_f = \sum_{f'=1,2,3} V_{ff'} D_{f'} \,. \tag{1.19}$$

Here V is the CKM matrix that controls the mixing of the quark flavour eigenstates and a Lagrangian of the form

$$\begin{aligned} \mathcal{L}(q) = & \sum_{f'=1,2,3} \bar{\chi}_L^f \gamma^\mu [i\partial_\mu - \frac{1}{2}\vec{\tau}\cdot\vec{W}_\mu - \frac{1}{3}B_\mu]\chi_L^f \\ & + \bar{U}_{fR}\gamma^\mu [i\partial_\mu - \frac{g'}{2}\left(\frac{4}{3}\right)B_\mu]U_{fR} \\ & + \bar{D}_{fR}\gamma^\mu [i\partial_\mu - \frac{g'}{2}\left(\frac{-2}{3}\right)B_\mu]D_{fR} \end{aligned} \tag{1.20}$$

is derived.

Note that adding an explicit term giving masses to the weak fields to the Lagrangian would break local gauge invariance. Similarly a Dirac mass term for the leptons would also break local gauge invariance due to the different gauge transformations of the left and right handed components. In order to give mass to the bosons of the weak force, a method of breaking a local gauge symmetry called spontaneous symmetry breaking can be used [21].

1.2.4 Higgs Mechanism

The Higgs mechanism is an example of spontaneous symmetry breaking where a system has a symmetry that is maintained above some critical point but is no longer valid below this point. A simple example of this is a ferromagnet which has no overall magnetism above a certain temperature and thus has invariance under a rotation, but below that temperature a spontaneous magnetic alignment occurs breaking the rotational symmetry. The Higgs mechanism plays a similar role in breaking a symmetry in the electroweak theory in order to give mass to the weak bosons.

The Higgs mechanism modifies the electroweak Lagrangian by adding a doublet of complex scalar Higgs fields:

$$\Phi = \begin{pmatrix} \phi^+ \\ \phi^0 \end{pmatrix}. \tag{1.21}$$

The effect of this addition on the scalar potential of the form

$$V(\Phi) = \mu^2(\Phi^\dagger\Phi) - \lambda(\Phi^\dagger\Phi)^2 \tag{1.22}$$

means that for a choice of $\mu^2 < 0$ and $\lambda < 0$, the potential takes on the shape of a wine bottle with a number of degenerate minima in ϕ space. Choosing a value in ϕ space that is one of these degenerate minima gives a non-zero vacuum expectation value (vev). Applying a non-zero vev and making a choice of gauge results in a Lagrangian of the form:

$$\begin{aligned}\mathcal{L} = &\frac{1}{2}\partial_\mu H \partial^\mu H + \frac{1}{4}g^2(H^2 + 2\nu H + \nu^2)W^+_\mu W^{-\mu} \\ &+ \frac{1}{8}(g^2 + g'^2)(H^2 + 2\nu H + \nu^2)Z_\nu Z^\nu \\ &+ \mu^2 H^2 + \frac{\lambda}{4}(H^4 + 4\nu H^3)\,,\end{aligned} \tag{1.23}$$

where v is the vacuum expectation value and H is the Higgs field. This contains mass terms for the previously massless vector bosons [21] which are the terms containing only the vev, coupling constant and boson field. This gives the masses of the electroweak bosons to be:

$$M_W = \frac{1}{2}g\nu \tag{1.24}$$

$$M_Z = \frac{1}{2}(g^2 + g'^2)^{\frac{1}{2}}\nu\,. \tag{1.25}$$

1.3 Heavy Vector Triplet Model

There are many extensions to the Standard Model that have been proposed by the theory community. Many of these aim to solve the hierarchy problem, the question of why the Higgs mass is so much smaller than the Planck mass. The mass of the Higgs field receives radiative corrections that require large fine tuning to give the observed Higgs mass [21]. One solution to this problem is supersym-

metry which introduces additional contributions to the Higgs mass which remove the need to fine tune the radiative corrections. Another solution is that used in composite Higgs models and others. These propose that the Higgs is not a fundamental particle but a bound state of a new strong interaction and predict the existence of additional high mass resonances [24].

In order to ease comparison of these composite Higgs type models to data produced at the LHC, attempts have been made to describe classes of models with a simplified Lagrangian that can be used to compare many models. The Heavy Vector Triplet (HVT) theory is one such approach. It consists of two models, A and B. Model A is an extended gauge symmetry model that describes weakly coupled extensions to the standard model, and model B describes a minimal composite Higgs model that is a strongly coupled, composite Higgs extension. Both models predict extra heavy spin 1 particles and the only free parameters in these models are the resonance mass, M_V and the resonance coupling, g_V [25].

1.4 Proton-Proton Collisions

Protons consist of valence and sea quarks. Valence quarks give the quantum numbers to hadrons. For example the proton has 3 valence quarks: two up and one down. Sea quarks are virtual particles produced in pairs when a gluon splits; they have very short lifetimes before annihilating. The constant flux of creation and annihilation is the quark sea. When proton bunches collide at a hadron collider the interaction between the quarks and gluons produces both low momentum (soft) and high momentum (hard) interactions. An illustration of these collisions is shown in Figure 1.2. Hard interactions can be simulated using perturbative QCD because the coupling constant is small enough that higher

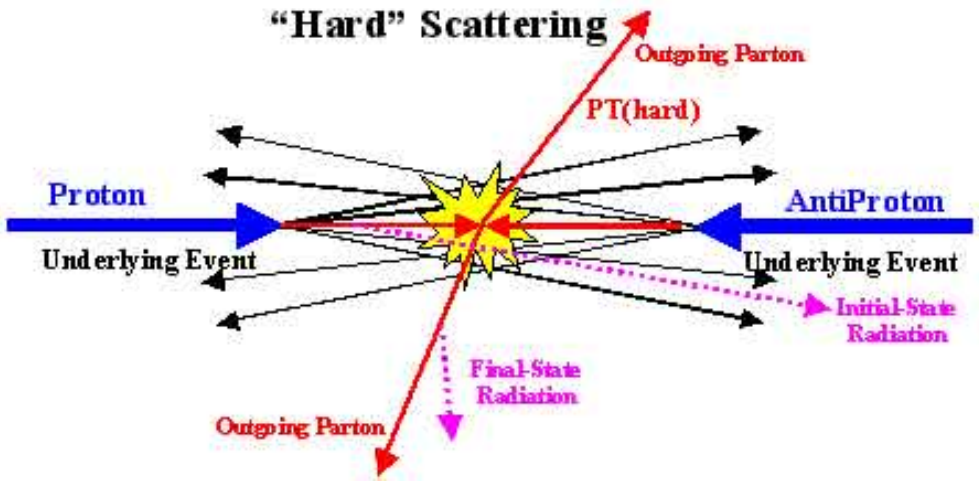

Figure 1.2: Illustration of a proton-proton collision and the various types of radiation produced. Initial state radiation (ISR) is the radiation of quarks or gluons before the hard scatter. Final state radiation (FSR) is radiation from the outgoing partons after the hard scatter and underlying event (UE) is the remnants of the collision not coming from the hard scatter.

order terms in a perturbative expansion have progressively smaller contributions, allowing an accurate approximation to be calculated using a small number of terms. This is not the case for the soft interactions as the QCD coupling constant increases at low energies. The factorisation [26] theorem allows these two cases to be separately calculated. The following equation can be used to calculate the scattering cross-section for a collision between two protons A and B:

$$d\sigma_{AB} = \sum_{AB} \int dx_1 dx_2 f_{a/A}(x_1, \mu_F^2) f_{b/B}(x_2, \mu_F^2) \hat{\sigma}_{ab}(\hat{s}, \mu_F^2, \mu_R^2)\,. \tag{1.26}$$

$\hat{\sigma}_{ab}$ is the perturbative cross-section for a particular process to some final state of interest whereas $f_{a/A}$ and $f_{b/B}$ are parton distribution function (PDFs) used to calculate the non-perturbative, soft contribution and are dependent on the parton momentum fractions x_1 and x_2. μ_F and μ_R are the factorisation and renormalisation scales [27].

1.5 Monte Carlo Event Simulation And Generators

The generation of Monte Carlo pseudodata proceeds in two stages. The first stage randomly samples the phase space of all possible feynman diagrams. This is the matrix element (ME) part of the Monte Carlo simulation. The second part is the parton showering, which simulates higher order corrections to the ME using a probabilistic splitting method called the DGLAP equations to simulate quark and gluon emissions.

There is some overlap between the processes simulated by these two stages that if not addressed can lead to double counting of events. This removal is done in a variety of ways; usually by using the small angle emissions from the parton shower and the wider angle emissions from the matrix element [28].

The effect of pileup, soft radiation background from collisions other than the hard scatter, is also applied to MC simulations and is discussed in section 3.1.

A variety of Monte Carlo generators are used at the LHC. These generators are either leading order (LO) or next to leading order (NLO). Generators are further divided into what part of the simulation they perform. Some only carry out the ME calculation, others the showering step (PS) and some carry out both. Generators that only carry out one step can be interfaced to another to perform the full simulation. A summary of generators can be found in Table 1.2.

Generator	Order	Simulation
Herwig	LO	PS
Pythia	LO	PS
Alpgen	LO	ME
Sherpa	LO	ME+PS
MadGraph5	NLO	ME
Powheg	NLO	ME
aMC@NLO	NLO	ME

Table 1.2: Table of Monte Carlo generators showing the order to which the calculations are carried out and which part of the simulation the generator performs. LO is leading order, NLO is next to leading order. ME is matrix element and PS is parton shower.

Chapter 2

Higgs Experimental Results

The Higgs boson was discovered by the ATLAS and CMS collaborations in 2012 with a mass of 125 GeV [29]. This section discusses the expected production and decay modes of the Higgs boson at the LHC and previous experimental observations.

2.1 Higgs Production Modes

At the LHC there are many production modes for the Higgs boson. Figure 2.1 shows the production cross-sections for the most common production processes at the LHC at 14 TeV for the possible Higgs masses. The four most dominant production methods are ggF, VBF, VH and ttH. Feynman diagrams for each of these processes are shown in Figure 2.2.

2.2 Higgs Decay Modes

The Higgs boson can decay in many ways. Figure 2.3 shows the branching ratios as a function of the Higgs mass. For a mass of 125 GeV the most common

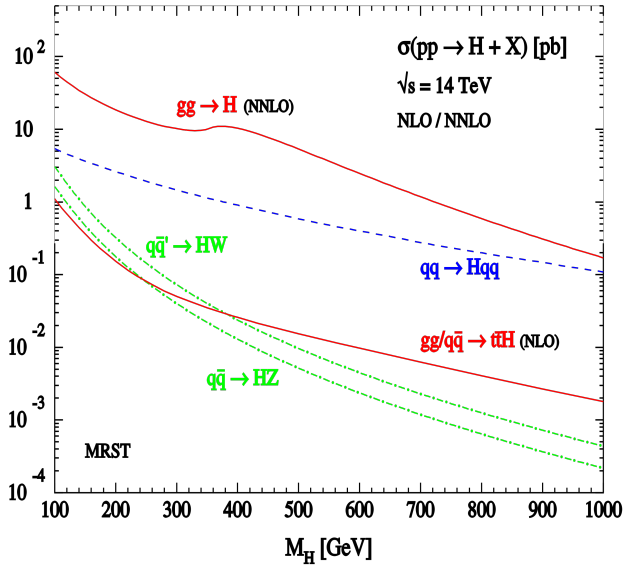

Figure 2.1: Standard model Higgs boson production cross section at the LHC as a function of Higgs mass taken from [1].

decay mode is to $b\bar{b}$, however this is a difficult process to observe at a hadron collider. This is because when colliding protons a large number of hadrons are produced which are not from the decay of a Higgs boson but which are difficult to distinguish from this signal process. Other Higgs decay processes include pairs of vector bosons and pairs of photons. Lepton and photon final states are easier to observe because the hadronic backgrounds are easier to distinguish from these signatures.

2.3 Higgs Experimental Results

The ATLAS and CMS collaborations announced the discovery of a new particle believed to be the Higgs boson with a mass of 125 GeV using data at both $\sqrt{s} =$ 7 and 8 TeV. The discovery was made in the $\gamma\gamma$ and ZZ channels. By the end of Run 1 the Higgs decaying to WW had been observed as well as strong evidence

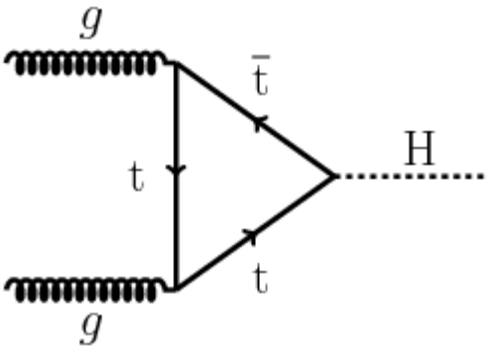

(a) Higgs production via gluon gluon fusion (ggF)

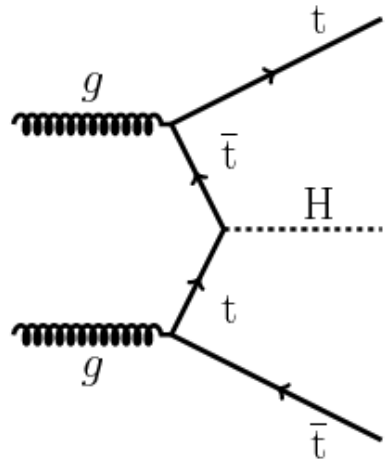

(b) Higgs production via top quarks (ttH)

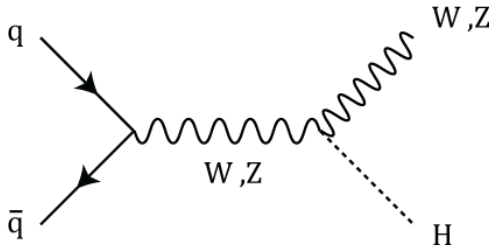

(c) Higgs production with and associated vector boson (VH)

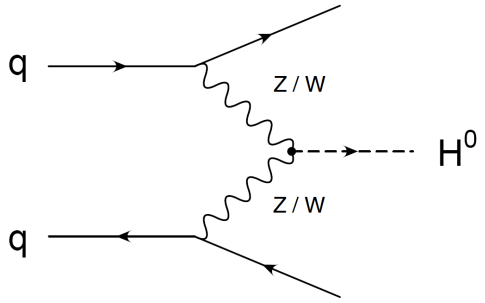

(d) Higgs production via vector boson fusion (VBF)

Figure 2.2: Leading order Higgs production mechanisms

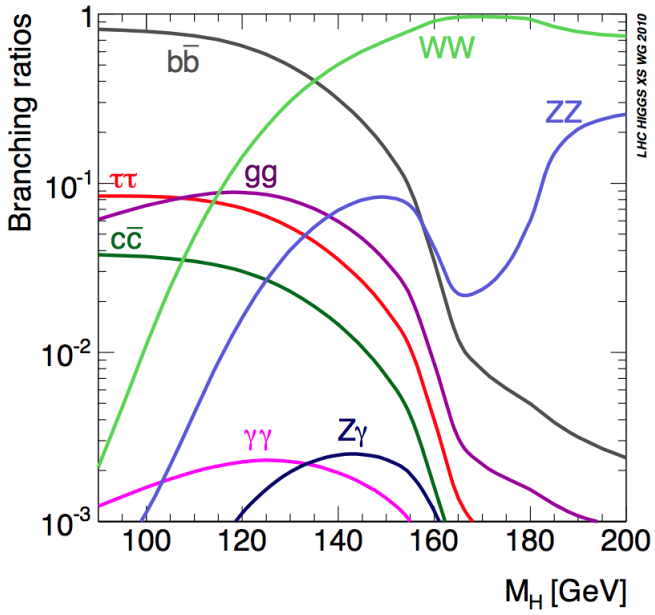

Figure 2.3: Standard model Higgs boson branching ratios as a function of Higgs mass taken from [2].

for decaying to $\tau\tau$. The combination of the $\gamma\gamma$ and ZZ results yields a mass of 125.09 $\pm$ 0.21 (stat) $\pm$ 0.11 (syst) GeV and spin of $J^P = 0^+$, consistent with the expected properties of the Higgs boson [30, 31, 32].

There has as of yet been no observation of the Higgs boson decaying to $b\bar{b}$ however by using the VH production mechanism, the large hadronic background can be supressed by requiring that the W/Z boson decays leptonically. A search using the VH production mechanism is presented in chapter 5 and a similar analysis searching for a BSM resonance that produces the same final state is presented in chapter 6.

2.4 VH Resonances Experimental Results

Both ATLAS and CMS carried out searches for heavy resonances using the Run 1 dataset. The results from the ATLAS search are shown in Figure 2.4. The

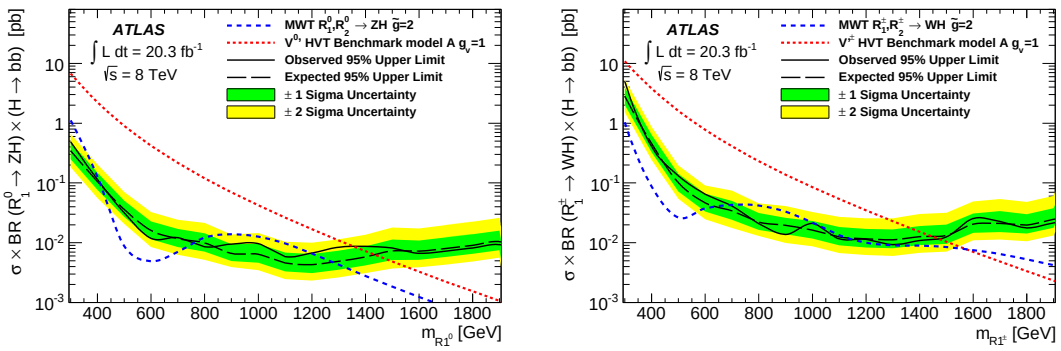

Figure 2.4: 95% CL upper limits on the production cross section time branching fraction to VH and H to $b\bar{b}$. Overlayed are the HVT and minimal walking technicolor (MWT) theory curves. The limits are shown for the neutral (left) and the charged (right) resonances

benchmark HVT model is excluded below a resonance mass of 1360 GeV in the neutral boson case and below 1470 GeV for the charged resonance [33]. The production cross section that is excluded in this analysis starts to rise in the region of 1 TeV suggesting that improvements could be made at high masses using boosted analyses techniques discussed in chapter 4.

The Run 1 CMS search made use of boosted techniques to improve the search sensitivity at high masses. Figure 2.5 shows the combined limits for the electron and muon channels. The HVT model is excluded up to a resonance mass of 1500 GeV but a small excess is observed at a mass of 1800 GeV with a global significance of 1.9 standard deviations [34]. This excess at high mass is of interest at Run 2. This is demonstrated in Figure 2.6 which shows how the ratio of parton luminosities against particle mass changes between 8 TeV and 13 TeV. It rises sharply for massive particles suggesting that analyses focusing on high mass resonances can produce interesting results early in Run 2.

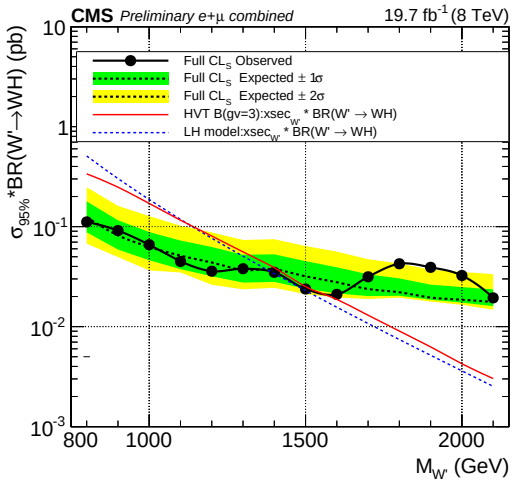

Figure 2.5: Observed (solid) and expected (dashed) 95% CL upper limits on the charged HVT resonance (W') production cross section times branching fraction to WH. Overlayed is the HVT model and Little Higgs model scenarios.

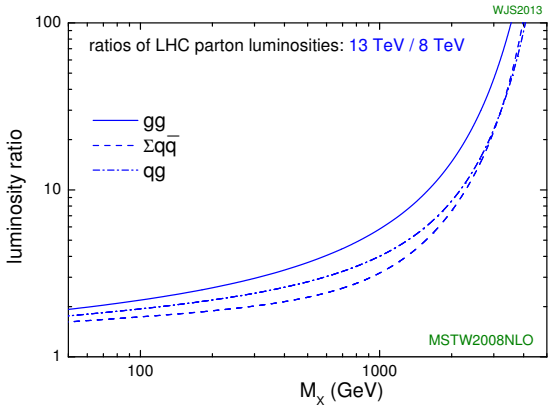

Figure 2.6: Ratio of 13 TeV and 8 TeV parton luminosities taken from [3]. For further details on this see [4].

Part II

Chapter 3

Experimental Apparatus

3.1 The LHC

The Large Hadron Collider is a particle collider located at the CERN site under the French-Swiss border near Geneva. It is installed in a tunnel of circumference ∼27 km which was previously occupied by the Large Electron Positron (LEP) collider.

A diagram of the injector chain is shown in Figure 3.1. Protons start in the Linac 2 linear accelerator, go to the proton Booster, then to the Proton Synchrotron, the Super Proton Synchrotron and from there into the LHC ring itself. This design allows for the energy of the protons to be increased at each step of the chain until they reach the final collision energy. For proton-proton collisions the centre of mass energy was 7 TeV in 2011 and 8 TeV in 2012. At the end of 2012 collisions were stopped and detectors upgraded. Collisions were restarted in 2015 and the energy was increased to 13 TeV and is planned to increase to 14 TeV. The first period of data taking (from 2009 to 2012) is referred to as Run 1, and the second run 2. The LHC also collides lead ions but those experiments are

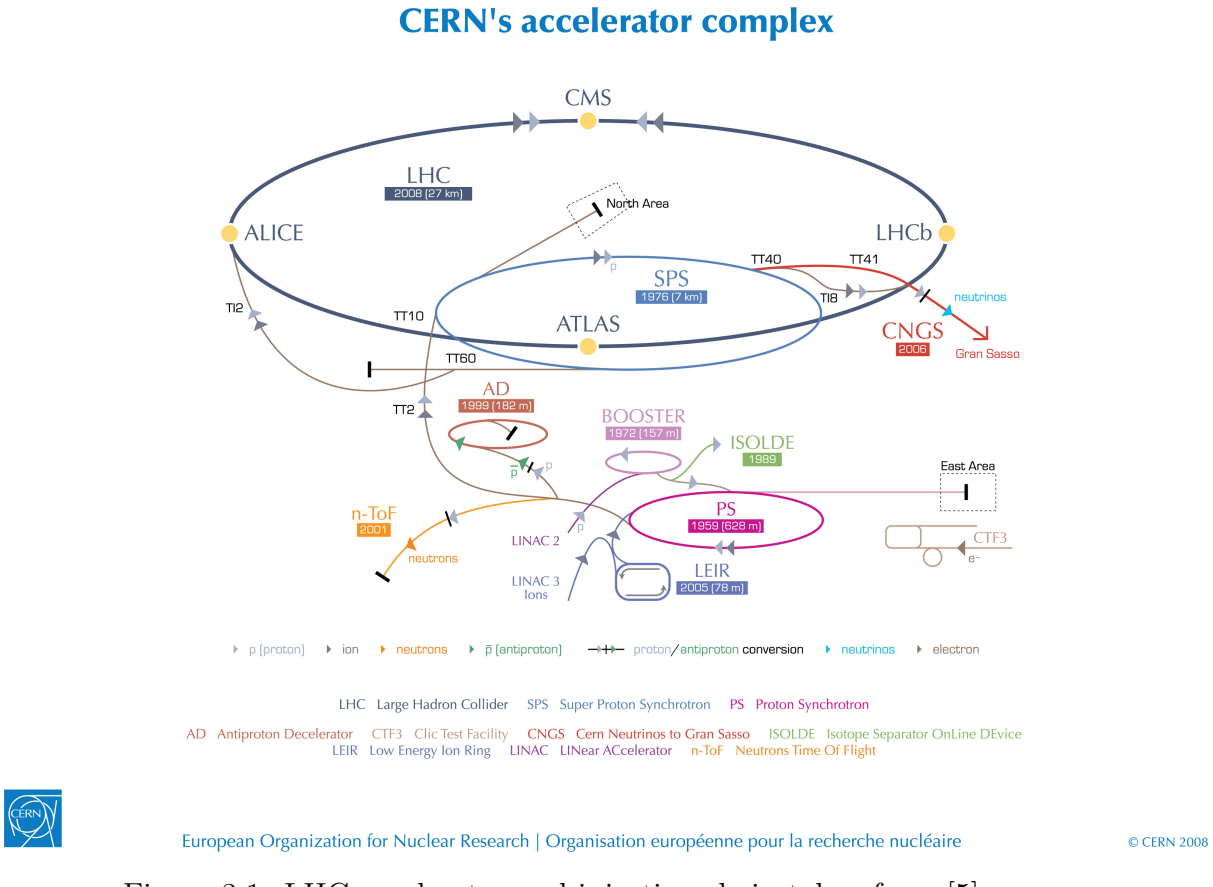

Figure 3.1: LHC accelerator and injection chain taken from [5]

not the subject of this thesis.

The beams are circulated in two beam pipes which are housed in superconducting magnets kept at a temperature of ∼1.9 K that provide a field of 8.33 T. The magnets are used to direct and focus the beams.

On the LHC ring there are four interaction points with a detector at each. ATLAS and CMS are the general purpose detectors primarily designed for proton-proton collisions and are used to investigate Higgs physics and to search for physics beyond the standard model, among other areas. The LHCb experiment is designed for investigating flavour physics. The ALICE experiment is designed for investigating lead ion collisions.

For physics analysis it is important to know the integrated luminosity. The

instantaneous luminosity can be calculated as

$$\mathcal{L} = \frac{N^2 k_b f \gamma}{4\pi^2 \sigma^2} F \,, \tag{3.1}$$

where N is the number of protons per bunch, k_b is the number of bunches, f is the revolution frequency, γ is the relativistic factor, σ is the bunch cross section, and F is the reduction factor caused by the crossing angle. As given by Equation 3.1 the instantaneous luminosity can be increased or decreased by tweaking the various parameters [35]. The integrated luminosity can be calculated as

$$L = \int \mathcal{L} \cdot dt \,. \tag{3.2}$$

The accumulation of integrated luminosity for Run 1 is shown in Figure 3.2. In 2011 the total delivered to ATLAS was 5.43 fb^{-1}. For 2012 the energy was increased to 8 TeV, the number of particles per bunch crossing was increased, and ϵ_n and β^* were decreased in order to increase the instantaneous luminosity. This led to an increase in the total integrated luminosity provided to ATLAS of 22.8 fb^{-1} [6].

A similar luminosity plot is shown in Figure 3.3 for Run 2. The bunch spacing was reduced from 50 ns used in Run 1 to 25 ns [7].

A challenge at hadron colliders is dealing with pileup. Pileup is divided into two types: in-time, and out-of-time. In-time pileup refers to multiple interactions in a bunch crossing producing soft radiation that is absorbed by the detector alongside particles produced by the hard scatter. Out-of-time pileup is caused by particles produced in a bunch crossing not having cleared the detector before the next collision occurs. Both of these have the effect of adding additional soft

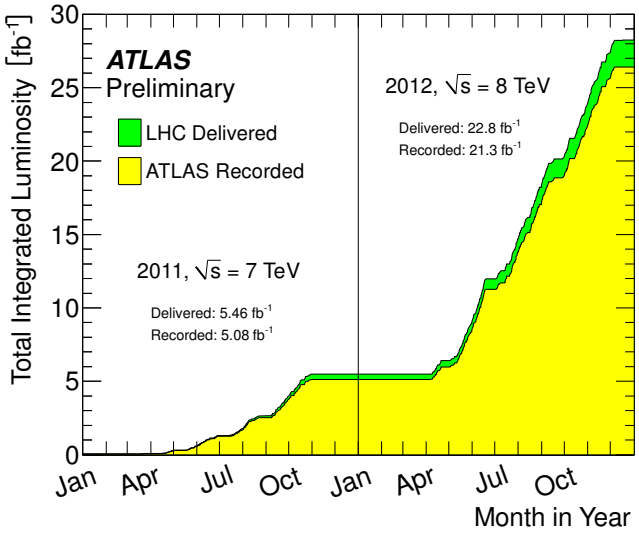

Figure 3.2: ATLAS total integrated luminosity over time for Run 1 (taken from [6]).

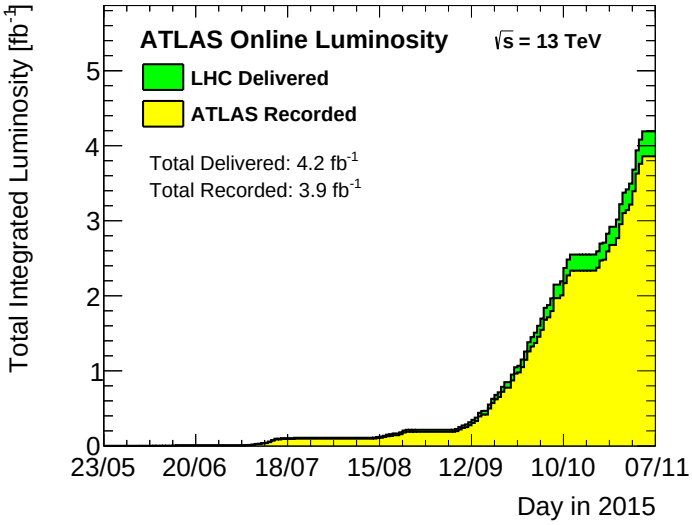

Figure 3.3: ATLAS total integrated luminosity over time for Run 2 (taken from [7]).

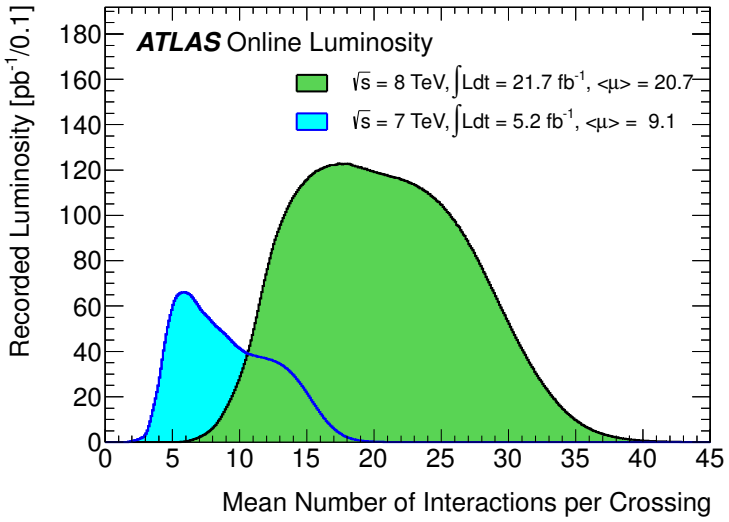

Figure 3.4: ATLAS recorded luminosity as a function of the average interactions per crossing (pileup) at 7 and 8 TeV (taken from [6]).

radiation to the detector that can affect how physics objects are reconstructed and result in mismeasurements of their kinematics. Out-of-time is more significant than in-time for 2011 and 2012 and increases further due to the shortened bunch spacing in 2015. To mitigate the effects of pileup a correction is applied to data based on the number of reconstructed primary vertices and the mean number of interactions per crossing ($\langle\mu\rangle$). $\langle\mu\rangle$ is shown for Run 1 in Figure 3.4 and for Run 2 in Figure 3.5.

3.2 The ATLAS Coordinate System

The ATLAS collaboration uses a coordinate system with the origin located at the interaction point and with the z direction along the beam axis. The x-y plane is perpendicular to the beam axis with the positive x direction pointing towards the centre of the LHC ring and positive y pointing up. All transverse quantities such as p_T are defined in this plane.

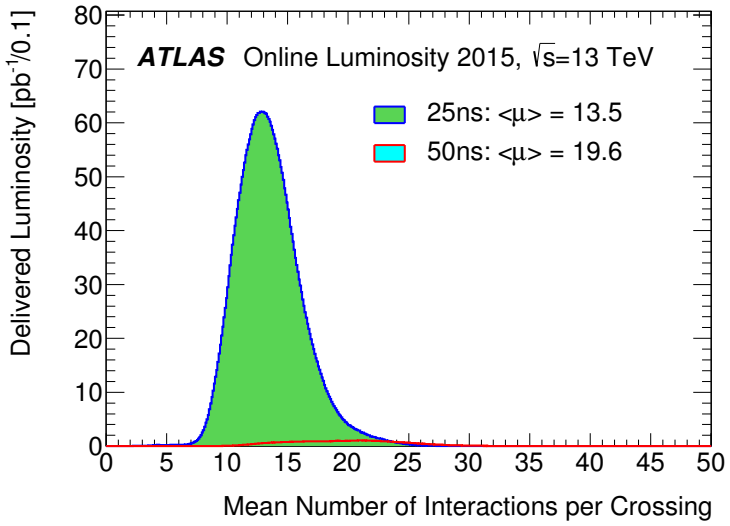

Figure 3.5: ATLAS recorded luminosity as a function of the average interactions per crossing (pileup) at 13 for both 25 and 50 ns bunch spacings (taken from [7]).

From these a polar coordinate system is defined with θ as the angle from the beamline and ϕ as the radial angle about the beamline. These can be used to define a Lorentz invariant angle, referred to as pseudorapidity.

The rapidity is defined as:

$$y = \frac{1}{2} \ln \frac{E + p_z}{E - p_z} \,, \tag{3.3}$$

where E is the energy and p_z the component of momentum along the beam axis. For a particle close to the speed of light and $E >> M$, the pseudorapidity can be well-approximated as

$$\eta = \ln \tan \left(\frac{\theta}{2} \right) \,. \tag{3.4}$$

To calculate the distance between two objects in η - ϕ space a quantity ΔR is defined as:

$$\Delta R = \sqrt{(\Delta\phi)^2 + (\Delta\eta)^2} \,, \tag{3.5}$$

where $\Delta\phi$ is the radial angle between the two objects and $\Delta\eta$ the difference in pseudorapidity [8].

3.3 The ATLAS Detector

The ATLAS detector is a general purpose detector intended to perform a variety of physics measurements and searches at the LHC. The searches include looking for evidence of the Higgs mechanism, supersymmetry, and other beyond-standard-model (BSM) theories. To do this the detector has to be able to distinguish between different decayed particles in order to reconstruct the characteristic signatures of different models. This is done by combining particle track and vertex information with energy deposits in the various calorimeter systems. This allows the separation of muons, electrons, photons and jets of hadrons with good although not perfect accuracy.

The rarity of the processes that the collaboration seeks to observe, combined with the high energy collisions that the LHC can produce and the large amount of background radiation that this entails, places high demands on the detector design:

- Radiation hardness of sensors and electronics alongside high granularity.
- Wide pseudorapidity and azimuthal coverage to measure as many of the final state particles as possible.
- Good track resolution for b-jet identification.
- Good calorimetry for identifying electrons and accurately measuring jet energies

- A muon system that can perform charge identification and momentum measurements.

- A trigger system that can adequately reject backgrounds with sufficient signal efficiency to reduce the data rate to a manageable amount.

The detector measures 25 m high and 44 m along the beam axis. The innermost part is the Inner Detector, which is surrounded by a solenoid that provides a 2 T magnetic field. This is used to provide information about particle tracks and vertices by observing their path in a magnetic field. It has a coverage of $|\eta| < 2.5$. Surrounding that is the LAr EM barrel calorimeter, which is used to measure the energy of photons and electrons, and has coverage of $|\eta| < 3.2$. The scintillator-tile hadronic calorimeter is the next layer consisting of a large central barrel and two smaller extended barrels giving an $|\eta| < 1.7$ coverage. It is used to measure the energy of hadrons.

The end-cap region is defined as $|\eta| > 1.5$. This region has additional coverage out to $|\eta| = 4.9$ using LAr forward calorimeters for both electromagnetic and hadronic energy measurements.

The muon spectrometer surrounds the calorimeter and consists of a barrel and two end caps in a magnetic system consisting of a central toroid and two end caps. This gives a coverage of $|\eta| < 2.7$ and is used to measure muon momentum[8].

3.4 Inner Detector

The Inner Detector (ID) is responsible for tracking charged particles from the LHC beam pipe to the electromagnetic calorimeter. It allows interaction vertices to be located and charged particle momenta to be measured. In Run 1 it had three components: the Transition Radiation Tracker (TRT), the SemiConductor

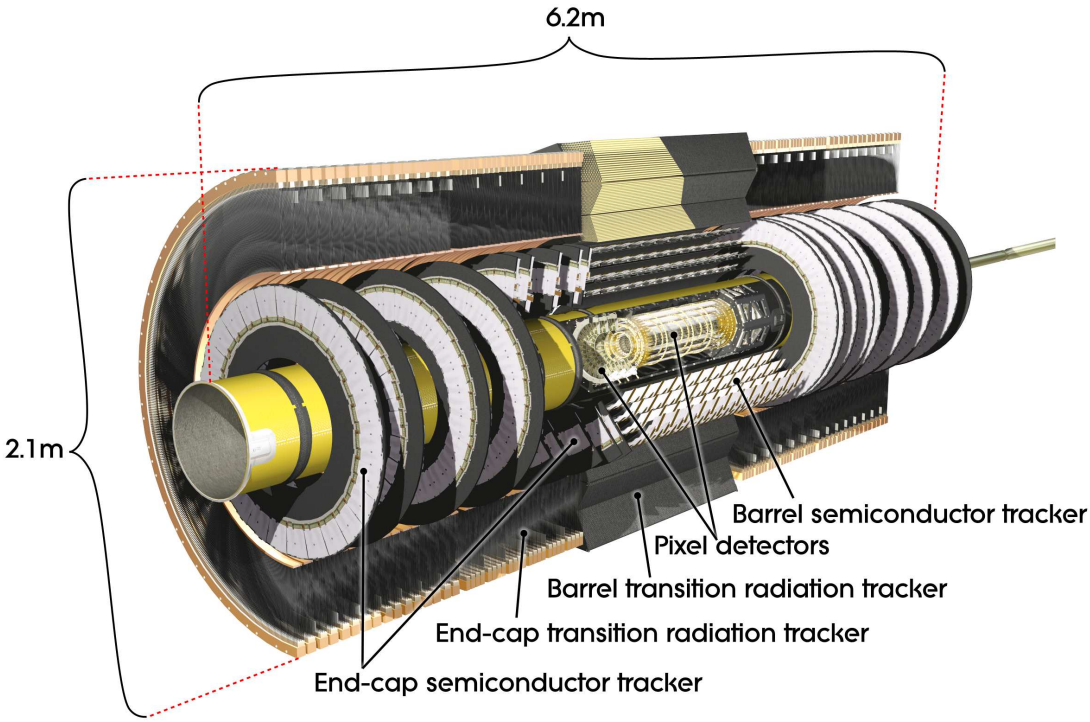

Figure 3.6: Diagram of the ATLAS inner detector (taken from [8]).

Tracker (SCT) and the Pixel Detector; all of which are inside a 2T magnetic field. In Run 2 an extra component was added called the Insertible B Layer (IBL) to improve the tracking and b-tagging performance. A diagram of the layout of the ID for Run 1 is shown in Figure 3.6. The ID gives a coverage of $|\eta| < 2.5$.

3.4.1 Pixel Detector

The pixel detector is made up of pixel sensors which are semiconductors. When a sufficiently energetic particle passes through them an electron-hole pair is produced that causes current to flow in the semiconductor which can be read out as a physics signal. There are 1744 pixel sensors in the detector with pixel size $50\,\mu$m in the $R-\phi$ direction and $400\,\mu$m in z. The detector consists of 3 barrels at a nominal distance from the interaction point of 50.5, 88.5 and 122.5 mm, and 3

disk endcaps on each side at z positions of 495, 580 and 650 mm. It provides high granularity, high precision measurements close to the interaction point with an $|\eta|$ coverage of 2.5 for the first barrel layer. The resolution is 10 μm in the $R-\phi$ direction and 115 μm in the z direction. Particles traversing the pixel detector provide three space time points that can be used for impact parameter and vertexing measurements that are particularly useful for heavy flavour tagging. The innermost pixel layer is sometimes referred to as the b-layer for this reason[8].

3.4.2 Semiconductor Tracker

The Semiconductor Tracker (SCT) is a strip detector that provides four precision measurements that contribute to momentum, impact parameter and vertex position reconstruction. There are 4 double-sided layers in the barrel region and 9 end-cap disks. Each detector element consists of two 6 cm sensors that are daisy-chained. There are 768 active strips each at a pitch of 80 μm. The spatial resolution is 17 μm in $R-\phi$ and 580 μm in z. Tracks can be distinguished if they have a separation of 200 μm. This system provides a coverage of $|\eta|$ up to 2.5 and gives extra vertex information that is important for heavy flavour tagging. The detector elements are reverse-biased semiconductors. They produce electron hole pairs when traversed by a charged particle that can be read out as an electronic signal[8].

3.4.3 Transition Radiation Tracker

The Transition Radiation Tracker (TRT) consists of layers of straw detectors filled with gas with a wire running down the centre sometimes called a drift tube. When a particle passes through these straws the gas will be ionised and

the resulting free electrons are attracted to the charged wire. These electrons will further ionise the gas causing an avalanche effect and thus charge builds up on the wire which can be read out as a physics signal. The TRT has a barrel and an end-cap. Each straw is 4 mm in diameter and has a length of 144 cm in the barrel and 37 cm in the end-cap. The straws are arranged parallel to the beam axis divided in half at $\eta = 0$ in the barrel and are arranged radially in wheels in the end-caps. The TRT gives coverage of $|\eta| < 2.0$. This design gives a fast response and good radiation hardness. The drift time measurement in the straws gives a spatial resolution of 130 μm for each straw. The detection of transition radiation in this system improves electron identification as the amount of radiation is proportional to the γ factor[8].

3.5 Calorimeter

The calorimeter consists of an electromagnetic calorimeter and a hadronic calorimeter. The former is located around the inner detector and the latter around that. Both have a barrel section and an endcap. A diagram of the layout is shown in Figure 3.7. This layout gives coverage of up to $|\eta| = 4.9$.

3.5.1 LAr Electromagnetic Calorimeter

The EM calorimeter consists of a barrel with $|\eta|$ coverage up to 1.475 and two end caps with a coverage of $1.375 < |\eta| < 3.2$. The barrel consists of two half barrels with a small gap at z=0 and is divided into two wheels, one at $1.375 < |\eta| < 2.5$ and the other at $2.5 < |\eta| < 3.2$. They are accordion shaped and made of lead and liquid argon (LAr). All of this is contained in a vacuum cryostat. The liquid argon is used as an active medium for particle detection, and the lead as

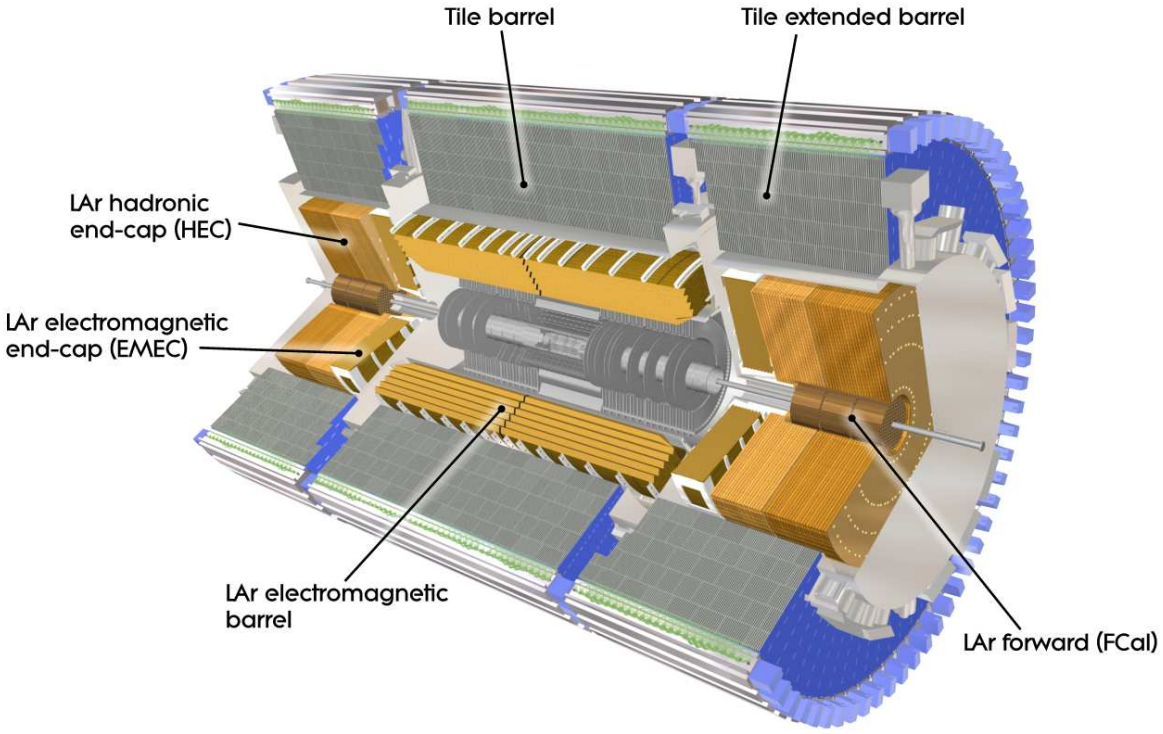

Figure 3.7: Diagram of the ATLAS calorimeter taken from [8]. Note the greyed out section in the centre showing the position of the inner detector in relation to the calorimeters.

a particle absorber. Electromagnetic particles that enter the detector undergo bremsstrahlung in the Argon producing photons that undergo pair production to produce an electron positron pair what will in turn undergo bremsstrahlung producing more photons. This process continues until the photon energy drops below the pair production threshold. The electrons are read out as a physics signal. The accordion shape of the calorimeter shape gives complete ϕ symmetry without azimuthal cracks. The EM calorimeter is three layers deep in the region $|\eta| < 2.5$, which is the region designed for precision physics. For the rest of the $|\eta|$ coverage there are only two layers. In the region $|\eta| < 1.8$ a presampler made of a LAr layer is used to correct for energy lost by electrons and photons in the ID. This calorimeter is primarily used for electron and photon energy measurements [8].

3.5.2 Hadronic Calorimeters

The hadronic calorimetry system consists of three sections: a tile calorimeter, a LAr hadronic endcap calorimeter and a LAr forward calorimeter. It is mostly used for jet reconstruction and missing transverse energy (E_T^{miss}) measurements. It must also stop other particles from passing into the muon system.

The tile calorimeter consists of a central barrel and two extended barrels all of which have three layers in depth. The central barrel has an $|\eta| < 1.0$ coverage while the extended barrels have range $0.8 < |\eta| < 1.7$ and consist of 64 modules divided azimuthally. The modules are constructed from steel and scintillating tiles with the steel as an absorber and the scintillating tiles as the active material. Incoming particles undergo inelastic hadronic interactions with the active material causing particle decays. This is a hadronic shower and it produces photons which can be read out by wavelength shifting fibres in the tiles

into photomultiplier tubes (PMTs).

The LAr hadronic endcap (HEC) has a coverage of $1.5 < |\eta| < 3.2$ and thus overlaps with both the forward calorimeter and tile calorimeter. It consists of wheels made from wedge shaped modules made of copper plates with LAr as a sampling medium. Each endcap has two wheels.

The LAr forward calorimeter (FCal) consists of three layers. The first is copper and is used for EM measurements; the second and third are tungsten and used for hadronic measurements, all with LAr as the active medium. It has a coverage of $3.1 < |\eta| < 4.9$ [8].

3.6 Muon System

The layout of the Muon system of the ATLAS detector is shown in Figure 3.8. It consists of four distinct technologies. Monitored drift tubes (MDT) and cathode strip chambers (CSC) are used for precision tracking, and resistive plate chambers (RPC) and thin gap chambers (TGC) are used for triggering and providing a second coordinate measurement. The system is designed to give momentum measurements in the range $|\eta| < 2.7$ and trigger coverage up to $|\eta| < 2.4$. The system is immersed in a magnetic field provided by a large barrel toroid and two end cap magnets. The bending power (characterised by the field integral perpendicular to a muon of infinite momentum) is described by the three regions of magnetic coverage. The barrel toroid region $0 < |\eta| < 1.4$ provides 1.5 to 5.5 Tm; the end-cap region $1.6 < |\eta| < 2.7$ gives 1 to 7.5 Tm; and a lower bending power in the region of overlap $1.4 < |\eta| < 1.6$ [8].

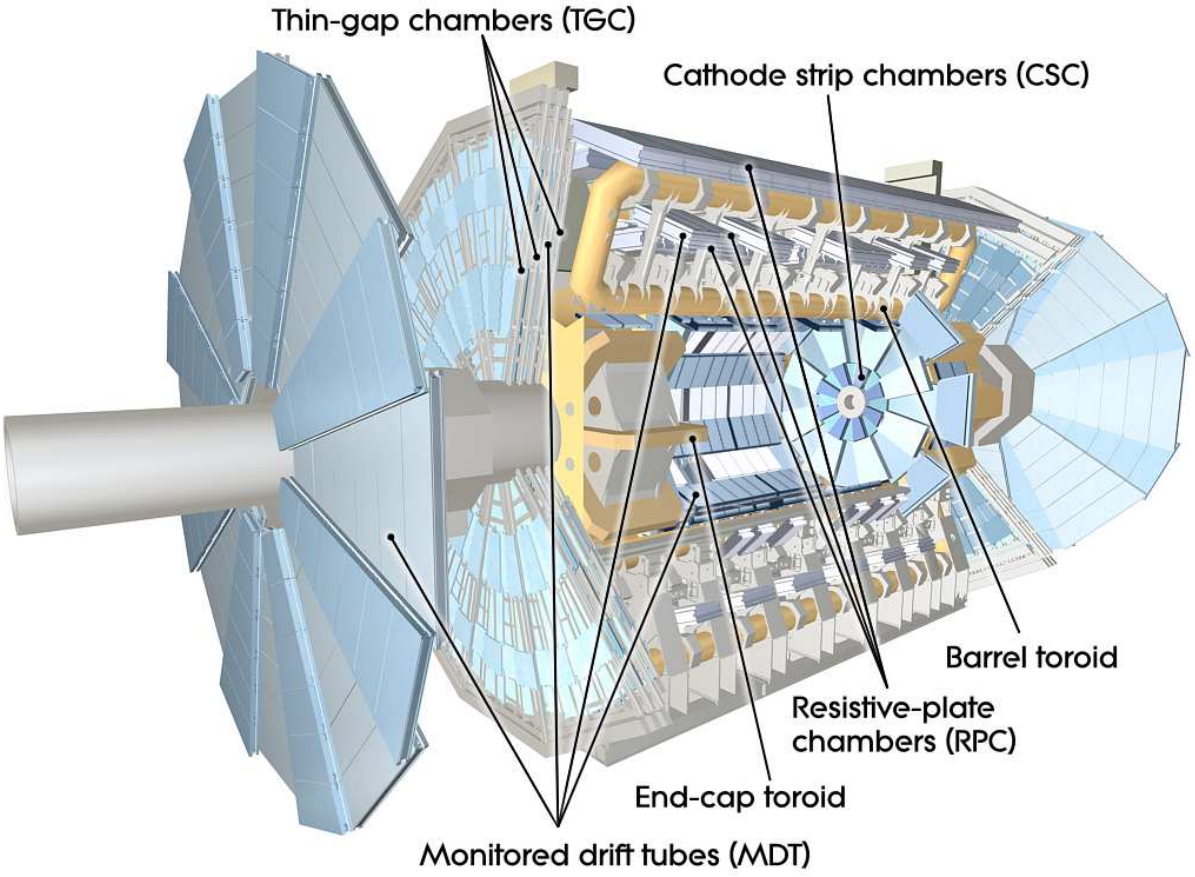

Figure 3.8: Diagram of the ATLAS Muon chamber taken from [8].

3.6.1 Precision tracking

Monitored drift tube chambers give high measurement accuracy and are simple to construct. They work using the same physics as TRT in the inner detector. They give a coverage of $|\eta| < 2.7$ except for the innermost end-cap layer where they only go out to $|\eta| < 2.0$. The chambers are constructed of layers of drift tubes and provide a resolution of $\sim$35 μm per chamber. Cathode strip chambers are used in the forward region ($2.0 < |\eta| < 2.7$) of the innermost tracking layer and have a resolution of 40 μm in the bending plane and 5 mm in the transverse plane. They are constructed from arrays of positively charged wires crossed by negatively charged wires within a gas. Particles produce a signal using the same physics as a drift tube [8].

3.6.2 Triggering system

Resistive plate chambers are used for triggering and are capable of delivering track information within a few tens of nanoseconds. They give coverage in the barrel region with $|\eta| < 1.05$. Thin gap chambers are also used for triggering and have similar time resolution to the resistive plate chambers and give coverage in the end-cap region of $1.05 < |\eta| < 2.4$[8]. The ATLAS trigger system is described in detail in section 3.7. Both of these technologies use the same physics as drift tubes to produce a signal.

3.7 ATLAS Trigger System

Collisions at the LHC produce a very high number of interactions. In order to record these interactions a trigger system was designed to reduce the high data rate that does not overwhelm the available storage space and processing power.

This system consists of three steps: the Level 1 (L1) trigger, the Level 2 (L2) trigger and the Event Filter.

The L1 trigger is the first of the three steps. This step aims to reduce the data rate from 1 GHz to a maximum of 75 KHz. It is based on fast custom electronics that apply very basic selection criteria using information from the calorimeters and muon subdetectors. The latency of this system is $\sim 2.5\mu s$. The L1 trigger also identifies regions of interest (RoIs) that are used by later parts of the trigger system. When an event is accepted by the L1 trigger system the data is transferred into readout buffers (ROBs) which are grouped into readout systems (ROS).

The L2 trigger uses the RoIs from L1 and applies fast custom algorithms to process the data from all the subdetector systems. The data rate is reduced to a maximum of 3 kHz. Next the event builder uses ROBs for events that pass the L2 system to provide full event information to the Event Filter (EF). The EF consists of offline algorithms that are invoked using a custom interface for running in the trigger system. The data rate is reduced to 200 Hz that is recorded for use in physics analyses. [36]

3.8 Simulation of collisions

In order to compare the data recorded in the ATLAS detector with theoretical predictions from the Standard Model the ATLAS collaboration uses a variety of software to produce Monte Carlo simulations of all expected physics processes. The software can be summarised as having three steps: event generation and decay simulation, simulation of the detector and the corresponding particle interactions with the detector medium, and digitization of the resulting simulated

energy deposits into electronic signals that can be compared with ATLAS data. This allows for the same ATLAS reconstruction software to be used on data and simulation[37].

An overview of Monte Carlo generators was presented in section 1.5. The detector simulation was performed using the GEANT4 software package [38].

3.9 Run 2 Detector Upgrade

Some upgrades were performed on the ATLAS detector during the shutdown between Run 1 and Run 2. A new beam pipe was installed and a fourth layer was added to the pixel layer, called the Insertible B-Layer (IBL), between the beam pipe and the current innermost pixel layer (B-layer). There are several motivations for adding another layer to the pixel detector. In the original design of the ATLAS detector the B-layer was intended to be replaced regularly because of the expected radiation damage. The final design makes the extraction of the B-layer complicated and it was decided that the best solution was to replace the beampipe with a smaller pipe that allows for the insertion of a new inner layer. The addition of the IBL compensates for the effects of the deterioration of the B-layer on b-tagging and tracking performance. The decreased distance to the interaction point also improves the b-tagging performance.

The IBL gives full coverage in ϕ and coverage of $|\eta| < 3.0$ and is similar in technology to the other pixel detectors [9]. A diagram of the layout is shown in Figure 3.9.

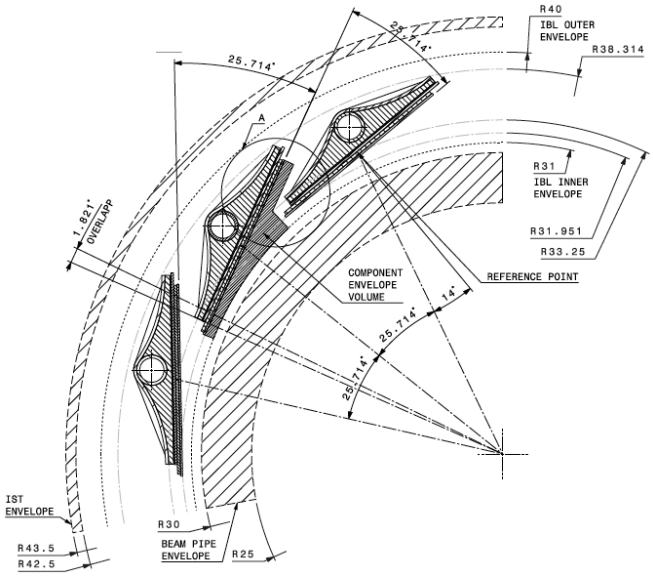

Figure 3.9: Diagram of the Insertable B-Layer (IBL) layout showing its position in relation to the beam pipe. (taken from [9])

Chapter 4

Object Reconstruction

This chapter describes how signals, known as 'physics objects' are identified and reconstructed from tracking information and energy deposits recorded in the ATLAS detector. The objects of interest are electrons, muons, jets of hadrons and missing energy (MET) corresponding to particles escaping the detector. Photons are also reconstructed but they are not of interest to either of the analyses in this thesis. The reconstruction algorithms make use of the vertex and tracking information from the inner detector, calorimeter deposits in both the hadronic calorimeter and the EM calorimeter, and tracks in the muon chamber to construct an object that then must pass some criteria to be considered an electron, jet or muon. These objects are then used to check the momentum balance of an event and caluclate the missing transverse energy.

The analyses presented in Part III rely on the object reconstruction described in this section and the uncertainties on these methods will, to varying degrees, have an effect on the sensitivity of the results presented.

4.1 Data Acquisition

Two analyses are presented in Part III of this thesis using different datasets. The first uses the full dataset from the ATLAS Run 1 which consists of 4.7 fb^{-1} at 7 TeV and 20.4 fb^{-1} at 8 TeV. The second uses the early data taken in Run 2, which consists of 3.2 fb^{-1} at 13 TeV. This data is broken down into periods that are themselves split into runs, which again are made up of 'lumiblocks' that correspond to approximately 2 minutes of a physics run. A Good Run List can be constructed in terms of these lumiblocks in order to mark as bad any data which is affected by technical malfunctions that can cause problems in recording and correctly reconstructing physics objects.

4.2 Tracking and Vertex Finding

In Run 1 data, tracks are reconstructed in the ATLAS detector starting from the innermost detector system and moving outwards. Track reconstruction begins by finding track seeds. A seed is defined as 3 space points in the pixel and SCT detectors. For the pixel detector a cluster of hits is considered a space point whereas for the SCT a hit on both sides of the module is considered a space point.

This seed is then used to build a track in the rest of the detector using a Kalman filter which will project the track onto the next layer and use information from any hits near this path to refine the path through the previous layers. This process can assign a hit to more than one track and can also result in tracks containing outlying hits. To solve these problems each track is awarded a score based on the number of hits that make up a track weighted appropriately for the precision of the detector element, missing but expected measurement points

given the trajectory, the χ^2 of the track, and the $\log p_t$ of the track. Tracks with a score below some threshold are discarded. The Kalman filter process is then repeated for the remaining tracks but this time the track is extended into the TRT and this extension is kept only if it improves the quality of fit.

These tracks can now be used to reconstruct the primary vertex. The algorithm used for this in Run 1 is called iterative vertex finding and fitting. It starts by selecting tracks that pass some quality criteria, and selecting a vertex seed by finding the maximum in a histogram of the z position of the tracks. Next an iterative fit is performed on the χ^2 of the tracks. During the fit a weight is applied to each track and progressively changed. This weight, defined as

$$\omega(\chi^2) = \frac{1}{1 + \exp(\frac{\chi^2 - \chi^2_{\text{cutoff}}}{2\text{T}})}\,, \tag{4.1}$$

depends on how far the χ^2 of the track in the previous iteration is from some cutoff and a temperature parameter, T, that starts high and is progressively reduced until it reaches 0. When that happens the weight becomes a step function and defines which tracks are used in determining the vertex position. Tracks that are incompatible with the vertex by some set value of χ^2 are put into a pool to be used in finding the next primary vertex. The algorithm is rerun to find more primary vertices until there are no more tracks left or no vertex can be found [39].

In Run 2 track reconstruction and vertex finding is the same but with improvements made to pixel cluster sharing between different tracks. This is vital for Run 2 as the increased centre of mass energy will increase the track density in the detector, which means that more tracks will share pixel clusters [40].

4.3 Electrons

4.3.1 Electron Trigger

The electron trigger works in two stages: the level 1 (L1) trigger, which is hardware based, and the high level triger (HLT), which is software based. The L1 trigger makes use of the calorimeter to perform some basic reconstruction. It uses calorimeter areas of size $\eta \times \phi \approx 0.1 \times 0.1$ called trigger towers to identify RoIs. For each tower the E_T of the cells of the hadronic or EM calorimeter are summed except the fourth layer of the hadronic endcap and barrel-endcap gap scintillators. A cluster is formed by finding a local maximum using a sliding window algorithm on an area of 4×4 towers. A cluster passes the trigger if a 2×2 region within the window contains a pair of neighbouring towers that passes a particular threshold.

The HLT consists of two parts: L2 and the event filter (EF). They make use of both the tracker and the calorimeter. Using RoIs that pass the L1 trigger cells are combined to form a cell cluster with $\eta \times \phi \approx 0.4 \times 0.4$. The cell with the largest energy deposit in this area is found and used as a pre-seed (due to time constraints only the second layer of the EM calorimeter is used to find the pre-seed) for building electron clusters. Two cluster sizes are used: 3×7 when the cluster is in the barrel and 5×5 when it is in the end-cap. A fast tracking algorithm called IDScan is used at L2 to reconstruct tracks. It looks at tracks around the RoI from L1. It first finds the z position of the primary interaction point and then performs combinatorial tracking using points with the same $\eta - \phi$ coordinates that match the interaction point [41]. The EF then uses offline-like algorithms to reconstruct calorimeter quantities and a version of the offline track reconstruction software that is constrained to data available in the RoIs [42].

4.3.2 Electron Candidate Reconstruction

In the ATLAS detector electrons are reconstructed from energy deposits in the calorimeter that are matched to tracks. The first step in this reconstruction is to reconstruct energy clusters in the calorimeter. This is done using a seeding algorithm. This works by dividing the calorimeter into towers forming a grid in $\eta - \phi$ space corresponding to the granularity of the middle layer of the EM accordion. The energy in all layers is summed to get the tower energy. Next a window of size 3×5 towers in $\eta - \phi$ space is moved across the grid of towers. If the window energy is above 2.5 GeV and is a local maximum then this is called a precluster and its centre is calculated as the energy-weighted centre of mass of the towers. Once all preclusters have been found, duplicates are removed by discarding any lower-energy preclusters within a certain distance of another. Finally to form an EM cluster, all cells around the seed in a rectangle of 5×5 in the middle layer are used to calculate the energy weighted centre of mass. This gives the seed position which is also used as the seed position for the back layer. This calculation is then repeated for the strips layer the result of which is used as the seed position used for the presampler layer. The sum of all the energy deposits in a rectangle of 5×5 around these seed positions forms a cluster.

Next it is necessary to reconstruct electron track candidates. This is done by first taking calorimeter clusters that pass some loose shower shape requirements. For these clusters a region of interest (ROI) of $\Delta R = 0.3$ around the seed cluster barycenter is defined. Track pattern recognition is then run. Two hypotheses are considered, the pion and electron, that model two different expectations of energy loss at a materials surface. First the pion hypothesis for energy loss is considered. If a track seed with $P_T >$ 1 GeV is not found with at least 7 hits and within one of the RoIs, the pattern recognition using the electron energy loss

hypothesis is run. For all tracks a χ^2 is calculated for the track hypothesis. If a track fails the jet track fitting it is refitted with the electron track fitter. Any tracks that pass the pattern recognition and fitting stages are then matched to an EM cluster if they pass either of two sets of criteria. For the first, tracks with > 4 silicon hits are extrapolated from their closest approach to the primary vertex to the middle layer of the EM accordion. They then must be within $|\eta|$ of 0.05 of an EM cluster and within ϕ of 0.2 on the inner side of the track curve or within 0.05 on the outer side. Tracks with < 4 hits must pass the same ϕ criteria but have no $|\eta|$ criteria. The second set of criteria is meant to recover low momentum tracks that have lost a lot of energy before reaching the calorimeter. It involves extrapolating the track after rescaling its momentum to the energy of the calorimeter cluster. The resulting track must then be within ϕ of 0.1 on the inner side of the track curve and within 0.05 on the outer side.

All tracks passing these criteria and matched to an EM cluster are considered an electon candidate. These are then refitted using a Gaussian Sum Filter [43]. Any that fail the GSF fit keep the previously calculated track values [42] [10].

4.3.3 Electron Identification

Finally, to select electron candidates the track-cluster association is redone. This is done similarly to previously described but using the already selected tracks and applying tighter cuts. A cut of $\Delta\phi < 0.1$ is applied and for TRT-only tracks $\Delta\eta < 0.35\,(0.2)$ is disregarded in the barrel (endcap) and $\Delta\phi < 0.03\,(0.02)$ on the (opposite) side the track is bending towards. If a seed cluster has at least one track matched it is considered an electron candidate. If a cluster has more than one matched track, those with hits in both the pixel detector and the SCT are prioritised and the one with the smallest ΔR from the seed cluster is chosen.

Seed clusters with no matching tracks are considered to be unconverted photons; converted photons are identified by looking for pairs of tracks nearby that come from a displaced vertex and by looking for missing hits near the beginning of the path of the track.

The electron candidates selected will not be 100% pure, but will contain objects that are not electrons. Some will be jets that passed electron pattern recognition and fitting; others electrons from heavy flavour decays and photon conversions etc. To separate these from prompt electrons both a cut-based and a likelihood approach have been developed [10]. For the analyses in Part III the likelihood approach with 3 different working points is used, referred to as loose, medium and very tight. A likelihood function uses signal and background PDFs of multiple variables to produce a signal probability that can be used as a discriminant. The loose category contains variables used for discriminating against light flavour jets, the medium and very tight categories contain extra variables to reject heavy flavour jets and conversions. For a full list of the variables used for each working point see [10]. The likelihood is parameterised into 9 bins in η and 6 bins in E_T. The combined efficiency for E_T and η is shown in Figure 4.1 for both data and MC. The LooseLH shows the best agreement between data and MC, and also as expected the best efficiency [10].

4.3.4 Electron Efficiency Measurement

The efficiency of electron identification and reconstruction is measured using a method called 'tag and probe'. This technique uses $Z \to ee$ and $J/\Psi \to ee$ decays. Strict selection criteria is applied to one of the electrons (called the "tag") and the efficiency is measured on the second ("probe") electron. An electron that has been used as a tag can be reused as a probe. The probe sample will be

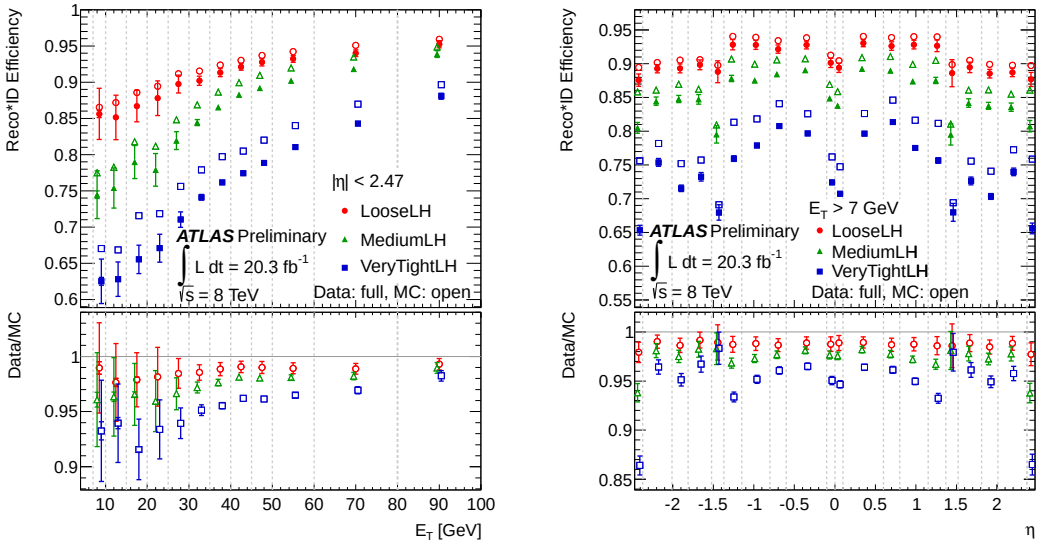

Figure 4.1: Electron reconstruction and identification efficiency as a function of E_T (left) and η (right) for the LooseLH, MediumLH and VeryTightLH working points for the 8 TeV dataset (taken from [10]).

contaminated by background which is often modelled using a template method. This usually consists of keeping the same selection as in the signal sample but inverting some selection requirements, usually isolation cuts, to get a close to pure sample of the background and then estimating the normalisation by fitting to data in some control region.

The efficiency is measured as the fraction of electrons in the probe category that pass the criteria we seek to test. The efficiency is measured separately for the trigger, reconstruction and identification. The reconstruction efficiency is defined relative to the clusters reconstructed in the EM calorimeter; the identification efficiency is then derived relative to the reconstructed electrons, and the trigger efficiency is defined for identification electrons therefore the efficiency depends on the identification selection chosen. The efficiency of reconstruction for electrons binned in both E_T and η can be seen in Figure 4.2. The data MC agreement is good across the parameter space and for 2012 the efficiency never drops below 95% [10].

4.3.5 Data to MC scale factors

The MC simulations used to model various physics processes may need to be corrected to reproduce the efficiencies measured in data. To do this the ratio of the efficiency measured in data to that measured in MC is used to correct the MC simulation. This ratio is often close to unity, but various problems in modelling can cause this to not be the case. The efficiency plots in Figure 4.1 show that for LooseLH the scale factors would be very close to 1 but for other working points correcting for differences in data and MC would become important for an analysis [10].

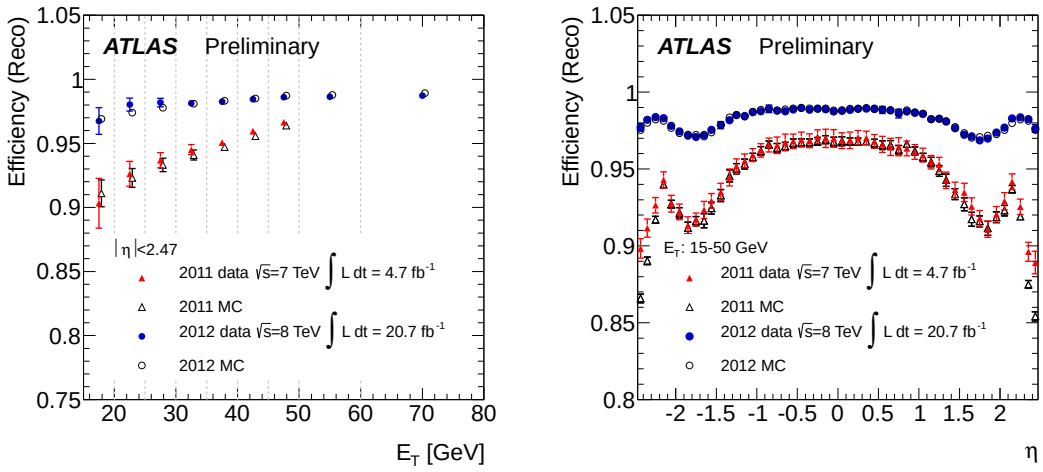

Figure 4.2: Electron reconstruction efficiency as a function of E_T (left) and η (right) for 7 and 8 TeV datasets (taken from [10])

4.4 Muons

4.4.1 Muon Trigger

The muon trigger, like the electron trigger, works in two stages: L1 and HLT. The L1 trigger can be fired by a coincidence of position and time measurements in either the RPC or TGC. The number of coincident points required differs depending on the muon p_T threshold. The p_T is estimated using the deviation of the hit pattern from that expected for a muon with infinite momentum. Six p_T thresholds are defined. For the trigger to fire in the RPC a number of hits must be observed. For the three highest p_T thresholds (20, 15 and 10 GeV), hits in 3 layers are required. For the other thresholds, hits in 2 of the 3 layers are required. For the TGC trigger a coincidence of 3 hits is required, except for limited areas

in the lowest threshold. The detector regions (RoIs) and p_T measurements are sent to HLT. Typical dimensions of these RoIs in $\eta - \phi$ is 0.1×0.1 (0.3×0.3) in the RPCs (TGCs). The geometric coverage is 99% in the endcap but is only 80% in the barrel due to gaps for inner detector services among other things.

The HLT is divided into two parts: first, the Level 2 reconstruction, and then the event filter. The Level 2 reconstruction takes the RoIs from L1 and adds the information from the MDT which is used to reestimate the track parameters. Next this new track is matched to a track in the inner detector chosen as the closest track in the $\eta - \phi$ plane. A weighted average is then used to reestimate the p_T. The product of this procedure is referred to as a Level 2 combined muon.

The next stage is the event filter which has two methods for finding muons: the RoI based method, and the full scan method. The RoI method uses the RoIs from the Level 1 and Level 2 steps, builds muons from these using the muon detectors, and combines them with inner detector tracks. The resulting muons are referred to as event filter combined muons. If no combined muons are formed then inner detector tracks are extrapolated to the muon detector and if matched to track segments then a muon is formed. The isolation of the muon is also calculated using tracks with $p_T^{track} > 1$ GeV within some ΔR_{cut} around the muon excluding the muon itself:

$$Iso = \sum_{\Delta R < \Delta R_{cut}} p_T^{trk} \tag{4.2}$$

and can be used as a selection criteria for a particular trigger, for instance requiring that the isolation value be small for a large value of ΔR_{cut} gives a high muon purity.

The full scan method is used to find additional muons not reconstructed by the RoI method. These muons are called full scan muons and are reconstructed

from combined pairs of inner detector tracks and muon detector tracks. These tracks are reconstructed using the whole of the muon detector and the inner detector.

There are a variety of muon triggers that can be applied depending on analysis requirements. They are all described by some combination of the variables described above: an L1 p_T threshold combined with a p_T on the more refined measurement from the event filter, possibly with an extra isolation measurement criteria [44].

4.4.2 Muon Candidate Reconstruction

Muon reconstruction uses the Muon spectrometer (MS), the inner detector (ID), and also some information from the calorimeter. Reconstruction of tracks in the MS is done in two steps. Local track segments are found in each individual layer of the MS chambers and then these segments are combined to produce a full track. Muons are reconstructed as four different "types" depending on which detector components they have interacted with.

- Stand-Alone (SA) muons are those which are reconstructed only from tracks in the MS. The trajectory is derived from projecting back the tracks, including an estimation of the energy loss in the calorimeter, to the point of closest approach to the beamline. These muons are mostly used in the region $1.5 < |\eta| < 2.7$ where the inner detector has no coverage.

- Combined (CB) muons result from the combination of tracks independently reconstructed and classified as muons in both the MS and the ID. Most muons fall into this category.

- Segment-tagged (ST) muons occur when a track in the inner detector is

extrapolated into the MS and then associated with one or more local track segments in the detector subsystems but not a fully reconstructed MS track. These muons are usually low p_T muons or those crossing a region of the MS without full coverage thus failing the CB muon reconstruction.

- Calorimeter-tagged (CaloTag) muons are reconstructed from tracks in the ID associated with an energy deposit in the calorimeter consistent with a minimum ionizing particle. These are usually found in the region $\eta < 0.1$ as they are designed to recover acceptance in regions that do not have MS coverage.

Two algorithms exist for reconstructing muons, STACO and MuID, both of which provide similar performance. The following ID track quality requirements are applied for both:

- At least one pixel hit
- At least 5 SCT hits
- At most 2 pixel or SCT sensors traversed without hits
- For $0.1 < |\eta| < 1.9$, at least 9 TRT hits

In the region $|\eta| > 2.5$ these requirements are not applied and track segments in the ID can be matched to SA muons to become a CB muon [11].

4.4.3 Muon scale factor and energy corrections

Reconstruction and identification efficiency scales are derived similarly to the electrons, using tag and probe on $Z \to \mu\mu$ and $J/\psi \to \mu\mu$ decays. This results in an efficiency measurement of 99% over most of the detector with agreement

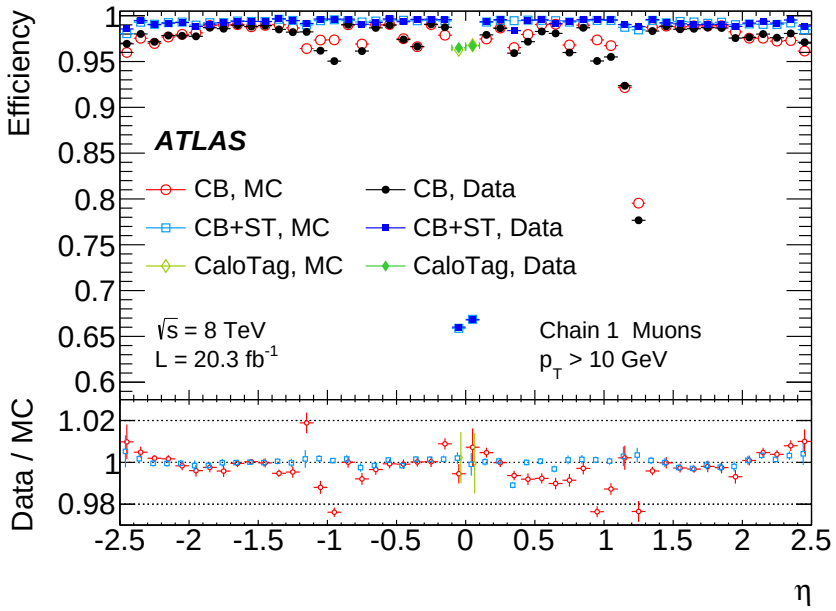

Figure 4.3: Reconstruction efficiency for different Muon types as a function of η for the 8 TeV dataset (taken from [11])

between data and MC within $\sim 1\%$. The data to MC comparison for the muon reconstruction efficiency in η is shown in Figure 4.3. The inefficiencies observed for CB and CB+ST muons are due to the barrel to endcap transition and the joining of the two MS detectors. These are compensated for by using different muon types with better efficiencies in those areas. The data to MC efficiency scale factor is binned in $\eta - \phi$ with no p_t dependence observed.

Also applied are energy scale and resolution smearing. These are required because of imperfections in MC. These corrections are derived so that the scale and resolution of the Z boson mass peak, among others, show good data-MC agreement. The effect of the correction on the mass scale can be seen in Figure 4.4 for the three mass peaks used in the tag and probe method. Similarly for the mass resolution in Figure 4.5. After the correction is applied the mass scale agrees to within 0.2% in all regions and the resolution agrees to within the uncertainty on the corrections [11].

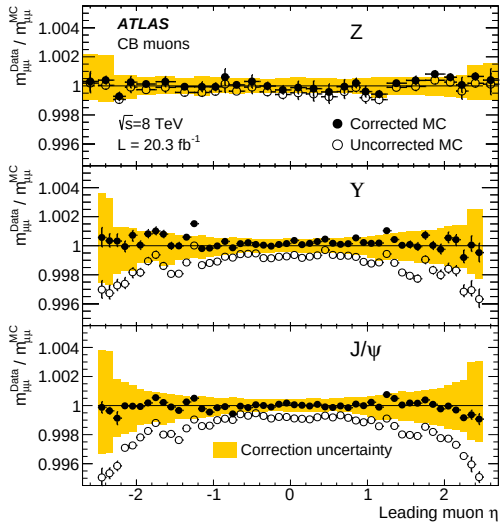

Figure 4.4: Effect of the Muon mass scale correction when applied to Z decays, Y decays and J/ψ as a function of η (taken from [11]).

4.5 Jets

In collisions at hadron colliders partons are produced which hadronise before they reach the detector. These showers of particles are reconstructed as jets. In ATLAS there are two types of jet: calorimeter jets, and track jets. The former are reconstructed from energy deposits in the calorimeter. The latter use inner detector tracks to define the jets. This section will describe the reconstruction and calibration of both calorimeter and track jets, both of which play a large role in the analyses described in Part III.

4.5.1 Calorimeter Jet Reconstruction

Calorimeter jets are reconstructed using a jet algorithm that accepts as inputs either calorimeter clusters or calorimeter towers. Calorimeter clusters are built from topologically connected cells according to the signal significance in each cell

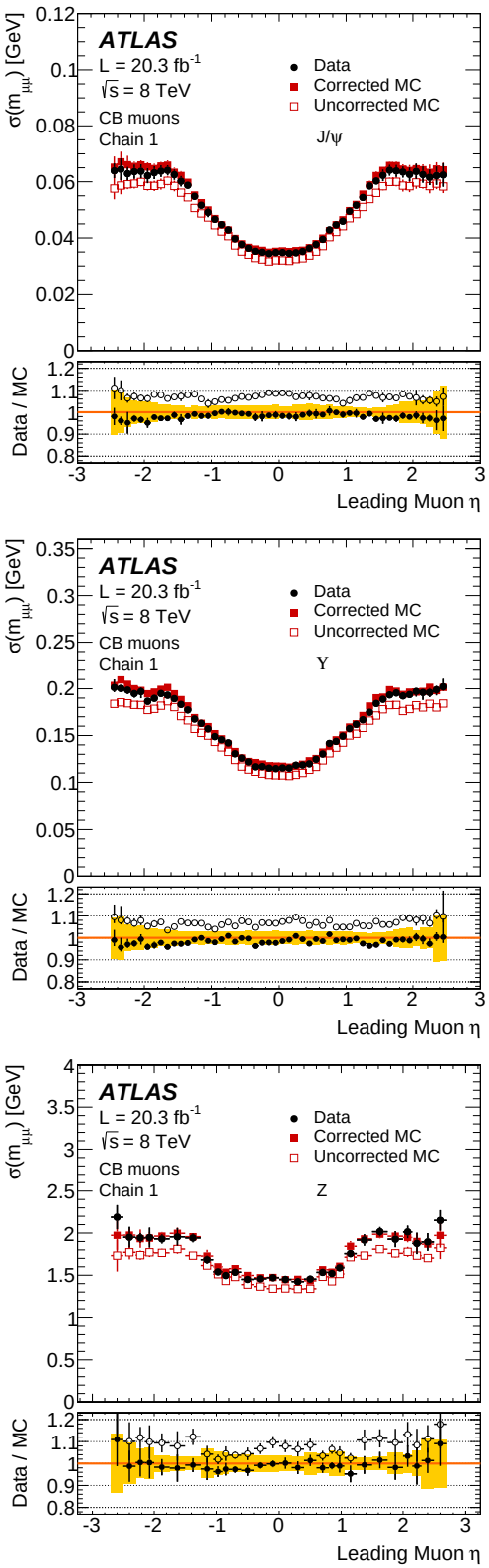

Figure 4.5: Effect of the Muon mass resolution correction when applied to Z decays, Υ decays and J/ψ as a function of η (taken from [11]).

caused by particle showers interacting with the material. The significance of a cell, ς_{cell}^{EM}, is calculated as

$$\varsigma_{cell}^{EM} = \frac{E_{cell}^{EM}}{\sigma_{noise,cell}^{EM}}, \tag{4.3}$$

where $\sigma_{noise,cell}^{EM}$ is defined as the average (expected) noise in the cell from pileup and electronic noise sources. All of these quantities are measured at the EM scale, which means that the energy deposits from electrons and photons are correct but the hadron energy is not correctly calibrated.

The reconstruction algorithm is a series of seed and collect steps that uses 3 parameters defined as S, N and P where S=4, N=2 and P=0. Firstly it checks all cells and if the significance is greater than S for any cell it is considered a protocluster. These are ordered in decreasing ς_{cell}^{EM}. Next, any cells neighbouring a protocluster with $\varsigma_{cell}^{EM} > N$ or $\varsigma_{cell}^{EM} > P$ are added to the same protocluster. (Neighbouring is defined as 2 calorimeter cells that are adjacent in one layer, or those from another cell which overlap in $\eta - \phi$.) The neighbours that have $\varsigma_{cell}^{EM} > N$ in turn have their neighbours added to the protocluster. If a neighbour has $\varsigma_{cell}^{EM} > S$ then the two protoclusters are merged; protoclusters are also merged if a cell with $\varsigma_{cell}^{EM} > N$ is associated with both protoclusters. This algorithm is iteratively applied for each cell with $\varsigma_{cell}^{EM} > N$. After these steps any protoclusters with two local maxima ($E_{cell}^{EM} > 500\,\text{MeV}$) are split into two protoclusters [45].

To reconstruct calorimeter towers, grids of size $\Delta\eta \times \Delta\phi = 0.1 \times 0.1$ are used and the energy within them added to form a tower. Unlike the calorimeter clusters, towers are of a fixed size. In the case of noise-suppressed towers, only calorimeter cells that are used in the calorimeter clusters are included.

Next, the cluster towers are used to reconstruct jets. This is done in ATLAS using the anti-k_t algorithm which is a special case of a class of algorithms called

cluster algorithms. These define a distance measure, d_{ij}, and a cutoff value, d_{iB}:

$$d_{ij} = min(k_{Ti}^{2p}, k_{Tj}^{2p}) \frac{(\Delta R)_{ij}^{2}}{R^2} \tag{4.4}$$

$$d_{iB} = k_{Ti}^{2p} \,. \tag{4.5}$$

These equations are used to calculate and make a list of the values of d for all the protoclusters. If the smallest value is d_{ij}, clusters i and j are combined and the list recalculated. If the smallest value is d_{iB} then this object is considered a complete jet and removed from the list. The Anti-k_t algorithm uses $p = -1$. This means that soft objects are merged into close-by hard objects and gives a regular conical jet. Thus the algorithm is collinear and infrared safe. In ATLAS, R=0.4 is the most commonly used jet radius [46].

4.5.2 Large Radius Jets

For analyses in Run 2 there will be an increasing number of jets with high p_T due to the higher centre of mass energy of the collisions. In the case where the jet p_T reaches above 200-250 GeV, calorimeter jets produced from a 2 body decay reconstructed with R=0.4 can start to merge together. The granularity of the calorimeter makes it difficult to go to jet radii smaller than those already used. The solution to this is to reconstruct these merged jets in the calorimeter as one large radius jet of R=1.0. These jets are reconstructed almost identically to the calorimeter jets described in subsection 4.5.1 but with the addition of some techniques, called jet grooming, which are intended to remove soft components from underlying event (UE), QCD and pileup.

The standard grooming technique applied in ATLAS is trimming. This is done by taking the components of a large jet and applying the k_t algorithm to

build small radius subjets from them. Any subjet with $\frac{p_{Ti}}{p_T^{jet}} < f_{cut}$ is removed. The value of f_{cut} used in the analysis in Part III is 5% with subjets of radius R=0.3. This technique is based on the fact that partons from a hard scatter tend to carry much more momentum than those from pileup and ISR etc [47] [48].

4.5.3 Track Jet Reconstruction and matching

b-tagging, which is discussed in detail in section 4.6, describes methods designed to distinguish hadrons produced from the decay of b quarks from those produced from the decay of other quark flavours. These techniques are highly sensitive to pileup in jets which increases with the jet radius. One possible solution is to use small radius track jets that are matched to the large radius jet and then perform the b-tagging on those jets. The granularity of the tracker is much better than the calorimeter thus allowing us to go to radii at which the jets can be distinguished at much higher p_T. We can also better select jets from the hard scatter vertex and reject pileup using track jets.

Track jets are reconstructed from inner detector tracks. The selection criteria for these tracks are:

- $p_T > 0.5\,\text{GeV}$
- At least one hit in the pixel detector
- 6 hits in the silicon strip detector
- $d_0 < 1.5\,\text{mm}$
- $|z_0 \sin\theta < 1.5\,\text{mm}|$ where θ is the track polar angle

where d_0 is the longitudinal impact parameter and z_0 is the transverse impact parameter. These tracks are then used as inputs to jet reconstruction algorithms

similar to those used for calorimeter jets but with smaller radius parameters of down to 0.2 [49].

4.5.4 Ghost Association

In order to match track jets to large radius calorimeter jets it is possible to do simple matching using ΔR between the track jet and the large radius jet. However since jets are not always a perfectly regular shape, a better way of performing this matching is with ghost association. This method is applied during the jet clustering stage. All track jets in an event have their p_T set to a tiny value. This resulting jet with almost no momentum but with its direction preserved is referred to as a ghost. These ghosts are then added to the energy clusters in the calorimeter that are to be used to reconstruct the large radius jets. When the jet clustering algorithm is run the ghosts are clustered into the large jets: since they have no momentum they do not affect the jet reconstruction, but the result is to know which track jets are associated with a large radius jets [50] [51].

4.5.5 Jet Selection

In ATLAS a process called jet cleaning is applied to jets once they have been reconstructed. It is intended to remove jets that do not originate from a hard scatter, or that are associated with hardware problems. Possible sources of jets other than from a hard scatter include beam gas events, where one proton of the beam collides with residual gas in the beam pipe; beam halo events, which are interactions in the collimators in the beam-line far away from the detector; cosmic ray muons overlapping with collision events; and calorimeter noise. Jet quality is defined by the jet selection efficiency and fake-jet rejection and uses

variables including energy fraction in the EM calorimeter and the maximum energy fraction in one calorimeter layer among others to distinguish between "good" and "bad" jets. There are four categories used in ATLAS: Looser, Loose, Medium, and Tight. Looser has the best selection efficiency and Tight has the best fake rejection factor [52].

4.5.6 Jet Calibrations

Calorimeter jets are reconstructed at the so-called EM scale. This accurately represents photons and electrons but not hadrons, which are typically measured at 15-55% lower than their true energy. This is to a variety of reasons:

- Energy losses from dead material in the detector
- Fluctuations in the EM content of the shower and the non-compensating nature of the calorimeter
- Energy losses from out-of-cone effects during jet reconstruction

There are currently two levels of correction applied to small radius jets in ATLAS run 1 analyses. First, the Jet Energy Scale (JES) correction is applied, and then the Global Sequential Calibration (GSC).

Jet Energy Scale (JES)

The JES correction consists of 3 steps. The first is the correction of the jet origin. Topological clusters from which the jets are constructed have their direction in the (η, ϕ) plane defined between the centre of the ATLAS detector and the energy-weighted barycentre of the cluster. The jet origin correction step adjusts this so that the jet originates from the hard scatter vertex. This is done by redefining

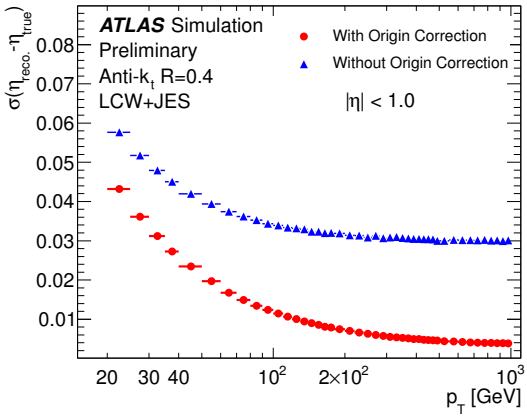

Figure 4.6: Effect of the jet origin correction on the η resolution as a function of p_T (taken from [12]).

the (η, ϕ) of the topo-clusters so that they point to the hard scatter vertex and then recalculating the jet 4-momentum from these adjusted clusters. The effect of this correction on the rapidity resolution can be seen in Figure 4.6, where a clear improvement is visible.

The second step is to correct for the effect of pileup on the jet kinematics. The contribution from pileup is estimated and corrected for using the product of the pileup p_t density (ρ) and the jet area (A^{jet}), and is subtracted from the jet. A small pileup dependence on the jet p_t is still observed after this so a further correction based on the number of primary vertices (N_{PV}) and the average interactions per bunch crossing ($\langle\mu\rangle$) is applied. It is worth noting that for large radius jets (R=1.0) this step is not applied as it is unnecessary after the application of trimming described in subsection 4.5.2.

Finally, the jet energy and pseudorapidity are adjusted to give a better match to the MC truth value. The correction is derived as $\frac{E_{ptcl}}{E_{reco}}$ where E_{ptcl} is the particle level jet energy and E_{reco} is the reconstructed jet energy. The jets used are required to be well isolated and the correction is binned in detector pseudorapidity. The jet energy response before correcting is shown in Figure 4.7 for η and shows

a large difference that is corrected for between the particle and reconstructed energies.

Once the jets have been calibrated a further in-situ technique is applied. This is performed differently for jets in the forward and central regions of the detector and differently again for high p_T jets. The calibration is derived by exploiting the momentum balance of a jet recoiling from a well-measured reference object. Central jets are calibrated using photons or Z bosons. The forward region is calibrated by using a well-calibrated jet from the central region recoiling from a jet in the forward region. High-p_T jets are calibrated using the recoil of a group of low p_T jets. The data-to-MC ratio derived from each of these techniques is shown in Figure 4.8. This is used to correct the jet p_T to produce what are known as EM+JES jets [53].

Jet Energy Resolution (JER)

The JES corrects the central value of the jet energy measured in the detector but it is also important to correct the precision of the measurement. The precision of the measurement is limited by the detector resolution but it is also affected by electronic noise and pileup leading to a wider jet mass peak. To correct for this a jet energy resolution correction is applied.

Firstly the resolution is parameterised as

$$\frac{\sigma(p_T)}{p_T} = \frac{N}{p_T} \oplus \frac{S}{\sqrt{p_T}} \oplus C\,, \tag{4.6}$$

where N, S and C are the electronic and pileup noise, calorimeter sampling noise and constant terms respectively. These terms are then measured looking at momentum balance in both dijet and vector boson plus jet events and a combined

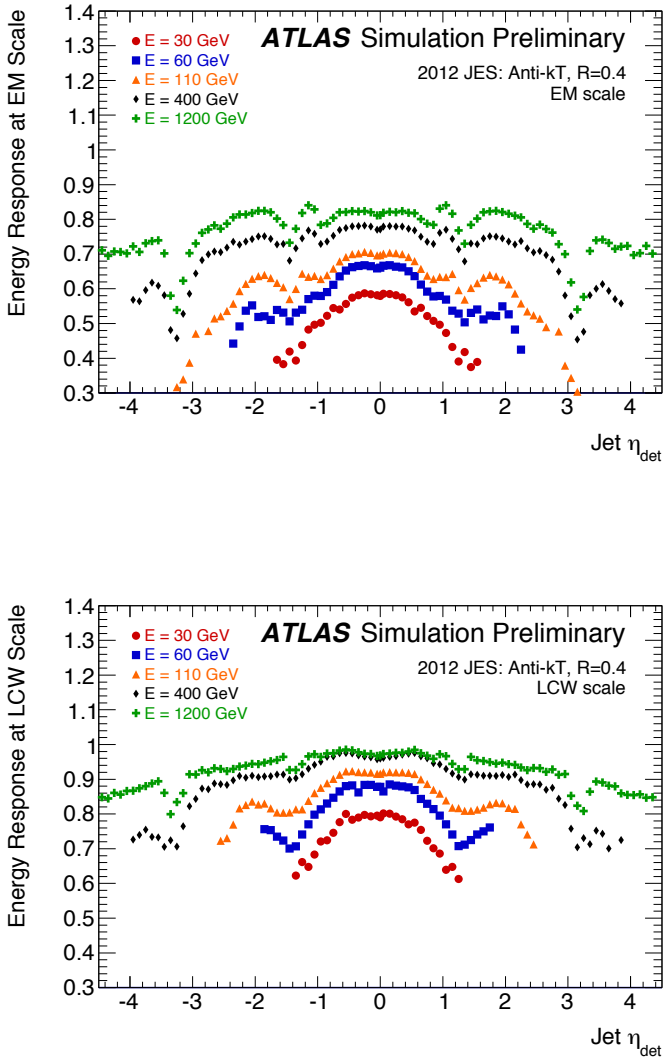

Figure 4.7: Effect of the MC based jet correction on EM scale (left) jets and LCW scale (right) jets (taken from [12]).

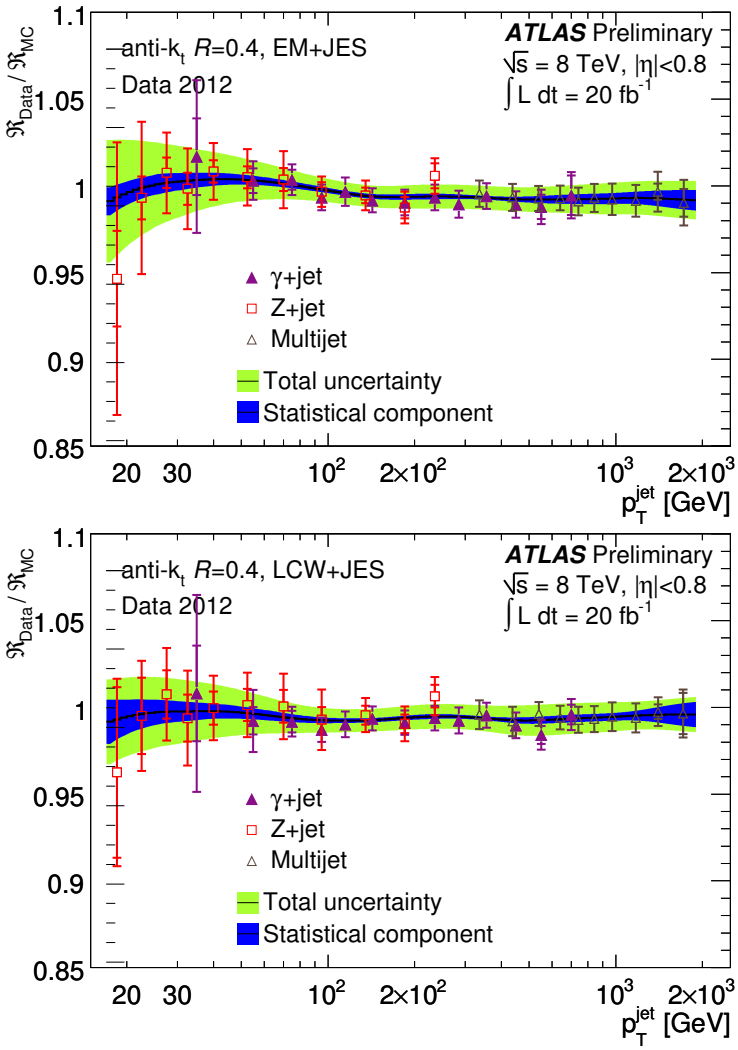

Figure 4.8: Effect of the in-situ jet correction derived from jets recoiling from a reference object (taken from [12])

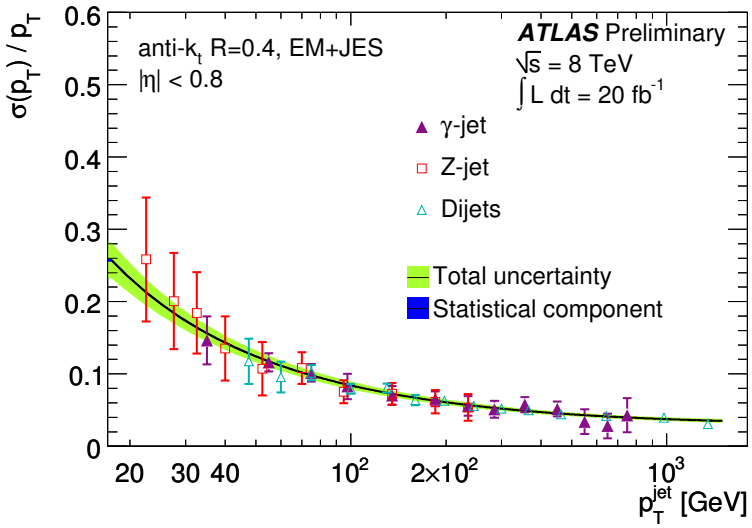

Figure 4.9: Effect of the jet energy resolution correction as a function of jet p_T (taken from [12]).

fit using Equation 4.6 performed. The JER is split into different η regions because different detector regions will show a different response. The resolution as a function of p_T is shown in Figure 4.9 for the central region. The uncertainty on the JER ranges from 3% at 20 GeV to less than 1% above 100 GeV.

Global Sequential Calibration (GSC)

The GSC is a correction designed to improve the jet energy resolution without changing the average energy scale. It uses the topology of calorimeter energy deposits, and tracking information. This allows the technique to incorporate information about the particle content of the hadronic shower. It also uses information from the muon chamber about events that are not fully contained in the hadron calorimeter. The GSC is applied after the JES and includes corrections from several variables that are applied sequentially.

Some of the reasons for the poor jet response are non-compensation of the calorimeter, energy deposits from jets ending up in the muon chambers, differ-

ences relating to parton flavour, and inactive detector areas. To understand the energy lost to the muon chamber the number of partial tracks constructed in the muon chamber ($N_{segments}$) behind the jet is used. To try to understand the contents of a jet the number of tracks associated with jets (n_{trk}) and the $width_{trk}$ variable,

$$width_{trk} = \frac{\sum_i p_T^i \Delta R(i, jet)}{\sum_i p_T^i} \tag{4.7}$$

where the sum is over the tracks in a jet are used. Also used are the fractions of energy deposited in the different longitudinal compartments of the calorimeter. Each correction in the sequence is derived as the inverse of the jet response for each variable. The resolution improvement as a function of p_T is show in Figure 4.10 for the various η regions. Improvements of up to 10% in resolution are seen compared to the resolution after applying the EM+JES corrections.

4.5.7 Jet Mass Scale and Resolution

For highly boosted objects all the decay products can be captured inside a single large radius jet. The properties of this large radius jet are used to distinguish between hadronically decaying massive particles and multijet production. Techniques for studying the structure of large radius jets are referred to as jet substructure techniques. One of the simplest variables to look at is the jet mass. If all the decay products of a decaying massive particle are captured in the jet then the reconstructed mass should relate to the mass of the particle, whereas this is not the case for multijet production. To check and correct the modelling of the jet mass in the ATLAS detector a jet mass scale (JMS) and jet mass resolution correction (JMR) are derived.

The JER and JES are derived using the conservation of momentum. Since

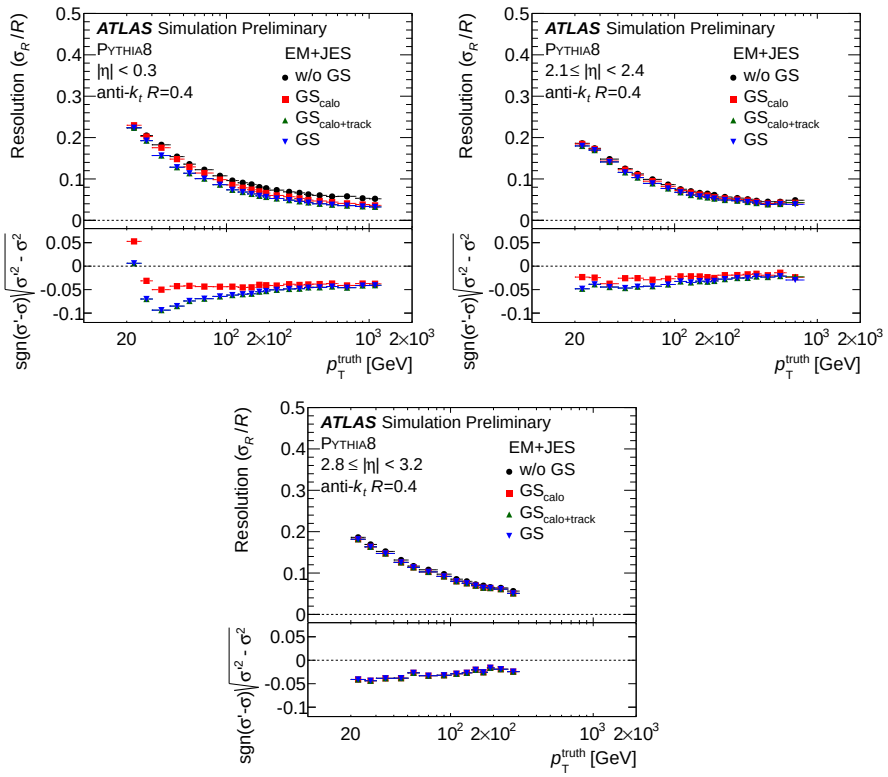

Figure 4.10: Effect of the global sequential calibration (GSC) as a function of the true jet p_T in three η regions (taken from [13]).

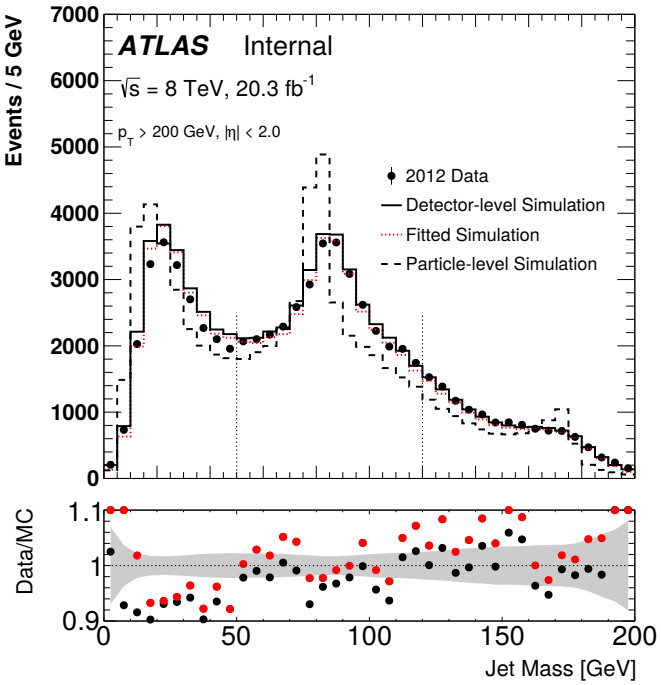

Figure 4.11: Effect of the jet mass scale correction on high p_T jets (taken from [14]). The red points are the ratio of the data to the fitted simulation and the blue points are the ratio of the data to detector-level simulation.

there is no conservation rule for mass we must find another way to correct the jet mass. This is done using lepton+jets $t\bar{t}$ events and fitting the reconstructed W boson mass peak to the particle level peak to determine the mass scale and resolution. The effect of this fit is shown in Figure 4.11. The relative JMS and JMR are both ~ 1 with an uncertainty of 0.3% for the JMS and 5-8% for the JMR [14].

4.6 b-tagging

Identifying which flavour of hadron decayed to produce a particular jet in our detector is a challenging problem at hadron colliders. However the relatively long lifetime of b-hadrons makes it possible to distinguish those from other flavours

of quarks. The lifetime of b-hadrons is $\sim 1 \times 10^{-12}$ s which translates to a travel distance of ∼3 mm in the detector. b-tagging algorithms exploit this fact by looking at information such as the impact parameter and the secondary vertex position. These algorithms are important for the analyses presented in Part III.

4.6.1 Calorimeter jet b-tagging algorithms

The primary algorithm used for calorimeter jets in ATLAS is called the MV1c algorithm. It is a derivative of the MV1 algorithm trained to enhance the c-jet rejection. Both are neural network based algorithms that are trained using simpler b-tagging algorithms outputs as the input variables. These algorithms are called IP3D, SV1 and JetFitter.

The IP3D algorithm identifies b hadrons by the transverse and longitudinal impact parameters of tracks associated with a particular jet. The transverse impact parameter is defined as the distance of closest approach to the primary vertex in the $r - \phi$ plane and the longitudinal impact parameter is defined similarly for the z coordinate. These variables are signed. If the distance of closest approach is in front of the primary vertex then the impact parameter is positive; otherwise it is negative. b-hadrons tend to have a positive value. A likelihood ratio using a 2-dimensional histogram of the significance of these two variables is used to perform the b-tagging in this algorithm [54].

The SV1 algorithm relies on properties of the secondary vertex. To reconstruct this vertex all the tracks associated with the jet are taken and paired together, by projecting their path backwards, to form vertices. The position of each vertex should be the secondary vertex position if the pair originated from the decay of the b hadron and not some other source such as a pileup interaction. An iterative χ^2 fit is performed removing the worst tracks until the fit is good. Then

several variables are examined: the invariant mass of all tracks associated with the vertex, the ratio of the sum of track energies in the vertex to those in the jet, and the number of two track vertices. Again a likelihood ratio is used to calculate the b weight [54].

The JetFitter algorithm uses a Kalman filter to fit a common line to the primary vertex and the b and c vertices in the hadron decay chain. This means that the b and c vertices are not always merged so that the flight length significances can be used, alongside similar variables used in the SV1 algorithm, to perform a likelihood discriminant [54].

The outputs from these three algorithms are used as variables to train the neural network for the MV1c algorithm. The MV1c algorithm allows for upper and lower cuts to be applied to the tagging weight. This means that analyses can be split into regions of different b-jet purity to enhance their sensitivity. Three different working points are employed in one of the analyses, described in Part III referred to as Loose, Medium and Tight [15].

4.6.2 b-tagging uncertainties

The performance of a b-tagging algorithm is described by ϵ_b, the efficiency of tagging a b-jet, and the probability of b-tagging a light or charm jet as a b-jet (ϵ_l and ϵ_c) where a light parton is u, d, s quarks, and gluons. The light jet rejection is shown as a function of the b-tagging efficiency in Figure 4.12. Working points are defined by the b-jet efficiency measured in simulation, and data/MC scale factors are derived by measuring the tagging efficiency in data. For the b-tag efficiency the efficiency in data is measured by looking at fully leptonic $t\bar{t}$ decays and using a likelihood function based on the p_T and tag weight of the two b-jets in the decay. The efficiencies and scale factors derived for the 70% working point

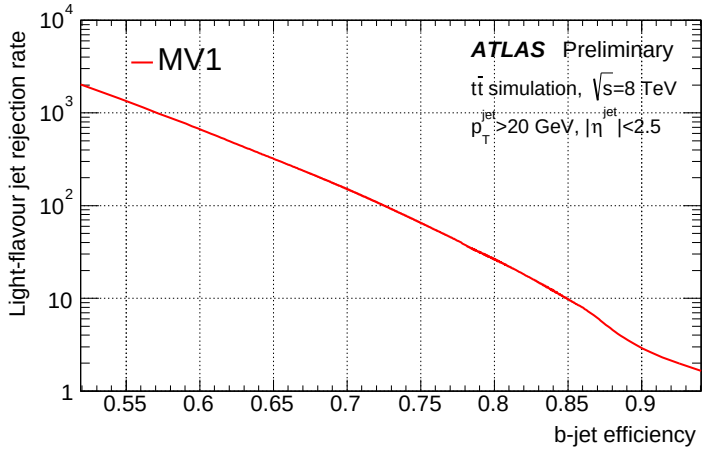

Figure 4.12: Light jet rejection rate as a function of b-jet efficiency for the MV1 b-tagging algorithm (taken from [15])

as a function of p_T are show in Figure 4.13. The total uncertainty on the sacle factors is $\sim 2\%$ [16].

4.6.3 Track jet b-tagging algorithms

Track jet b-tagging offers advantages over calorimeter b-tagging. The ability to reject pileup when using tracks is greater than when using calorimeter deposits. For calorimeter jets this increased pileup can change the direction in which the jet axis points; this is something to which b-tagging algorithms are sensitive as they rely on good measurements of the impact parameter and the position of the different decay vertices in the b hadron decay chain. Track jets, with their reduced sensitivity to pileup, will give more accurate values for these parameters.

Track jets reject pileup by requiring that the tracks used in the jet reconstruction be tightly matched to the hard scatter. This gives a good measurement of the jet axis but removes tracks from the jet that could help discriminate between different jet flavours. To compensate for this a second track association is performed after the jet axis has been determined to associate tracks with looser

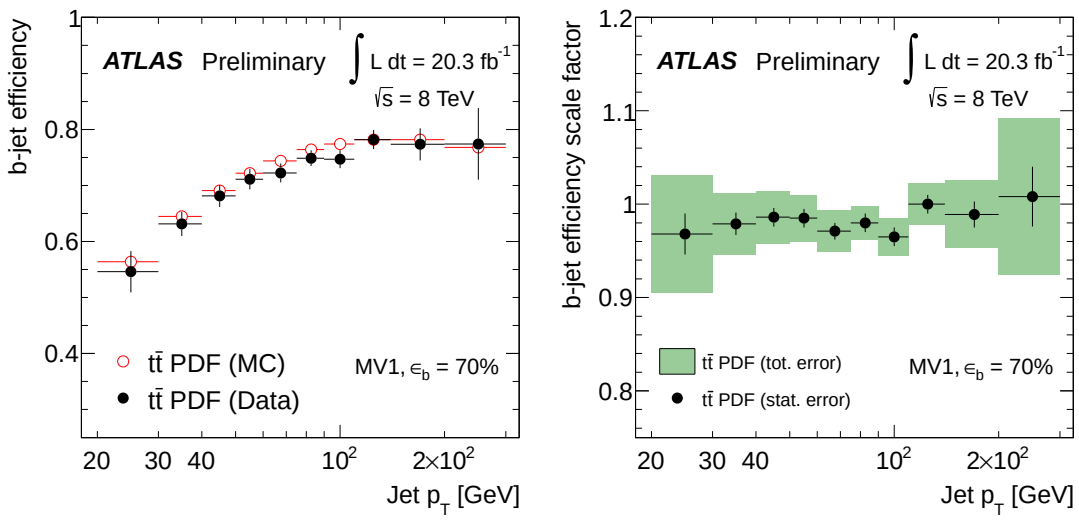

Figure 4.13: b-jet efficiency as a function of p_T for data and MC (left) and the resulting efficiency scale factor (right) as a function of p_T for the 70% efficiency working point derived from $t\bar{t}$ events (taken from [16]).

impact parameters to the jet. Only track jets with $p_T > 7\,\text{GeV}$ and $|\eta| < 2.5$ are used as below this threshold the light jet rejection is poor. The tracks in these jets are used as the inputs to b-tagging algorithms. The MV2c20 algorithm is the algorithm that is used in the work presented in Part III. It is a boosted decision tree based algorithm that uses jet properties and information from the IP3D, SV1 and JetFitter algorithms in a similar fashion to the MV1c algorithm. Currently these algorithms are all trained on calorimeter jets, a retraining on track jets would improve the performance. The calibration scale factors and systematic uncertainties are derived similarly to the calorimeter based b-tagging. The c-and light-jet rejection as a function of the b-tagging efficiency is shown in Figure 4.14 [17, 55].

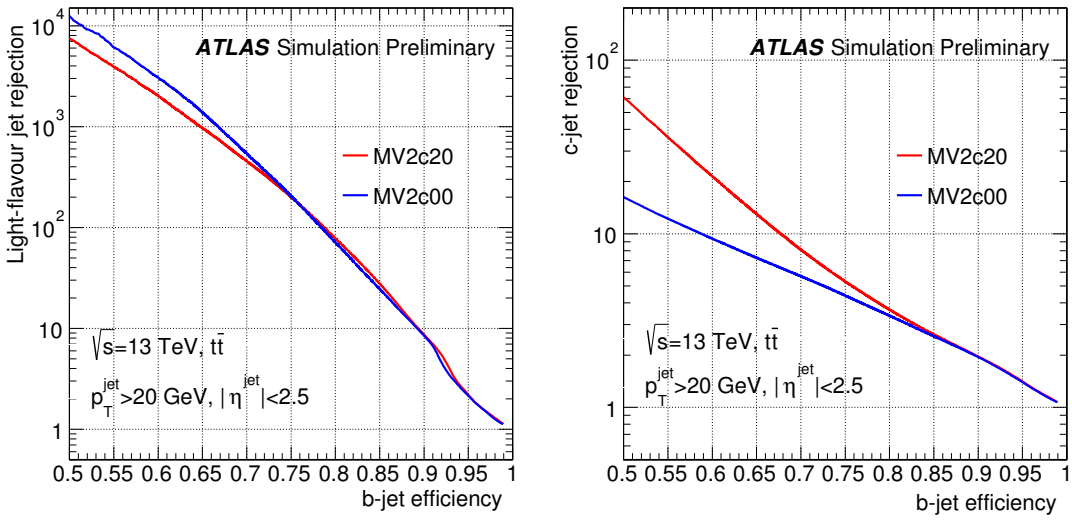

Figure 4.14: Light jet (left) and c-jet (right) rejection as a function of b-jet efficiency for the MV2c00 and MV2c20 algorithms (taken from [17]).

4.7 MET

Due to the conservation of momentum the vector sum of the transverse momentum of the collision products should be zero. Any imbalance in this is referred to as E_T^{miss}. This can indicate the presence of weakly interacting particles in the final state, most commonly neutrinos but large E_T^{miss} is often a signal in BSM searches [56]. The measurement of E_T^{miss} can be affected by particles that fail to be reconstructed, are poorly reconstructed, or that escape the detector acceptance.

E_T^{miss} reconstruction in ATLAS uses reconstructed, calibrated objects when calculating the momentum imbalance. It is calculated as

$$E_{x(y)}^{miss} = E_{x(y)}^{miss,e} + E_{x(y)}^{miss,\gamma} + E_{x(y)}^{miss,\tau} + E_{x(y)}^{miss,jets} + E_{x(y)}^{miss,\mu} + E_{x(y)}^{miss,soft} \quad (4.8)$$

These objects are reconstructed in the order: electrons, photons, hadronically decaying taus, jets, and muons. The soft term is then defined as any momentum

deposits in the detector not associated with one of these objects, and arises from underlying activity and soft radiation from a hard scatter. From this we can calculate E_T^{miss} magnitude and angle:

$$E_T^{miss} = \sqrt{(E_x^{miss})^2 + (E_y^{miss})^2} \tag{4.9}$$

$$\phi^{miss} = \arctan(\frac{E_y^{miss})^2}{E_x^{miss})^2}) \,. \tag{4.10}$$

To reconstruct these objects we can use either the calorimeter or the tracker. The technique for reconstructing E_T^{miss} in the calorimeter is called CST (calorimeter soft terms) E_T^{miss}. It is sensitive to pile-up and can lead to extra energy contributing to the soft term because it is constructed from calorimeter deposits that are not added to any other objects. This is the standard definition used in Run 1. An alternative to this is to reconstruct all objects in the tracker using its superior resolution. This gives a good E_T^{miss} estimation but is let down by the lower angular coverage of the tracker and the fact that neutral particles are not measured.

A compromise between these two methods is the Track Soft Terms (TST) method. This builds all objects from the calorimeter except the soft term which is built from tracks in the inner detector that are associated with the hard scatter vertex. Tracks that fall within $\Delta R = 0.05$ of an electron or photon are excluded; similarly those within $\Delta R = 0.2$ of a hadronically decaying tau. Tracks ghost-associated with a jet are removed and ID tracks from combined or segment tagged muons are replaced by a combined fit to the ID and MS tracks. A comparison of the three MET reconstruction techniques is shown in Figure 4.15. For high E_T^{miss} the performance of CST and TST are similar but TST gives a better estimation

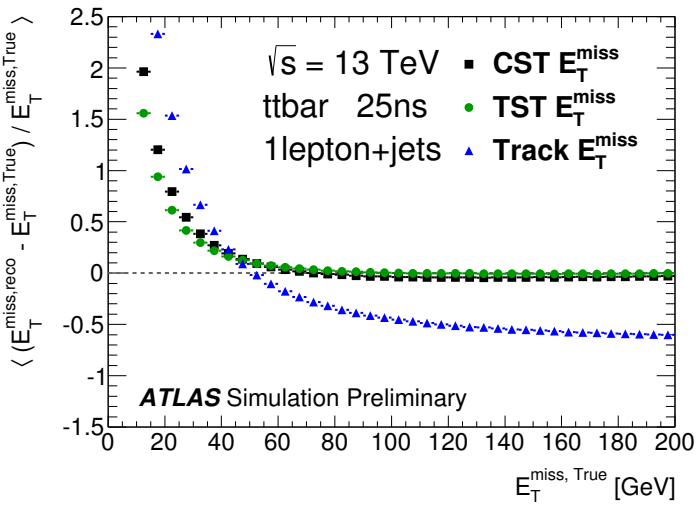

Figure 4.15: Comparison of the resolution of three E_T^{miss} reconstruction methods as a function of the true E_T^{miss} (taken from [18]).

at low E_T^{miss} [18].

Part III

The following section describes work on two analyses. The first is the Run 1 VH $H \to b\bar{b}$ analysis which is described in chapter 5. The second is an analysis performed using data from Run 2 to search for new physics beyond the standard model with a similar signature to the Run 1 analysis. This is described in chapter 6 and is called the VH resonance analysis.

The Run 1 analysis is not a complete summary of the analysis as the author contributed particular studies to this analysis.

Chapter 5

Hbb Analyses

This chapter describes some studies performed on the Run 1 dataset of 20.3 fb^{-1} at 8 TeV in the context of the search for WH associated production of the Standard Model Higgs Boson. This analysis was published in 2015 [57]. The final state of this search is W$\rightarrow l\nu$ and H$\rightarrow bb$. Both a multivariate analysis and a cut-based analysis were performed; the latter is the focus of this section and the former constitutes the publish work in [57].

5.1 Object and Event Selection

In the W$\rightarrow l\nu$ analysis, events are selected using a single lepton trigger with an E_T threshold of 24 GeV for electrons and a p_T threshold for muons of 24 GeV. Both these triggers have isolation criteria and so are complemented with higher threshold triggers (an E_T threshold of 60 GeV for electrons and a p_T threshold for muons of 36 GeV) that have no isolation criteria. Events are required to have one tight lepton and no additional loose leptons and the objects that satisfy the trigger are required to be matched to the reconstructed objects. Here a loose

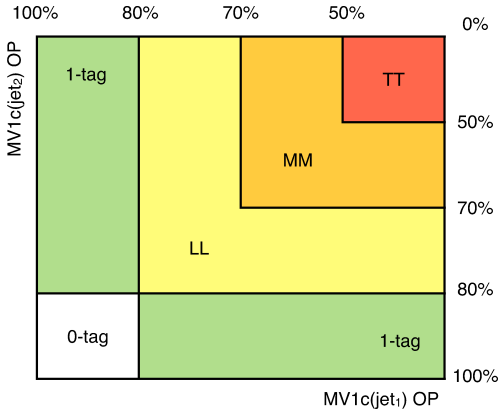

Figure 5.1: Diagram of the different MV1 b-tagging categories used in the $H \to b\bar{b}$ analysis. L is loose, M is medium and T is tight.

lepton is defined as passing the VeryLooseLH criteria for electrons and Tight MuID for muons.

The selection applied to jets requires exactly 2 or exactly 3 jets with $p_T > 25\,\text{GeV}$ and $|\eta| < 2.5$. Events with an extra jet with $p_T > 30\,\text{GeV}$ and $|\eta| > 2.5$ are rejected to reduce contributions from $t\bar{t}$. The b-tagging algorithm used is the MV1 algorithm with 3 working points as shown in Figure 5.1. There must be no more than 2 b-tagged jets and one must have $p_T > 45\,\text{GeV}$. Events in which the third jet is also b-tagged are rejected. The separation of the analysis into three b-tagging categories (TT, MM, LL) helps constrain backgrounds not containing two real b-jets. Further topological selection criteria are applied according to p_T^W, defined as the magnitude of the vector sum of the lepton transverse momentum, m_T^W, the transverse mass of the reconstructed W boson, and E_T^{miss}. There are five p_T^W intervals with boundaries at 0, 90, 120,160 and 200 GeV. The more boosted categories have a higher signal to background ratio which helps to improve our sensitivity. Additional selection criteria are shown in Table 5.1.

The prefit yields for each background in the 1 lepton channel after the full event selection are shown in Table 5.2. The largest backgrounds are W+jets, t$\bar{\text{t}}$

p_T^W bins [GeV]	0-90	90-120	120-160	160-200	> 200
ΔR(jet_1, jet_2)	0.7-3.4	0.7-3.0	0.7-2.3	0.7-1.8	<1.4
m_T^W [GeV]	< 120				
H_T [GeV]	> 180		-		
E_T^{miss} [GeV]	-		> 20		> 50

Table 5.1: Extra topological selection applied in the 1 lepton channel in bins of p_T^W. H_T is the scalar sum of the 2 jet momentas, lepton momentum and E_T^{miss}. m_T^W is the transverse mass of the W boson reconstructed from the lepton and E_T^{miss}.

and single top.

The multijet background is significantly smaller than W+jets, $t\bar{t}$ and single top but is the largest of all the other backgrounds and accounts for 3-5% of the overall background. Modelling it with Monte Carlo is not possible due to constraints on computing power and a data driven technique must be used. These two facts make it a tricky background to control and a poor estimate of its characteristics and size could have a detrimental effect on the final result.

5.2 Multijet Modelling Procedure

The modelling of the multijet (MJ) background in this analysis was not done using Monte Carlo but instead using a data driven technique. This technique involves generating a "multijet template". A fit is then performed using this template and the Monte Carlo simulations of the other backgrounds to data. The normalisation of both of these are allowed to float in the fitting procedure to find their best fit values.

The multijet template is selected from data using the nominal event selection with some modifications to the lepton isolation selection criteria in order to select a fairly pure multijet sample. The contribution of the electroweak backgrounds

Table 5.2: Signal, background and data yields in the different 2 b-tag categories for 2 and 3 jets in the H $\rightarrow$ b$\bar{\text{b}}$ analysis. The W/Z+jets backgrounds are split by quark flavour with l representing light flavours (u,d,s), c representing charm and hf representing heavy flavours (t, b). $MJ_{e/\mu}$ is the multijet background split by lepton category [20].

Sample	Yield		
	LL	MM	TT
2 jet			
VH	16.8	26.1	29.9
VV	130.4	83.7	68.0
$t\bar{t}$	1659.8	1914.2	1713.6
s-top	844.6	751.1	591.9
W+l	1429.0	103.0	2.9
W+cl	2102.7	362.6	18.6
W+hf	1776.4	1175.0	655.5
Z+l	87.4	6.6	0.1
Z+cl	53.5	10.9	0.5
Z+hf	125.5	95.5	65.2
MJ_e	57.7	32.9	15.2
MJ_μ	517.1	262.9	108.4
Total	8800.8 $\pm$ 827.7	4824.6 $\pm$ 408.8	3269.6 $\pm$ 300.3
Data	9190.0 $\pm$ 183.3	5271.0 $\pm$ 139.5	3753.0 $\pm$ 115.5
3 jet			
VH	5.6	8.9	10.0
VV	60.7	30.6	22.8
$t\bar{t}$	3187.0	3769.9	3621.1
s-top	605.2	547.5	432.9
W+l	558.7	37.6	1.0
W+cl	802.7	132.7	6.4
W+hf	769.2	482.9	270.4
Z+l	35.8	2.5	0.0
Z+cl	25.6	4.2	0.1
Z+hf	59.5	44.1	32.8
MJ_e	15.2	8.3	3.3
MJ_μ	150.3	77.7	37.7
Total	6275.6 $\pm$ 805.5	5147.1 $\pm$ 865.5	4438.7 $\pm$ 844.6
Data	6304.0 $\pm$ 155.5	5398.0 $\pm$ 138.9	4581.0 $\pm$ 122.9

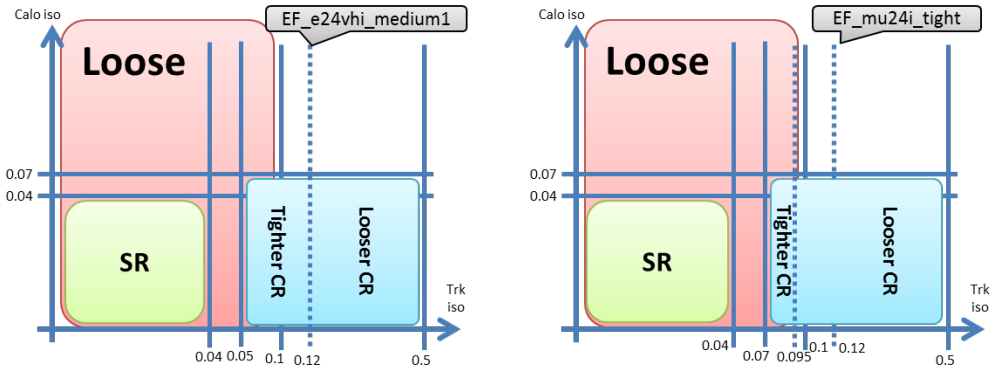

(a) Electron (b) Muon

Figure 5.2: The 1 lepton isolation selection criteria for electrons and muons. The blue box represents the multijet template region. For electrons the Tight CR is used for the nominal template and the Loose CR for the systematic variations. For muons the inclusive CR is used for the nominal while the Tight and Loose regions are used for up and down systematics respectively on iso_{track} cut.

to this sample is estimated by applying this event selection to the Monte Carlo simulated electroweak backgrounds. This contribution is subtracted from the data sample to give the final multijet template used in the fit. The modifications to the electron isolation selection is shown in Figure 5.2. Both the calorimeter and track isolation were studied as possible template regions but modifying the track isolation was shown to give better results [20].

5.3 Impact Parameter Studies

In previous versions of this analysis a cut on the impact parameter (d_0) of the lepton of less than 0.1 mm was used which helped to reduce the multijet background. For electrons associated scale factors are required when applying this cut but these are time consuming to calculate so the effect of removing the cut in the electron channel was studied. Figure 5.3 shows a comparison of the p_T of the lepton with and without the cut on d_0 and the same comparison is shown for the

Table 5.3: Comparison of MJ to data ratio in each b-tag category with and without the d_0 cut.

	2LTag		2MTag		2TTag	
	D0 cut	No D0 cut	D0 cut	No D0 cut	D0 cut	No D0 cut
MJ/Data	0.07	0.13	0.19	0.26	0.02	0.08

E_T^{miss} variable in Figure 5.4, and both of these are for the tightest b-tag region and require 2 tagged jets. These variables were chosen as they are both part of our selection criteria in the analysis and show clearly the increase in the multijet background. Table 5.3 shows the MJ yields as a fraction of data for each b-tag region. In every case the removal of the d_0 cut causes a large increase in the MJ background, however it was decided that this increase was not large enough to cause a problem in the analysis since the multijet background has a small overall contribution to the total background.

5.4 Improving Multijet Statistics

When the selection criteria for generating the multijet template have been applied the statistics are reasonable, however once the b-tagging has been applied the statistics in the 2-tag category is quite poor. This can make the multijet fitting procedure unstable and it often fails to converge. To overcome this problem, 1-tag events are used in the 2-tag template. The technique used to do this is called spoofing.

Spoofing uses 1-tag events and takes the MV1c value of the tagged jet and whether it is leading or subleading in p_T. From these two pieces of information it generates an MV1c value for the untagged jet making this event a 2-tag event that can be used to improve the 2-tag multijet statistics without changing the overall b-tag distribution. This is done using a distribution that compares the tag

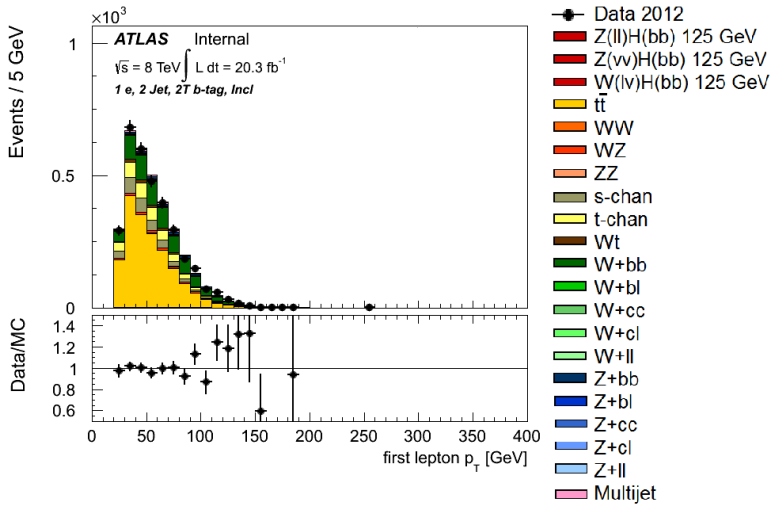

(a) p_T of the lepton with d_0 cut

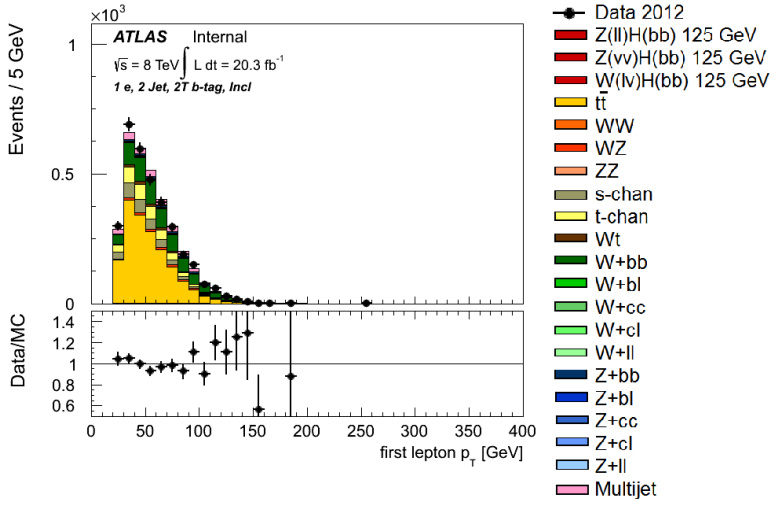

(b) p_T of the lepton without d_0 cut

Figure 5.3: Comparison of the p_T of the electron with and without the d_0 cut in the 2T b-tag region. The MJ contribution is in magenta.

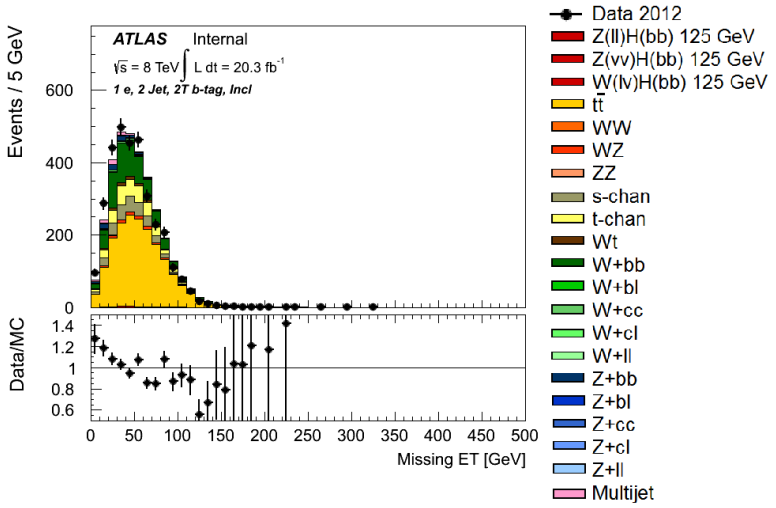

(a) E_T^{miss} with d_0 cut

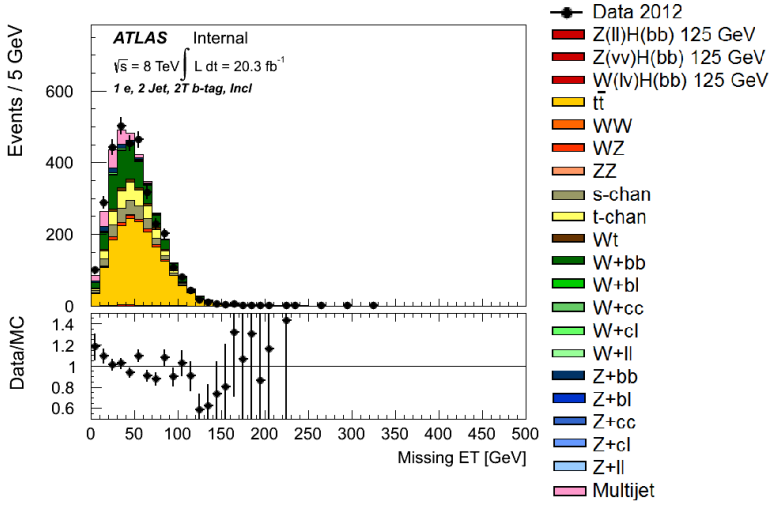

(b) E_T^{miss} without d_0 cut

Figure 5.4: Comparison of the E_T^{miss} with and without the d_0 cut in the 2T b-tag region. The MJ contribution is in magenta.

weights for the leading and subleading jets in 2-tag events and is done separately for electron and muon events.

5.4.1 Validation of Spoofing

In order to validate the spoofing technique the analysis framework was run with spoofing applied and without spoofing applied. Figure 5.5 shows the distribution of MV1c for the first jet as a function of MV1c for the second jet for both cases. A clear difference between the two distributions is observed. This shows that the application of spoofing is changing the shape of the b-tagging distribution in a way that is not representative of the 2-tag distribution, implying that the b-weight shape is different in the 1-tag distribution. To overcome this a reweighting is applied to the events as part of the spoofing derived from the ratio of the 2-tag to 1-tag MV1c weight. This is applied separately for leading and subleading jets and for electron and muon events. A comparison between no spoofing and the reweighted spoofing is shown in Figure 5.6 and the differences between the two distributions are now within the Poisson uncertainty.

5.4.2 Kinematic Differences

Further validation of the spoofing technique was performed by looking at the effects of spoofing on a few of the kinematic distributions. Figure 5.7, Figure 5.8 and Figure 5.9 show the comparison of a few variables with and without the application of spoofing after the multijet fit. The difference is most pronounced in the p_T of the electron, Figure 5.7, where there is a clear change in the slope of the ratio plot due to the concentration of the multijet background at low momentum. The effect of the spoofing procedure on the shape of the multijet

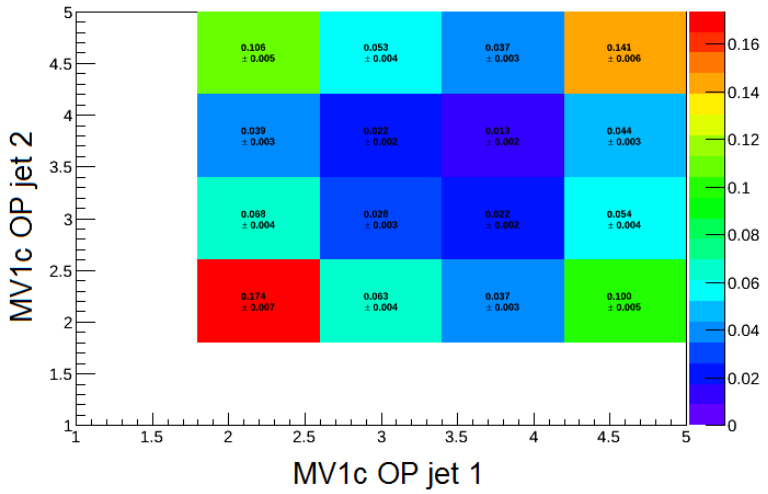

(a) MV1c operating points normalised to unit area with no spoofing applied

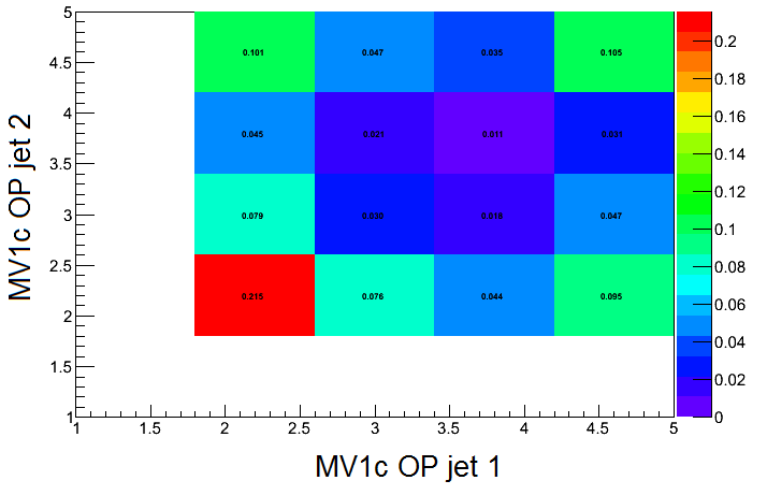

(b) MV1c operating points normalised to unit area with spoofing applied

Figure 5.5: Comparison of b-tag values with and without spoofing for electron events

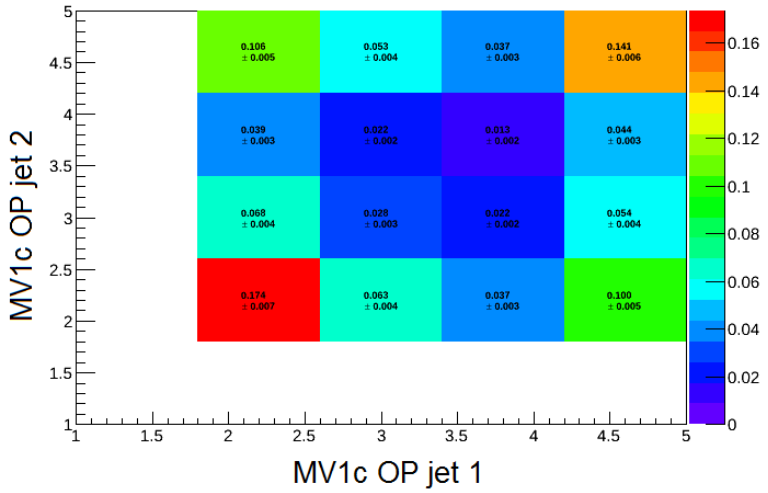

(a) MV1c operating points normalised to unit area with no spoofing applied

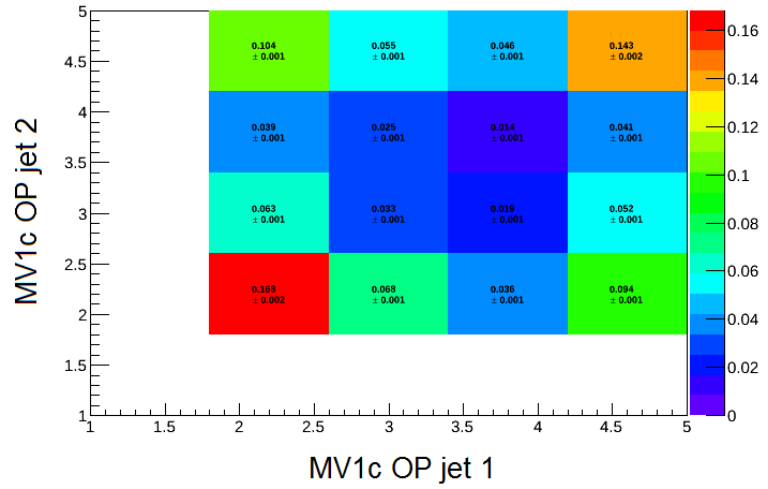

(b) MV1c operating points normalised to unit area with reweighted spoofing applied

Figure 5.6: Comparison of b-tag values with reweighted spoofing and without spoofing for electron events

Table 5.4: Comparison of electroweak and MJ scale factors derived from the MJ fit with and without spoofing.

	MJ Scale Factor	EW Scale Factor
No Spoofing	0.55	1.08
Spoofing	0.40	1.10

background can also be seen in Table 5.4 which shows the scale factors applied to the multijet and electroweak backgrounds by the fitting procedure. These are the scale factors that when applied to the multijet template and the electroweak contribution to the multijet region give good agreement with the data in that region. The multijet scale factor shows a large change when the fit is performed with spoofing applied.

In order to correct for these kinematic differences a further reweighting is applied to the promoted events. It is applied sequentially to the $\Delta R(b,b)$ and p_T^W using the ratio of the 1-tag to 2-tag events. "Real" 2-tag events make up about 10% of the final 2-tag MJ template with the rest being events that have been promoted from the 1-tag region. After these corrections the distributions with and without spoofing give good agreement.

5.5 W+Jets Generator Comparison

The modelling of the W+Jets background is performed using the Sherpa generator, however a pure W+Jets control region to verify the modelling and estimate systematic variations could not be found. Instead, systematics were derived using generator comparisons between the nominal Sherpa samples and either Alpgen-Herwig, aMC@NLO or specially prepared Sherpa samples. The baseline Sherpa samples contain the matrix element for all flavour processes whereas the specially prepared sample contains only those for W+bb.

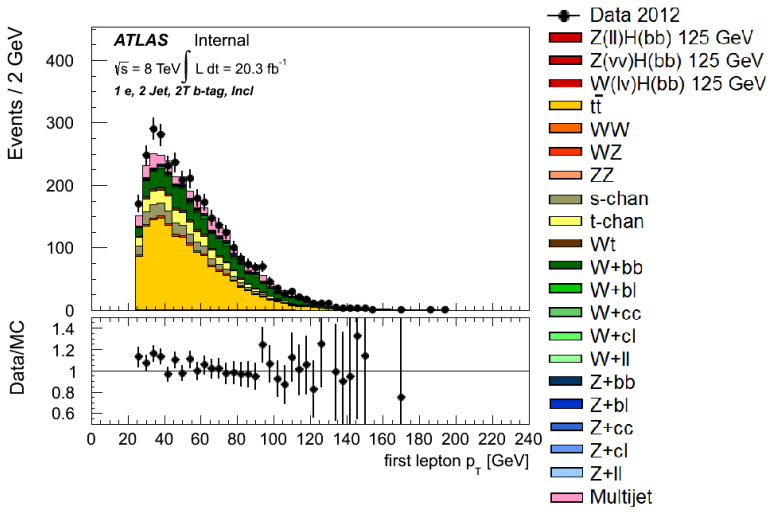

(a) p_T of the lepton without spoofing applied

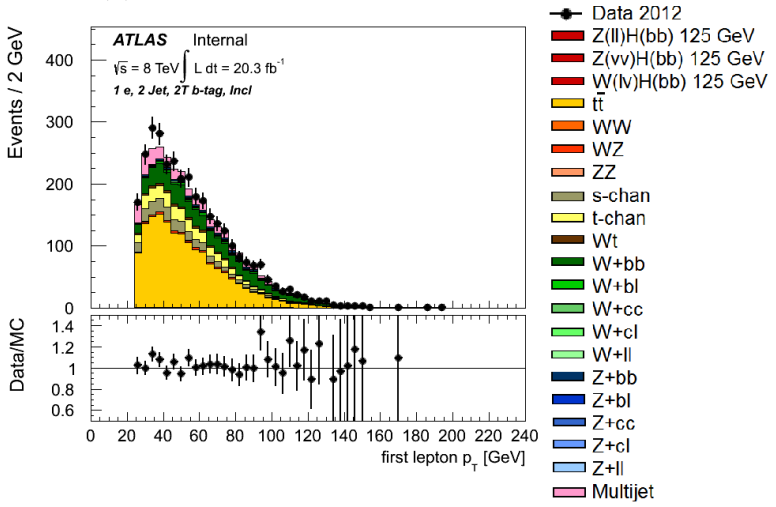

(b) p_T of the lepton with spoofing applied

Figure 5.7: Comparison of the p_T of the electron with and without spoofing in the 2T b-tag region.

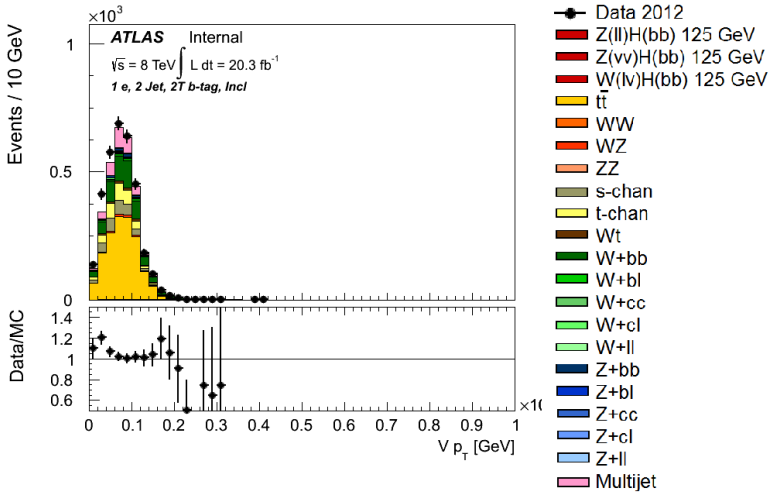

(a) p_T^W without spoofing applied

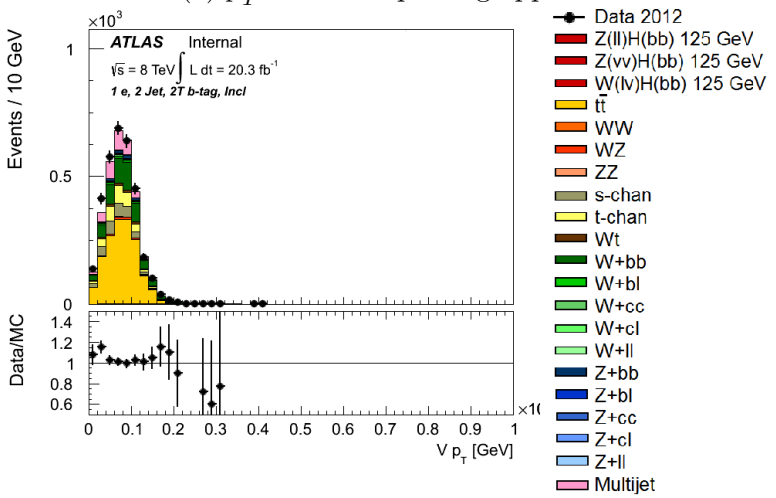

(b) p_T^W with spoofing applied

Figure 5.8: Comparison of the p_T^W with and without spoofing in the 2T b-tag region.

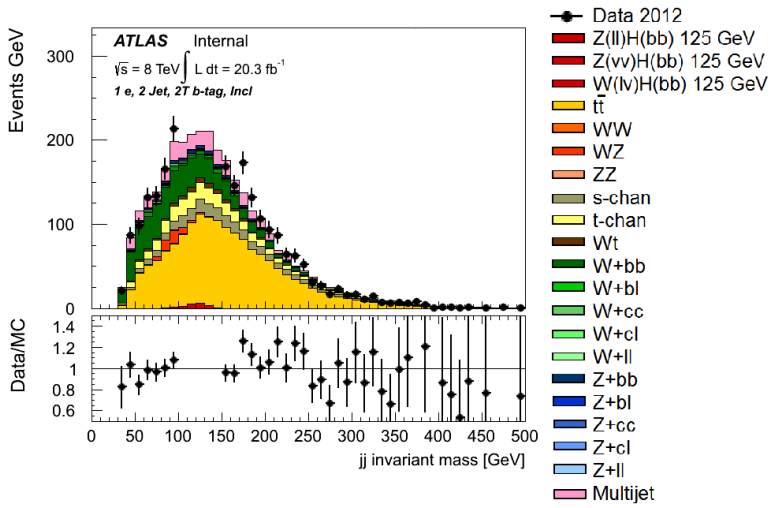

(a) m_{JJ} without spoofing applied

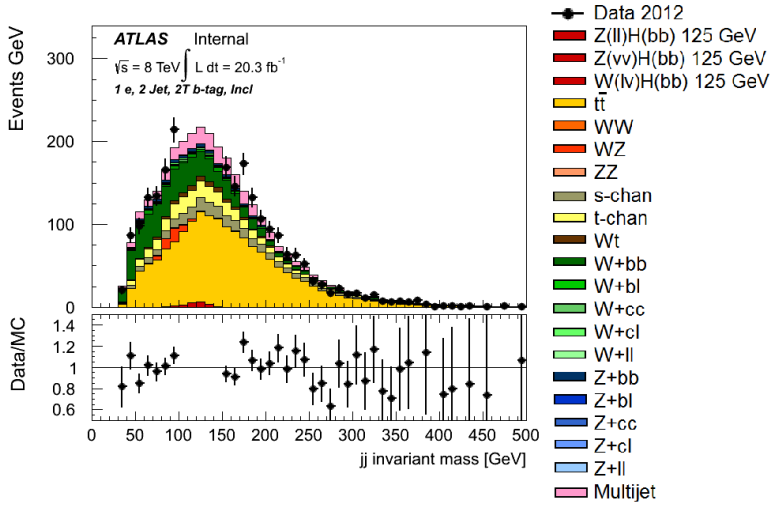

(b) m_{JJ} with spoofing applied

Figure 5.9: Comparison of the m_{JJ} with and without spoofing in the 2T b-tag region.

Generator comparisons can depend heavily on the choice of generator so a further crosscheck was performed comparing the nominal samples to AlpgenPythia, specifically looking at the flavour composition to make sure that there were no significant divergences. Figure 5.10 shows the dijet mass distribution split by flavour in the electron channel and the 2M b-tag category. Pythia shows a higher estimation of light flavours and lower heavy flavour composition than Sherpa. These differences are covered by systematics already applied to the various flavour fraction ratios derived from comparisons between Sherpa and aMC@NLO, which range from 12% to 35% depending on the flavour fraction and an additional systematic on the mJJ distribution.

One final observation from this study, shown in Figure 5.11 is the ratio of the number of events in the $p_T^V > 120GeV$ distribution to the $p_T^V < 120GeV$ distribution binned in ΔR between the two jets. A large difference is observed, AlpgenPythia has more high momentum events at low ΔR which could indicate a difference in the treatment of gluon-initiated production between the generators. While there is no explicit systematic on the gluon-initiated production of bb pairs, this difference is covered by a systematic uncertainty that is placed on the shape of the p_T^V distribution. For a full description of these systematics see [57].

5.6 Results

The limit setting procedure in this analysis was carried out using several regions. For details on this procedure and the incorporation of different regions in this calculation see section 6.6. The m_{bb} distributions in 2 jet and 3 jet regions are used and both are further divided into three b-tagging regions of increasing purity. These plots are also divided into the different p_t^W regions described in the event

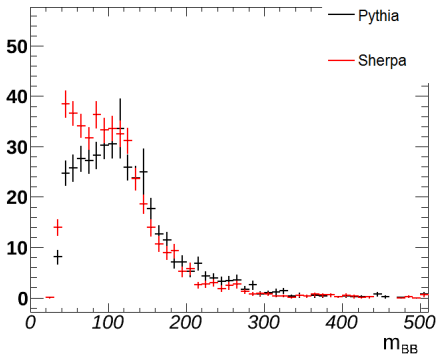

(a) W+bb flavour events in the 2M tag, electron channel

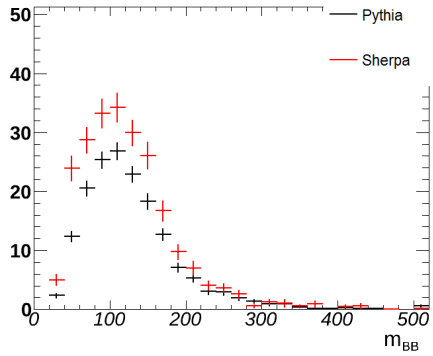

(b) W+cc flavour events in the 2M tag, electron channel

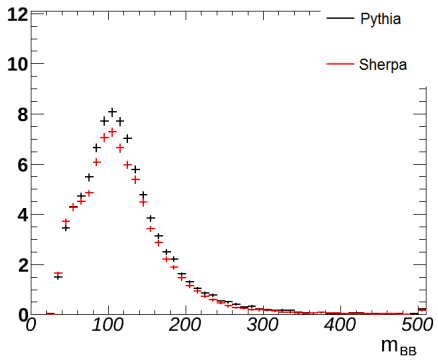

(c) W+ll flavour events in the 2M tag, electron channel

Figure 5.10: Comparison of the flavour composition of the Sherpa and Alpgen-Pythia samples

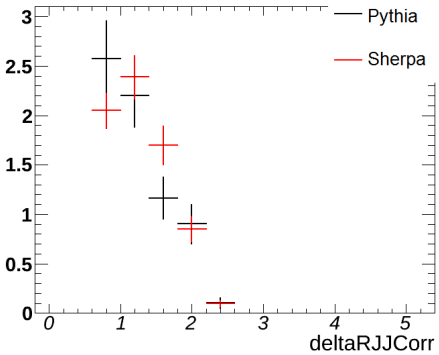

Figure 5.11: Ratio of High/Low p_T^V W+bb events in the 2M b-tag category

selection. In addition to this the MV1c distribution in the 1 tag, 2 and 3 jet regions are used. The binning of each of these histograms is optimised using an algorithm name TransformationD [20] that maximises the expected sensitivity. A few selected plots of these regions after the fit has been performed are shown in Figure 5.12 and all regions used in the fit can be found in Appendix C. The prefit background estimate is also shown as is the uncertainty.

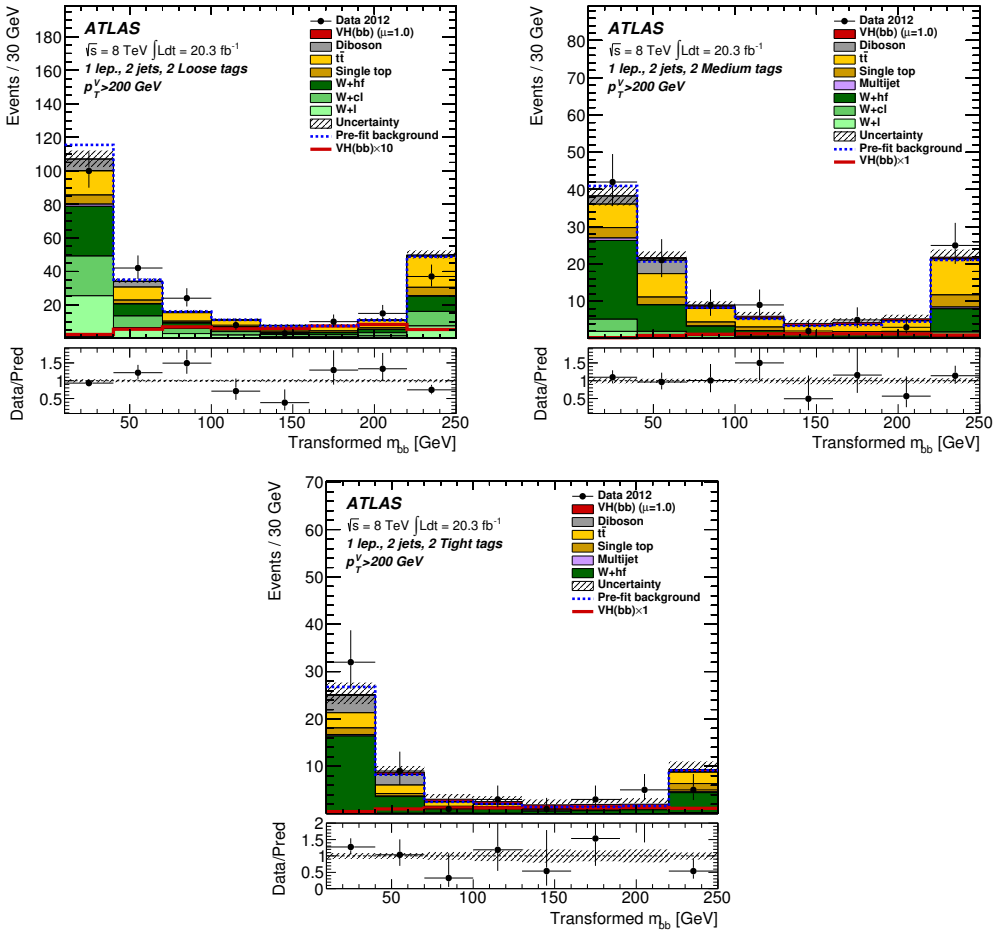

Figure 5.12: Postfit transformed dijet mass distribution in the 2 jet, $p_T^W > 200$ region with 2L tag (left), 2M tag (middle) and 2T tag (right) jets. The dashed blue line represents the prefit background.

The results of the limit setting procedure for a range of Higgs boson masses between 110 and 140 GeV in the 1 lepton channel using the 8 TeV dataset of

20.3 fb^{-1} can be seen in Figure 5.13. The limits are set on the cross section times branching ratio. The difference between the expected and observed limits can be explained by a downward fluctuation in the data observed in some of the more sensitive bins in the plots shown in Appendix C. The plots shows that the analysis is not sensitive to Higgs production that would be consistent with the standard model. This result is 67% correlated with the published MVA result [57, 20].

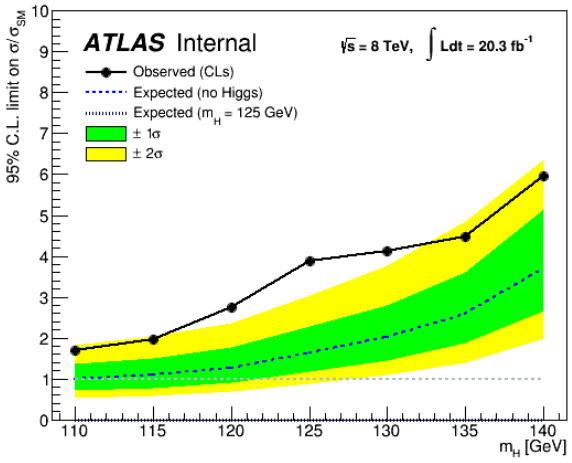

Figure 5.13: Final limit in the 1 lepton channel

Chapter 6

VH Resonance Analysis

In this chapter the analysis of the 2015 dataset consisting of 3.2 fb^{-1} of data at 13 TeV is presented. This search is intended to extend the Run 1 search for VH resonances [33]. These are high mass resonances that decay to a vector boson and a Higgs boson. They are present in many beyond the Standard Model (BSM) theories. A useful model for comparing experiment to theory is the the Heavy Vector Triplet (HVT) described in section 1.3 [58]. This model provided benchmarks to describe the sensitivity of this search and the results will be described in this section. The increased centre of mass energy should allow for an improvement in the limits of searches at high mass, consequently this search mostly focuses on improving the sensitivity of the "boosted" region with VH reconstructed mass above 1 TeV.

The final state for the models that will be probed are divided into three "channels". The zero lepton channel consists of Z$\rightarrow \nu\nu$, H$\rightarrow$bb; the one lepton channel W$\rightarrow$lν, H$\rightarrow$bb; and the two lepton channel Z$\rightarrow$ll, H$\rightarrow$bb.

6.1 Object Selection

6.1.1 Data And Simulated Samples

Events are required to pass a number of criteria using a Good Runs List that ensures that the detector was operating correctly.

The signal process of interest and all relevant background processes are simulated using Monte Carlo and the effect of pileup is simulated by adding minimum bias simulations to each event. The signal samples are generated using the MadGraph5 generator [59] for event generation with the NNPDF2.3LO PDFs and the Pythia8 generator [60] for the parton shower and hadronisation. The only free model parameters are the resonance mass (M_V) and the resonance coupling (g_V). The values chosen for these parameters can be found in Appendix A; the mass values probed range from 500 to 5000 GeV.

The standard model processes that have a similar final state to the signal model include Z+Jets, W+Jets, $t\bar{t}$, diboson production, single top production, and multijet. All of these processes with the exception of multijet are modelled using Monte Carlo simulations.

Z+Jets and W+Jets are modelled using Sherpa 2.1.1 for event generation and parton showering with the CT10 PDF and normalised to cross-sections calculated to NNLO [61, 62, 63]. $t\bar{t}$ is modelled using Powheg with the Powheg-BOX framework with the CT10 PDF and Pythia6 for showering with the CTEQ6L1 PDF, this sample is normalised to a cross-section calculated to NNLO+NNLL [64, 65, 66, 63, 67, 68]. For single top production Powheg with CT10 and Pythia6 with CTEQ6L1 were used and the cross-section taken from [69]. For diboson processes Sherpa with CT10 was used and the cross-section from [70].

Higgs production in association with a Vector Boson is predicted by the Stan-

dard Model but has not been observed experimentally as discussed in chapter 5. This would also be a background to this search. This process was simulated using Pythia8 for the quark initiated process and with Powheg plus Pythia8 for the hadronisation in the gluon initiated case. Both use the CT10 PDFs. A comprehensive listing of all the samples used in this analysis can be found in Appendix A.

6.1.2 Electrons

Electron reconstruction is discussed in detail in chapter 4. Electrons are reconstructed from calorimeter clusters. The clusters are found using the ATLAS sliding window algorithm. They are identified using the likelihood-based working points. For the 0-lepton category no electrons passing the "loose" working point are required; for the 1-lepton channel exactly one electron passing the "loose" working point is required; and for the 2-lepton channel exactly two "loose" electrons are required.

For all three channels, electrons are required to have $p_T > 7$ GeV and $|\eta| < 2.47$. An isolation requirement is applied such that the $\frac{\Sigma_{track}\ p_T}{p_T^l}$ of all tracks within a certain radius of the lepton is less than some isolation value I_0. This value is chosen such that the efficiency of reconstruction of dileptonic Z decays is 99% while the rejection of non-prompt leptons is maximised. The radius within which the isolation is calculated scales as $r(p_T^l) = min(0.2, \frac{10\,\mathrm{GeV}}{p_T^l})$ so that the radius shrinks as the lepton becomes more boosted. This is required as there is no single radius that can maintain good performance across the whole p_T^l spectrum.

6.1.3 Muons

Muons are reconstructed from calorimeter clusters that are matched to tracks or track segments in the muon spectrometer and use a likelihood based identification algorithm for all three lepton categories.

For all three channels muons must also have $p_T > 7$ GeV and $|\eta| < 2.7$. An isolation requirement is applied that is the same as in the electrons but with the radius defined as $r(p_T^l) = min(0.3, \frac{10\,\text{GeV}}{p_T^l})$.

6.1.4 Jets

Three types of jets are used in this analysis. The first are built from calorimeter clusters. They are anti-k_T jets with $R = 1.0$. The jets are reclustered with R_{sub} = 0.2 in order to apply trimming [71] with an f_{cut} of 5%. These jets are referred to as large-R jets.

The second are calorimeter jets also using the anti-k_T algorithm with a radius of 0.4 and are referred to as small-R jets. Both types of calorimeter jets are corrected by adding the energy of any muons contained within the jet to the total energy of the jet after subtracting the muon energy from the calorimeter cluster.

The third type of jets are track jets. They are built not from calorimeter clusters but from tracks in the inner detector using the anti-k_T algorithm with $R = 0.2$. Track jets are required to have a $p_T > 10$ GeV and $|\eta| < 2.5$. For a full description of these different jet types refer back to chapter 4.

6.1.5 MET

E_T^{miss} is reconstructed as a negative vector sum of the p_T of electrons, muons, small R jets and inner detector tracks not associated with any of these objects but originating from the primary vertex. Small radius jets are used because they are calibrated down to a lower p_T and over a wider η range. [18]

6.2 Event Selection

As this analysis is targeting high mass resonances, the Higgs is expected to be highly boosted such that its decay products are contained in a single large-R jet. Events that fall into any of the three lepton categories are thus required to have at least one large-R jet with $p_T > 250$ GeV and $|\eta| < 2.0$ with the highest p_T jet selected to be the Higgs candidate. A Higgs mass requirement of 75 GeV $< m_{jet} <$ 145GeV is applied to events. Track jets are matched to the large-R jets using ghost association and a requirement is applied that at least one of the track jets matched to the leading large-R jet must be b-tagged. The b-tagging algorithm used is the MV2c20 algorithm with a 70% efficiency working point. Events are further divided into two samples with 1 b-tagged track jet or 2 b-tagged track jets associated to the leading large-R jet. These selection criteria help to reject the two leading backgrounds, W+Jets and $t\bar{t}$. Events with extra b-tagged track jets not associated with the leading large-R jet are used in control regions for these backgrounds. The selection criteria for all three lepton channels is summarised in Table 6.1

6.2.1 Zero lepton Channel

For 0-lepton events an E_T^{miss} trigger with a threshold of 80 GeV is used to record events and there must be exactly no leptons passing the "loose" criteria. The discriminating variable used to define the sensitivity is the transverse mass of the VH system as defined as:

$$m_{T,VH} = \sqrt{(E_T^{Jet} + E_T^{miss})^2 - (\overrightarrow{p_T}^{Jet} + \overrightarrow{E_T}^{miss})^2}. \quad (6.1)$$

To reduce the multijet background a variety of cuts are applied to the events that satisfy our trigger and object requirements. $E_T^{miss} > 200$ GeV is required and the missing transverse momentum (p_T^{miss}) is required to be greater than 30 GeV. Three cuts are applied on the angles between different objects in the event, $\Delta\phi(E_T^{miss}, p_T^{miss}) < 90$, $\Delta\phi(E_T^{miss}, large\ R\ jet) < 120$, and minimum $\Delta\phi(E_T^{miss}, small\ R\ jet) < 20$. In the case of the small-R jets they are required to pass a pre-selection in order to be used in the analysis cuts. Jets with $|\eta| < 2.5$ must have $p_T > 20$ GeV and jets with $2.5 < |\eta| < 4.5$ must have $p_T > 30$ GeV. The effect of these angular selection criteria on the multijet background can be seen in Figure 6.1 and Figure 6.2. Any event which has an extra b-tagged track jet that is not associated with the leading large-R jet is rejected to reduce the $t\bar{t}$ background.

6.2.2 One lepton Channel

For the 1-lepton category the unprescaled single lepton trigger is used with a minimum p_T requirement of 24 GeV for isolated electrons and 20 GeV for isolated muons. If the object that fired the trigger does not match the object reconstructed by the offline software then the event is not used. Exactly one lepton with

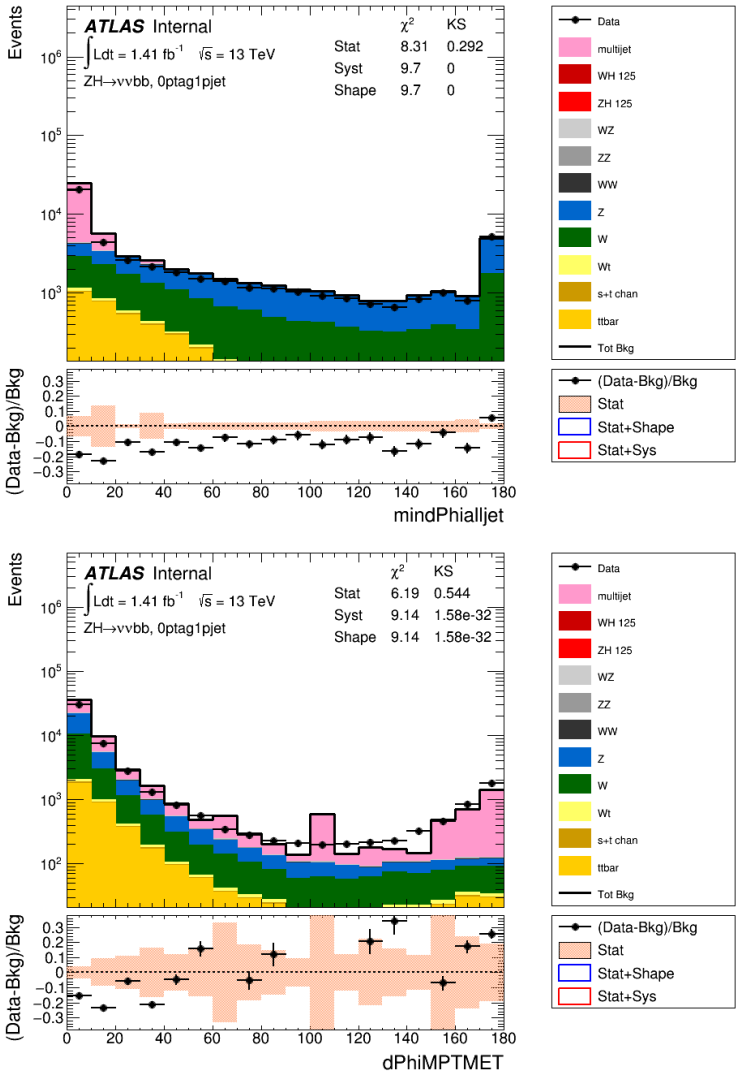

Figure 6.1: Minimal azimuthal separation between E_T^{miss} and any of the small-R jets (left) and the azimuthal separation between E_T^{miss} and p_T^{miss} (right).

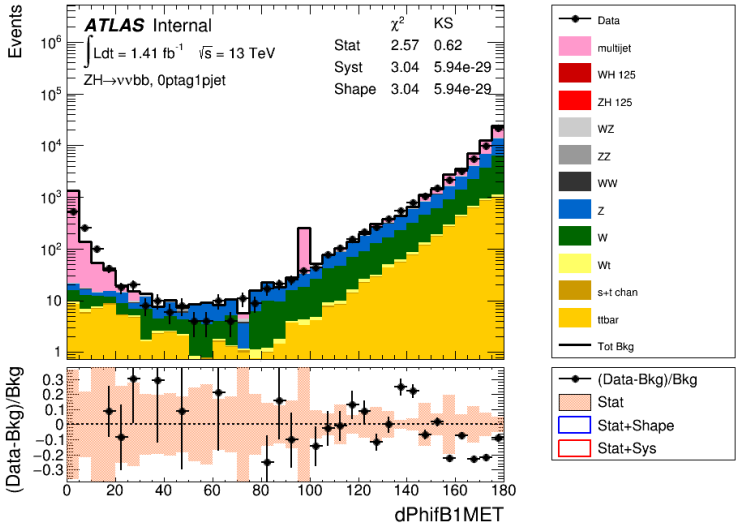

Figure 6.2: Minimal azimuthal separation between E_T^{miss} and the leading large-R jet.

$p_T > 25\,\text{GeV}$ is required. In order to reject the multijet background the lepton must also pass the "tight" identification category, E_T^{miss} must be greater than 100 GeV and cuts are applied to the calorimeter and track isolation. To reject $t\bar{t}$ events the same veto on extra b-tagged track jets is applied to the 1-lepton selection as is used in the 0-lepton case.

The mass of the VH system is used as the discriminating variable in the 1-lepton channel. The p_Z of the neutrino is calculated by applying the W mass constraint to the electron and neutrino and solving the resulting quadratic equation. The smallest real-valued solution is used.

6.2.3 Two lepton Channel

The 2-lepton channel uses a logical OR between three triggers for electrons and two for muons. The electron triggers are HLT_e24_lhmedium_iloose which requires a medium electron passing loose isolation requirements with $p_T > 24\,\text{GeV}$, HLT_e60_lhmedium1 which requires a medium electron with $p_T > 60\,\text{GeV}$, and

HLT_e120_lhloose which requires a loose electron with $p_T > 120\,\text{GeV}$. The muon triggers are HLT_mu20_iloose_L1MU15 which requires a muon passing loose isolation criteria with $p_T > 20\,\text{GeV}$, and HLT_mu50 which requires a muon with $p_T > 50\,\text{GeV}$.

The offline selection requires exactly 2 leptons which pass the loose criteria and have $p_T > 25\,\text{GeV}$. At least one of the leptons must pass the "medium" criteria and have $p_T > 60\,\text{GeV}$. Muons are also required to be well isolated in both the calorimeter and the inner detector. A mass requirement is applied to the invariant mass of the dilepton system, m_{ll}. For electrons it is $70 < m_{ll} < 110\,\text{GeV}$ and for muons it is $55 < m_{ll} < 125\,\text{GeV}$. The wider window in the muon case is to account for the worse p_T resolution for high p_T muons. A scale factor of $\frac{m_Z}{m_{\mu\mu}}$ is also applied to the four-momentum of the dimuon system to help correct for this. Unlike the 0-and 1-lepton channel, no veto is applied to events with extra b-tags.

	0 lepton	1 lepton	2 lepton
p_T^{jet}	> 250 GeV		
N_{jet}	$>= 1$		
m_{jet}	75 GeV $< m_{jet} <$ 145 GeV		
n_{b-tag}	$>= 1$		
$\lvert\eta^{jet}\rvert$	< 2.0		
p_T^{lep} leading	-	>25 GeV	>60 GeV
p_T^{lep} sub-leading	-	-	>25 GeV
E_T^{miss}	>200 GeV	>100 GeV	-
m_{ee}	-	-	70 GeV $< m_{ee} <$ 110 GeV
$m_{\mu\mu}$	-	-	55 GeV $< m_{\mu\mu} <$ 125 GeV
$\Delta\phi(E_T^{miss}, p_T^{miss})$	$< \frac{\pi}{2}$	-	-
$\Delta\phi(E_T^{miss}, large\ R\ jet)$	$< \frac{2\pi}{3}$	-	-
$\Delta\phi(E_T^{miss}, small\ R\ jet)$	$< \frac{\pi}{9}$	-	-

Table 6.1: Summary of the signal region event selection for each lepton channel.

6.3 1 Lepton Cut Optimisation Studies

At the increased centre of mass energy in Run 2, $t\bar{t}$ production increases by a factor of $\sim$4 over the Run 1 cross-section [72]. To combat this, studies were performed to find variables that can separate between the VH signal and $t\bar{t}$ so that by cutting on these variables the sensitivity of the analysis will improve.

6.3.1 Possible Variables

Many variables of possible interest were identified, mostly based on the topology of $t\bar{t}$ decays; there tends to be a momentum imbalance because the extra jets or leptons in the $t\bar{t}$ final state are not used. A selection of these variables is shown in Figure 6.3; these distributions show a clear shape difference between the backgrounds and the signal.

6.3.2 Optimisation

To exploit this shape difference a value on which to cut must be chosen. The simplest way to choose this value is to use an optimisation program such as TMVA [73]. This program chooses a desired signal efficiency and tries to find an upper and lower value to apply to a variable that matches that efficiency while giving the maximum background rejection. TMVA is capable of performing this optimisation on more than one variable simultaneously to produce a rectangular selection. It can also perform the calculation for multiple signal efficiency points.

Figure 6.4 shows this optimisation performed on each of three variables in conjunction with the mass of the large-R jet. It is clear from this plots that the best performing variable is the ratio of the p_T of the VH system to the scalar sum of the p_T of the decay of the VH system.

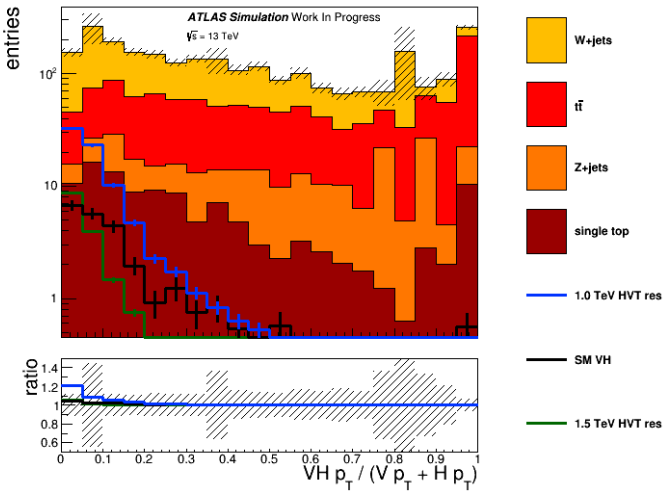

(a) Ratio of the momentum of the VH system to the scalar sum of the vector boson and large-R-jet momentum

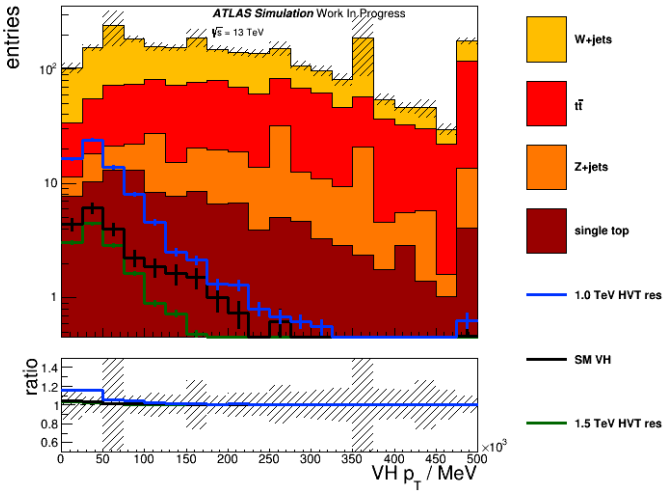

(b) Momentum of the VH system

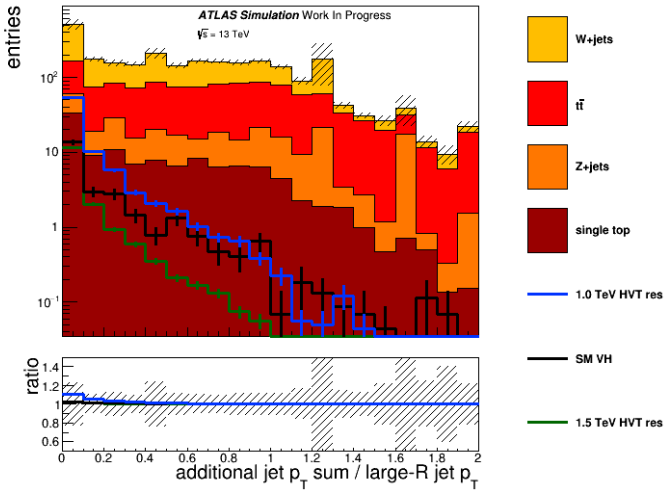

(c) Sum of the momentum of all other jets in the event relative to the momentum of the large-R jet

Figure 6.3: Three variables of interest for reducing the contribution of $t\bar{t}$ to the signal region selection

The variable used to set limits in the 1 lepton channel is the mass of the VH system. The effect of applying the cut values that correspond to 50% and 90% signal efficiency compared to the basic event selection can be seen in Figure 6.5. These cuts were not used in the final analysis selection as they had not been fully validated when the selection was frozen, however a mass window in the large-R jet was applied.

6.4 Control Regions and Background Estimation

In order to validate the modelling of the various background processes in this analysis a variety of control regions were defined in which a relatively pure sample of the background being validated could be obtained. These regions were then

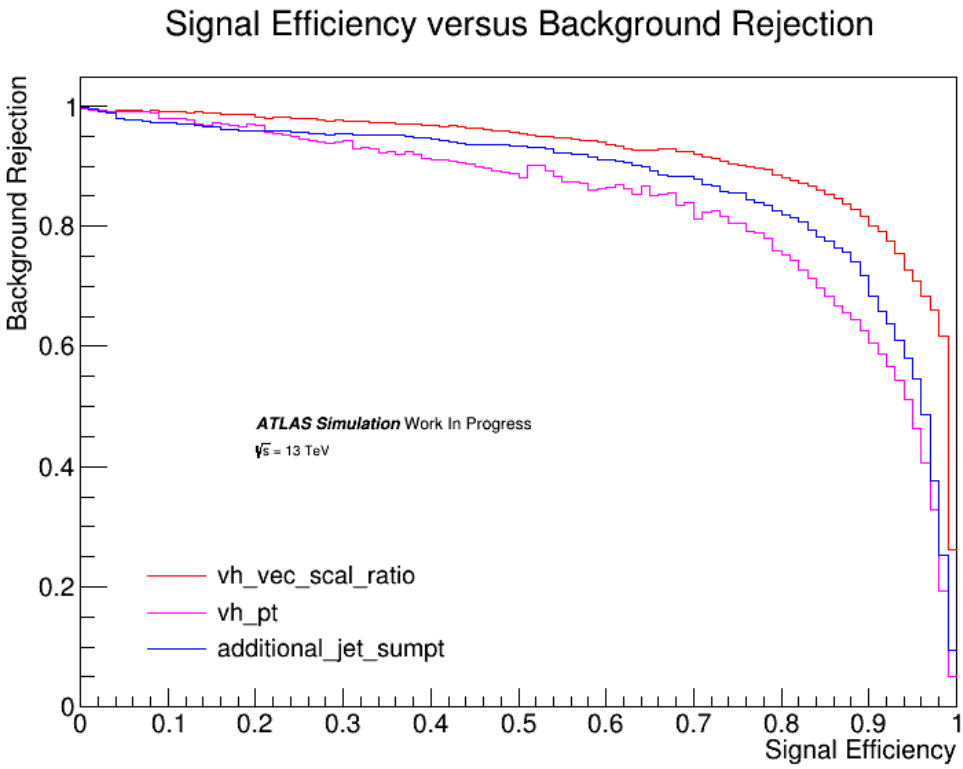

Figure 6.4: Maximised background rejection for a given signal efficiency point for the three variables shown in Figure 6.3. vh_vec_scal_ratio is for the variable shown in Figure 6.3a, vh_pt for Figure 6.3b, and additional_jet_sumpt for Figure 6.3c.

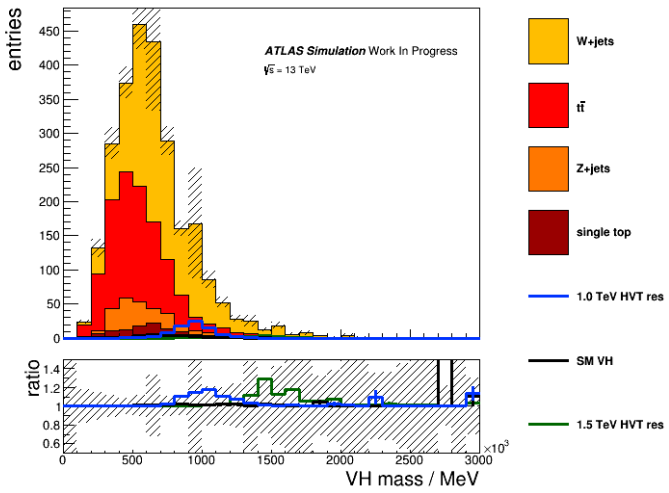

(a) Nominal Cuts Only

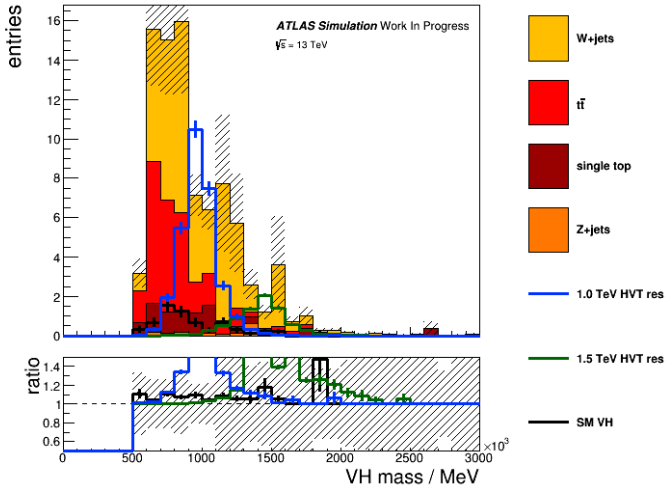

(b) jet mass > 85 GeV and ratio < 0.05 (50% signal efficiency)

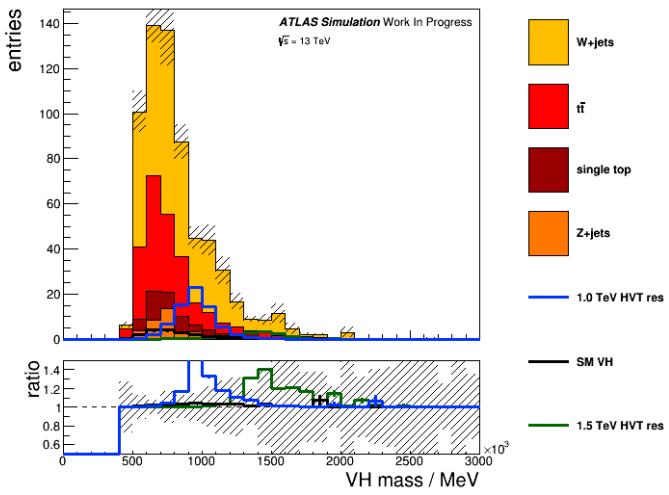

(c) jet mass > 25 GeV and ratio < 0.2 (90% signal efficiency)

Figure 6.5: VH mass distributions showing the effect of additional cuts.

used to compare the modelling of that background to data. A control region is usually defined by modifying some of the analysis cuts so that signal events are no longer selected. Different backgrounds are dominant in each lepton channel, however the single top and diboson backgrounds are extremely small in all channels and multijet is largely eliminated by applying selection criteria to the E_T^{miss} as shown in subsection 6.4.4.

The control regions for each background are used in the limit setting procedure. This helps to both constrain the contribution of the background processes in the signal region which should help improve the final sensitivity and improve the modelling of these backgrounds in the final plots. A diagram of the signal and control regions can be found in Figure 6.6 and a description for each channel is below.

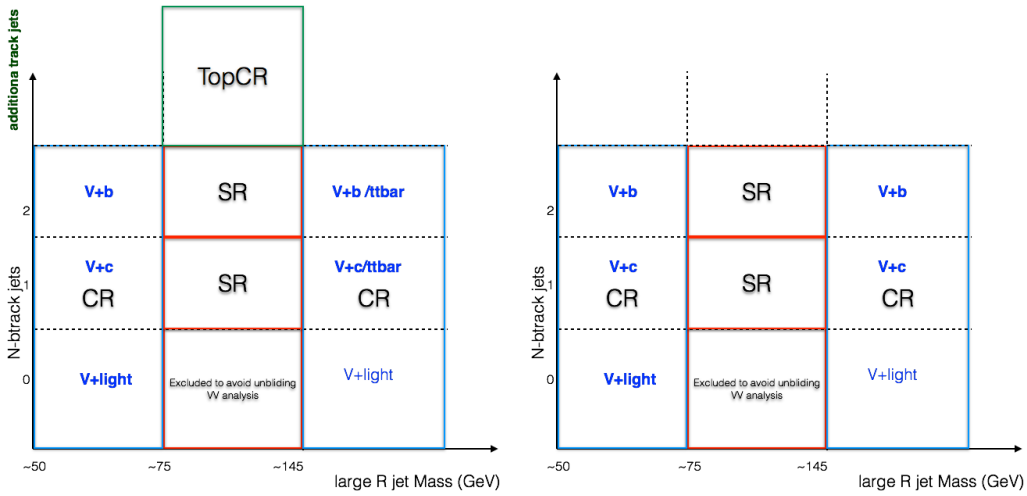

(a) Schematic of the signal region and control region used for the 1-lepton and 0-lepton channels.

(b) Schematic of the signal region and control region used for the 2-lepton channel.

Figure 6.6: Schematic of the signal region and control regions.

6.4.1 Zero lepton Channel

In the 0-lepton channel the dominant backgrounds are W/Z+jets and $t\bar{t}$. A number of control regions are defined in this channel to validate the modelling of these backgrounds. These control regions are based on the number of b-tags associated to the large-R jet, the number of additional b-tagged jets not associated to the large-R jet and the mass of the large-R jet.

For the $t\bar{t}$ background, four control regions are defined. The first requires that events have at least one b-tag and at least one extra b-tag and a jet mass between 75 and 145 GeV. The second requires 1 b-tag, 1 additional b-tag and the jet mass to be greater than 145 GeV; this is referred to as the high-mass sideband. The third is also a high-mass sideband with 1 b-tag and 0 additional b-tags and the fourth is the high-mass sideband with 2 b-tags and 0 additional b-tags.

There are two control regions used to validate the W/Z+jets background. They are both low mass sidebands, $m_{jet} < 75$ GeV, with one requiring one b-tag

and the other requiring two b-tags both with 0 additional b-tags. The former validates the modelling of the W/Z+c composition of the W/Z+jets background and the latter the W/Z+b composition.

Another low mass control region with 1 tag and 1 additional tag is also defined, this region contains a mixture of both dominant backgrounds and helps constrain both. The last control region requires 1 b-tag and the mass of the large-R jet is required to be in the signal window $75 < m_{jet} < 145\,\text{GeV}$. This control region also contains both W+jets and $t\bar{t}$ events and is useful in the limit setting procedure for understanding b-tagging because it will contain some events with 2 b-jets one of which was rejected by the b-tagging algorithm.

The data-MC comparison for each of these regions is shown in Figure 6.7 and the backgrounds are seen to be well modelled. In the final analysis the 2-tag, 0 additional tag high and low mass sidebands had to be merged due to statistical limitations.

6.4.2 One lepton Channel

In the 1 lepton channel the dominant backgrounds are W+jets and $t\bar{t}$ and the control regions are the same as in the 0 lepton channel but the low mass sideband is defined as $m_{jet} < 65$ GeV, and due to statistics the low and high mass sidebands have been merged in both the 1 tag 0 additional tags, and 2 tag 0 additional tag cases. The modelling is shown in Figure 6.8 and the data-MC agreement is good in all control regions.

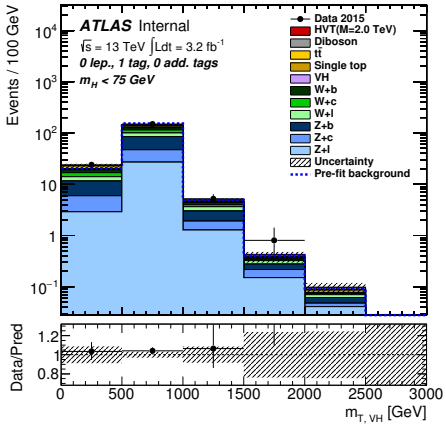

(a) 1 tag low mass sideband

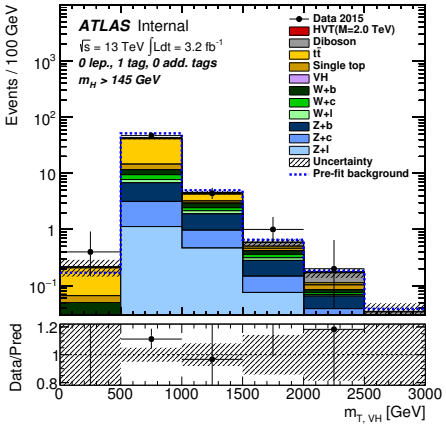

(b) 1 tag high mass sideband

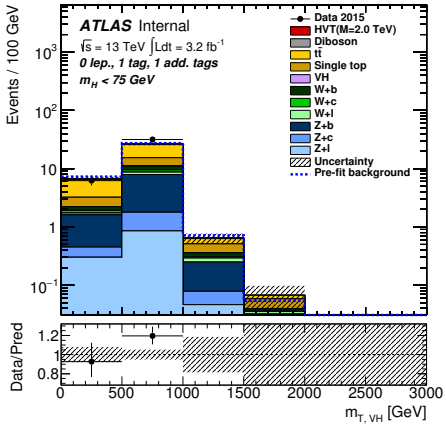

(c) 1 additional tag, low mass region

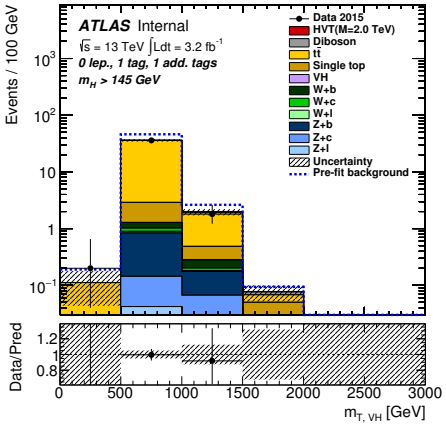

(d) 1 additional tag, high mass region

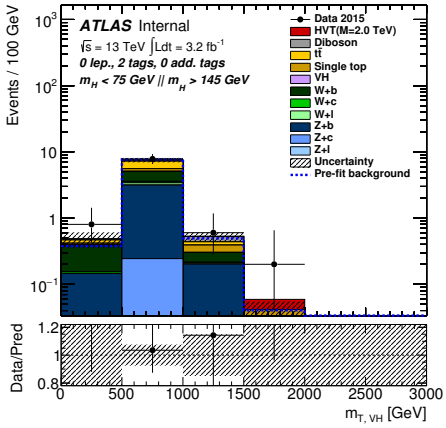

(e) 2 tag, merged

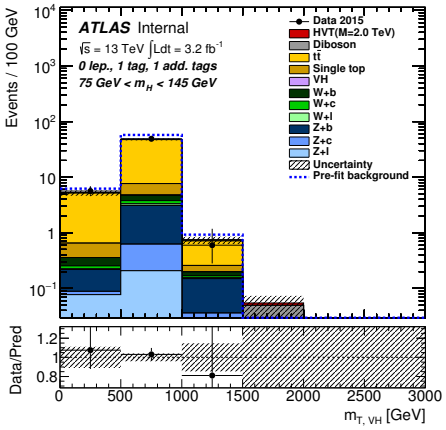

(f) 1 additional tag region

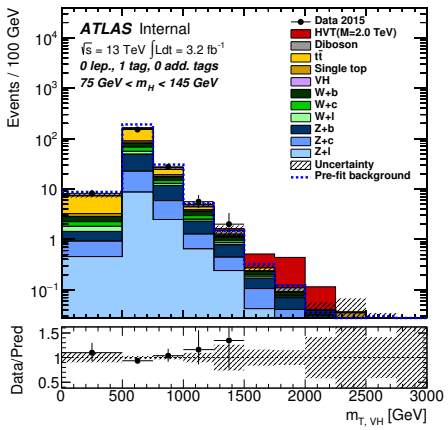

(g) 1 tag region

Figure 6.7: Postfit plots of the control regions used in the 0 lepton analysis, the blue band represents the prefit MC prediction. Low mass is defined as $m_H <$ 75 GeV, high mass as $m_H >$ 145 GeV and merged is the combination of these two regions where statistics are limited.

6.4.3 Two lepton Channel

In the 2 lepton channel the dominant background is Z+jets and for this background the same control regions as the 0 lepton channel are used but without any requirement on additional b-tagged jets. The mass sideband definition is also the same. Control regions are also defined to control the subdominant $t\bar{t}$ background in this channel. The high and low mass sideband definitions from the 0 lepton channel are used but are merged in both the 1 and 2 tag cases dues to statistical limitations. A region in which the leptons selected are one electron and one muon is defined for both 1-tag and 2-tag regions. There is also a 1-tag region with a mass window of $75 < m_{jet} < 145\,\text{GeV}$, as is used in the 0 lepton channel The data-MC comparison in these regions are shown in Figure 6.9 and the modelling is good.

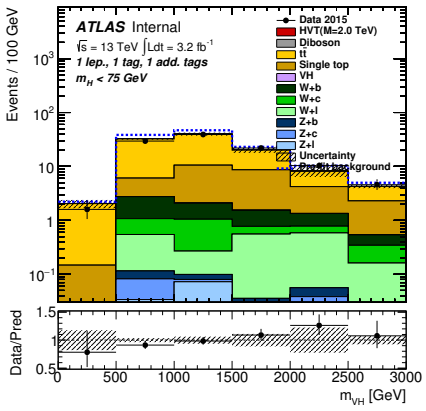

(a) 1 additional tag, low mass region

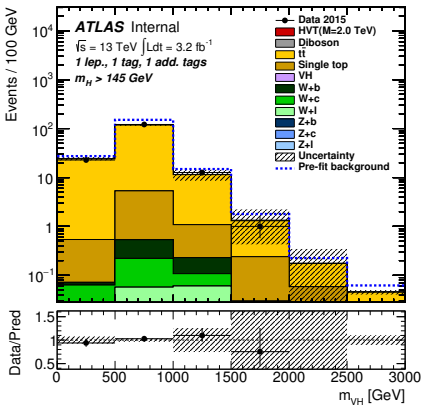

(b) 1 additional tag, high mass region

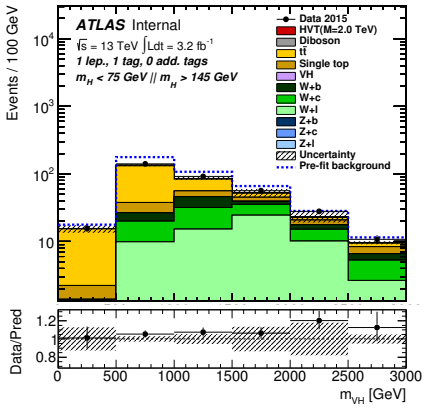

(c) 1 tag, merged region

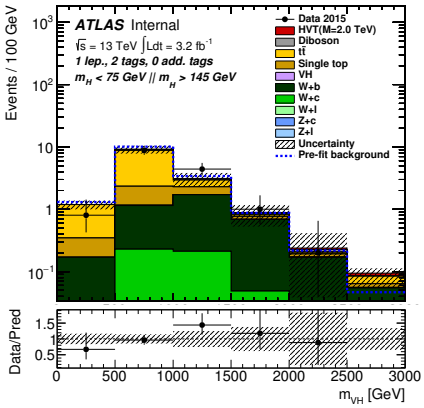

(d) 2 tag, merged region

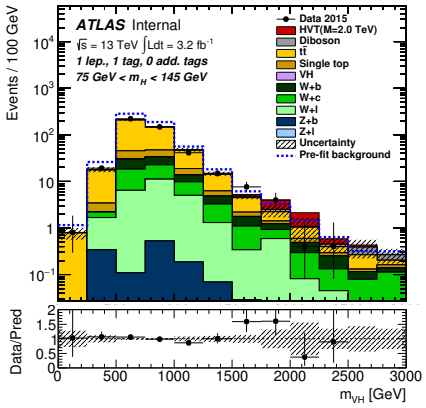

(e) 1 tag region

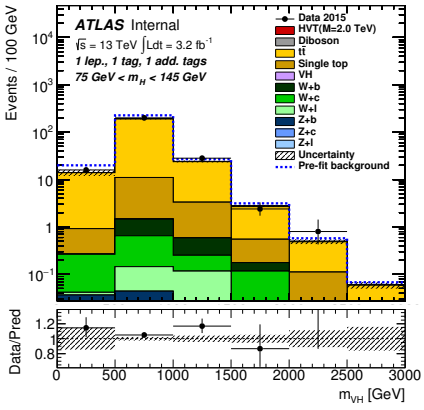

(f) 1 additional tag, central mass region

Figure 6.8: Postfit plots of the control regions used in the 1 lepton analysis, the blue band represents the prefit MC prediction. Low mass is defined as $m_H < 75$ GeV, high mass as $m_H > 145$ GeV and merged is the combination of these two regions where statistics are limited.

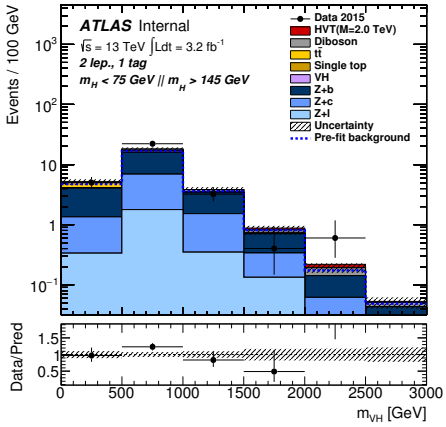

(a) 1 tag, merged region

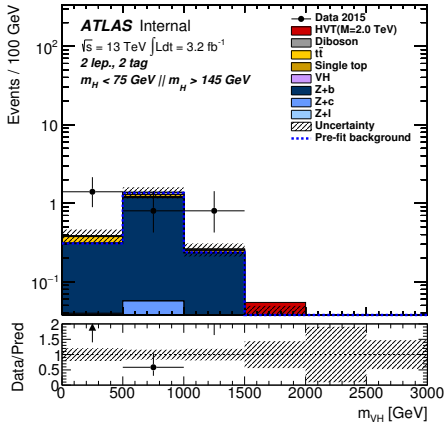

(b) 2 tag, merged region

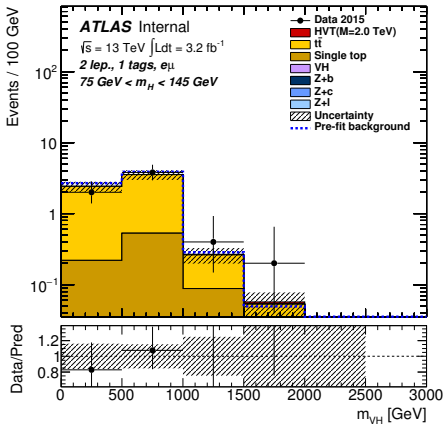

(c) 1 tag eμ region

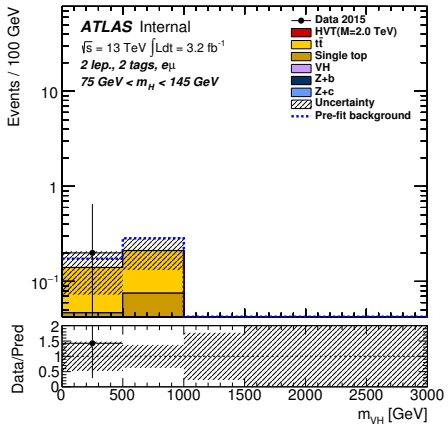

(d) 2 tag eμ region

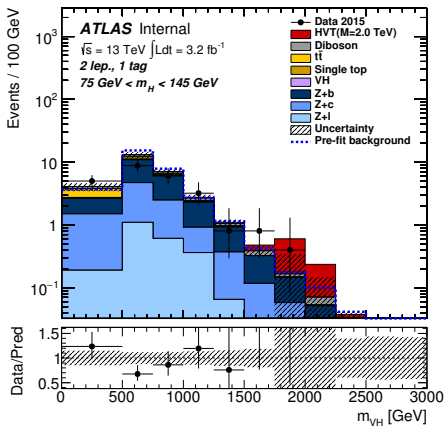

(e) 1 tag central mass region

Figure 6.9: Postfit plots of the control regions used in the 2 lepton analysis, the blue band represents the prefit MC prediction. Low mass is defined as $m_H <$ 75 GeV, high mass as $m_H >$ 145 GeV and merged is the combination of these two regions where statistics are limited.

6.4.4 Multijet background

In this analysis one of the backgrounds that has been mentioned is the multijet/QCD background. This consists of events in which jets were misidentified as leptons or when leptons are produced from hadron decays (non-prompt leptons). It was proposed that a high MET cut could eliminate this background almost entirely from the analysis.

Modelling the multijet background is challenging because generating enough Monte Carlo statistics to reasonably model the background takes a prohibitive amount of time. Instead of using a Monte Carlo technique to estimate this background a data-driven technique can be used. To do this the data and Monte Carlo that pass the event selection is used but also another sample is generated by changing the isolation requirements applied to the data so that the sample will be dominated by multijet. This new sample and the other MC backgrounds are used to perform a fit to the "normal" data. In this case the histogram used to perform this fit is the M_W^T and the normalisation of the multijet sample and the V+Jets sample are the parameters that are allowed to change in order to fit the backgrounds to the data.

In Figure 6.10a the results of this fit is shown for the event selection with no E_T^{miss} cut and shows a contribution from multijet. The results of the same fit when a E_T^{miss} cuts of 100 GeV is added to the selection is shown in Figure 6.10b and the multijet contribution is gone. Based on these studies a cut on E_T^{miss} is applied that removes multijet as a background in this analysis.

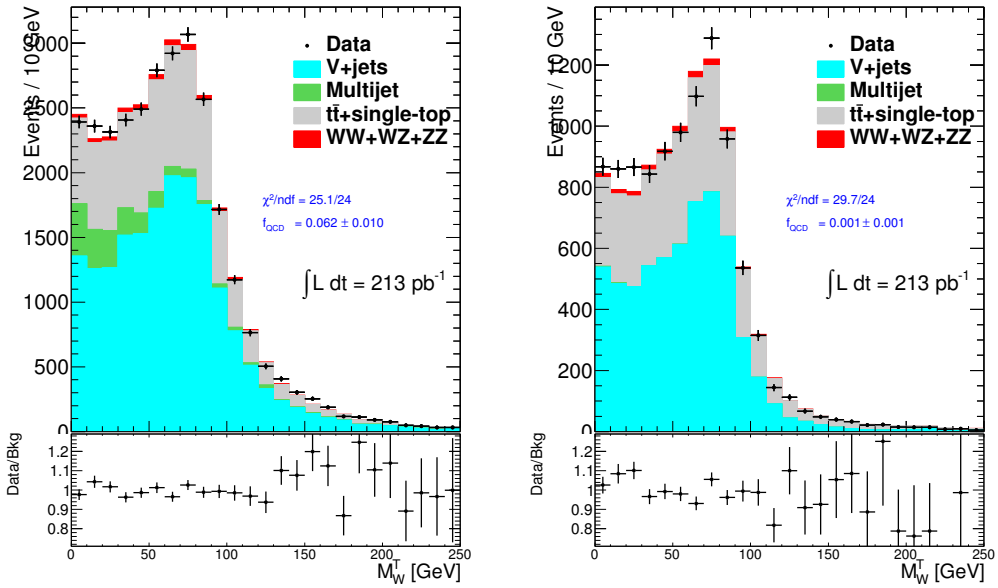

(a) MJ fit result with nominal selection only

(b) MJ fit result with Nominal selection and MET > 100 GeV

Figure 6.10: Comparison of the multijet fit results with and without an $E_T^{miss} >$ 100 GeV cut designed to remove the multijet background.

6.5 Uncertainties

Systematic uncertainties in this analysis come from theoretical uncertainties on the signal models, background modelling uncertainties and those from the reconstruction and identification of physics objects, efficiency measurements and corrections to particle energy measurements. An uncertainty on the luminosity is also calculated.

This section describes the calculation of theory and measurement uncertainties applied to the VH resonances analysis. A summary of all uncertainties can be found in Table 6.2.

6.5.1 Detector Uncertainties

There are a variety of uncertainties relating to object reconstruction in the ATLAS detector that need to be taken into account when performing an analysis, for example there is an uncertainty due to the efficiency of electron reconstruction that has to be taken into account. The most significant uncertainties in this analysis are those from the scale and resolution calibrations applied to the large-R jet energy and mass. These are estimated by comparing measured values in the calorimeter to those in the tracker using a sample of dijet events in data and Monte Carlo [74]. The second significant uncertainty comes from the b-tagging efficiency for track jets which is derived from $t\bar{t}$ events [75]. Other uncertainties that were found to have an impact come from lepton efficiencies as mentioned before, lepton momentum and energy measurements, trigger efficiencies and the small-R jet calibrations [53].

6.5.2 Background Modelling Uncertainties

Uncertainties designed to account for imperfections in simulation are applied to the simulated backgrounds relevant in this analysis. Normalisation uncertainties for each background are taken from cross-section measurements performed at the LHC or Tevatron. For W/Z+light jets a value of 10% is used, for W/Z+b and W/Z+c 30% is used [76]. In the case of t$\bar{\text{t}}$ and single top an uncertainty of 30% is used [77]; for dibosons it is 11% [70].

Uncertainties on the shape of m_{VH} for the W/Z+Jets and $t\bar{t}$ backgrounds are also estimated by comparing predictions from different generators. For W/Z+Jets the nominal Sherpa sample is compared to one produced using MadGraph. In the case of $t\bar{t}$, Powheg is compared with aMC@NLO. For $t\bar{t}$ two more uncertainties

are included. One is calculated by taking the difference from the nominal $t\bar{t}$ to a sample in which the factorisation and renormalisation scale is doubled and one in which it is halved. The second systematic is a shape systematic derived from the comparison of the Pythia generator to Herwig which is necessary to account for the uncertainty in the showering step of the Monte Carlo simulation.

An uncertainty on the luminosity of 5% is also included along with uncertainties on the statistics of the Monte Carlo samples.

6.6 Limit Setting Procedure

In searches for new physics a threshold above which we can claim a discovery must be defined. This is done using confidence intervals that calculate how well an observation matches our currently accepted physical model (called the background only hypothesis) and how well it matches the theory that is being tested, called the signal+background hypothesis. Limits are often described, as is the case here, by the production cross-section at which we can reasonably exclude the possibility of the existence of a particular process.

This section describes the procedure used to calculate these limits, a modified frequentist method known as the asymptotic CL_s method.

6.6.1 Statistical Hypothesis Testing

When calculating the confidence intervals for this analysis the profile likelihood function was used, defined as:

$$L(\mu, \boldsymbol{\theta}) = \prod_{j=1}^{N} \frac{(\mu s_j + b_j)^{n_j}}{n_j!} e^{-(\mu s_j + b_j)} \,, \tag{6.2}$$

where μ is the signal strength, $\boldsymbol{\theta}$ denotes all nuisance parameters, s_j is the number of predicted signal events in a particular bin, b_j is the predicted number of background events in a particular bin, and n_j is the total number of data events in a bin. One may also define control regions that help constrain nuisance parameters in the fit. These are included in the fit as in the same way as our signal region, as extra bins in the likelihood calculation. In order to test a hypothesis of a particular signal strength, μ, a profile likelihood ratio is constrained:

$$\lambda(\mu) = \frac{L(\mu, \hat{\hat{\boldsymbol{\theta}}})}{L(\hat{\mu}, \hat{\boldsymbol{\theta}})} \tag{6.3}$$

$\hat{\hat{\boldsymbol{\theta}}}$ is the conditional maximum likelihood (ML) estimator, the value of $\boldsymbol{\theta}$ that maximises L for a specific μ. The term on the denominator is the unconditional maximised likelihood estimator. This means that the values of μ and θ are chosen as those that maximise L (or in other words $\hat{\mu}$ and $\hat{\boldsymbol{\theta}}$ are their ML estimators).

The actual test statistic used to define our confidence intervals in this case is the profile log likelihood:

$$t_\mu = -2 \ln \lambda(\mu) \tag{6.4}$$

$\lambda(\mu)$ has a range between zero and one, with one denoting a high probability that the data matches the hypothesis for that μ. Higher values of t_μ can be interpreted similarly.

To calculate a p-value or a confidence interval from a test statistic we must first generate a pdf of our test statistic for a chosen value of μ, $f(t_\mu|\mu)$, and the p-value can be calculated as:

$$p_\mu = \int_{t_{\mu,obs}}^{\infty} f(t_\mu|\mu) dt_\mu \tag{6.5}$$

For a search, as is the case in this analysis, $\mu = 0$ is used.

In order to generate the pdf of a test statistic the profile likelihood ratio can be estimated as

$$-2\ln\lambda(\mu) = \frac{(\mu-\hat{\mu})^2}{\sigma^2} + \mathcal{O}(\frac{1}{\sqrt{N}}) \tag{6.6}$$

where $\hat{\mu}$ follows a Gaussian distribution with standard deviation σ and mean μ'. Using this value for t_μ its pdf can be derived as:

$$f(t_\mu|\mu') = \frac{1}{2\sqrt{t_\mu}}\frac{1}{\sqrt{2\pi}}\left[\exp\left(-\frac{1}{2}\Big(\sqrt{t_\mu}+\frac{\mu-\mu'}{\sigma}\Big)^2\right)+\exp\left(-\frac{1}{2}\Big(\sqrt{t_\mu}-\frac{\mu-\mu'}{\sigma}\Big)^2\right)\right] \tag{6.7}$$

Now that an expression for the pdf of the test statistic for a particular μ has been derived, it is possible to calculate a p-value. The result can also be expressed in terms of significance as:

$$Z = \Phi^{-1}(1-p_\mu) \tag{6.8}$$

where Φ is the quantile (inverse of the cumulative distribution) [78].

6.6.2 Constraining Nuisance Parameters

In subsection 6.6.1 the setting of limits is discussed and how control regions can be included as additional bins in the likelihood calculation that help to constrain the limit. However, the description of how systematic uncertainties are included as nuisance parameters is neglected in that description.

In order to include systematic uncertainties in the limit setting procedure two approaches are used. One is for a type of systematic that only affects the normalisation of the overall number of estimated events, the other describes the inclusion of systematics that effect the shape of distributions. Both of these systematic types are incorporated into the limit setting procedure in the same

way but using different interpolation strategies.

Normalisation uncertainties are included by adding a term to the likelihood that affects the total number of predicted events. This is a Gaussian function that depends on the uncertainty. For a simple likelihood described by the product of Poisson probabilities, $\mathcal{P}(n_i|\mu_i)$, where n_i is the number of events and μ_i is the number of predicted events the modified likelihood that includes the systematic is described in Equation 6.9.

$$L = \prod_{i=1}^{N} \mathcal{P}(n_i|\mu_i)\mathcal{G}(L|\widetilde{L}, \sigma_L) \tag{6.9}$$

This new term is a function, usually a Gaussian, of mean $\widetilde{L}$ and width σ_L which constrains the value of the nuisance parameter, L, to its final value. The mean of the Gaussian is set to be the nominal value of the systematics and the ± 1 values are set to be the up and down values. This function is used to interpolate and calculate the best fit value for the systematic during the fitting [79].

Shape uncertainties are included in the fit by providing an "up" and "down" histogram for each uncertainty that is calculated by varying a parameter by $\pm$ 1 sigma for that systematic. The final histogram is calculated as

$$\begin{aligned} h &= h_0 + \alpha(h_+ - h_0) \qquad \alpha > 0 \\ h &= h_0 - \alpha(h_- - h_0) \qquad \alpha \geq 0 \end{aligned} \tag{6.10}$$

where h is the postfit histogram, h_0 is the nominal histogram, h_+ the up variation and h_- the down variation. α is known as the nuisance parameter for this uncertainty and is a Gaussian with a mean of 0 and width of 1 that is allowed to float during the fit which changes the shape of distributions due to that systematic.

6.7 Results

The reconstructed mass distributions for the signal region in all three channels are shown in Figure 6.11 and the yields for each process in all three channels are show in Table 6.3, Table 6.4, and Table 6.5. Additional plots can be found in Appendix B.

The results of the likelihood fits performed, using the method described in section 6.6 and including the control regions described in section 6.4 and the nuisance parameters described in section 6.5 as constraints, are shown in Figure 6.12. The limits are set independently for each channel and are shown with two HVT model predictions for comparison with resonance couplings g_v=1 and g_v=3. The limits exclude the observation of a resonance with coupling g_v=1 with mass $m_{V'} < 1450$ GeV in the 0 lepton channel, $m_{V'} < 1520$ GeV in the 1 lepton channel and $m_{V'} < 980$ GeV in the 2 lepton channel. For a coupling g_v=3 the excluded mass range is $m_{V'} < 1760$ GeV in the 0 lepton channel, $m_{V'} < 1620$ GeV in the 1 lepton channel and $m_{V'} < 1400$ GeV in the 2 lepton channel.

The final values for the systematics are shown in Figure 6.13, Figure 6.14, and Figure 6.15 for the 0, 1 and 2 lepton channels respectively. The value of the systematic, sometimes called a pull, corresponds to how far from the prefit nominal value the final (best fit) value of a particular systematic has moved. The bars represent the uncertainty on the best fit value of a systematic. In each channel no systematic has moved more than 1 standard deviation from its prefit value which suggests that the estimation of the systematics is very conservative. Many systematics have a post fit uncertainty that is smaller than 1 sigma which suggests that the fitting procedure is constraining those systematics.

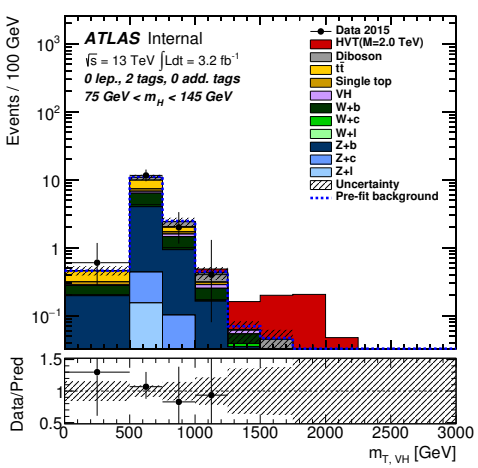

(a) 0 lepton

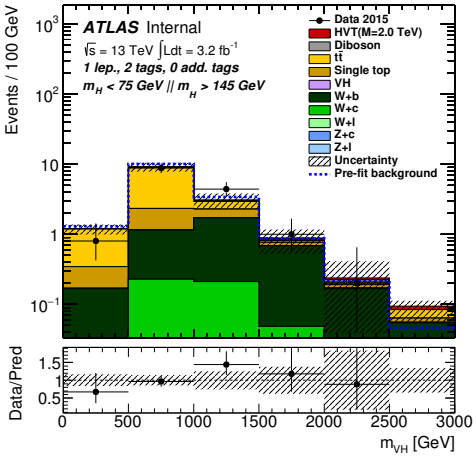

(b) 1 lepton

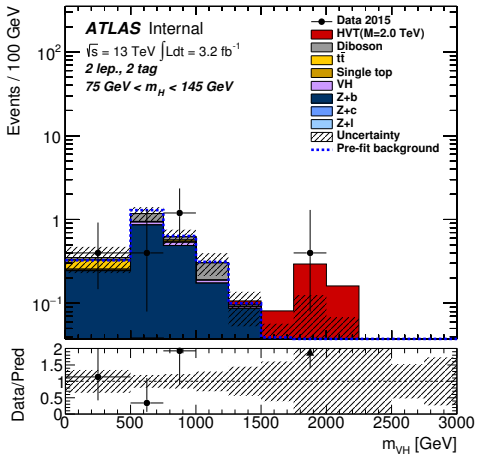

(c) 2 lepton

Figure 6.11: Postfit plots of the signal regions used to set limits. The blue band represents the prefit MC prediction, the signal is normalised to the 95% CL upper limit. More postfit plots can be found in Appendix B

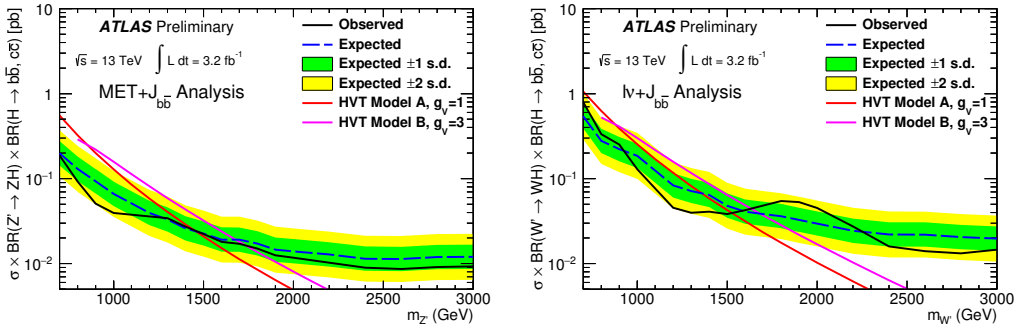

(a) 0 lepton (b) 1 lepton

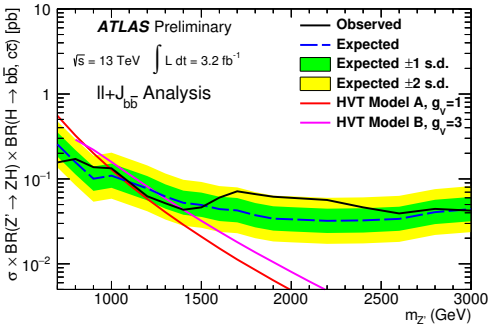

(c) 2 lepton

Figure 6.12: Upper limits at the 95% CL for the production cross section of a high mass resonance (Z'/W') times its branching ratio to ZH/WH

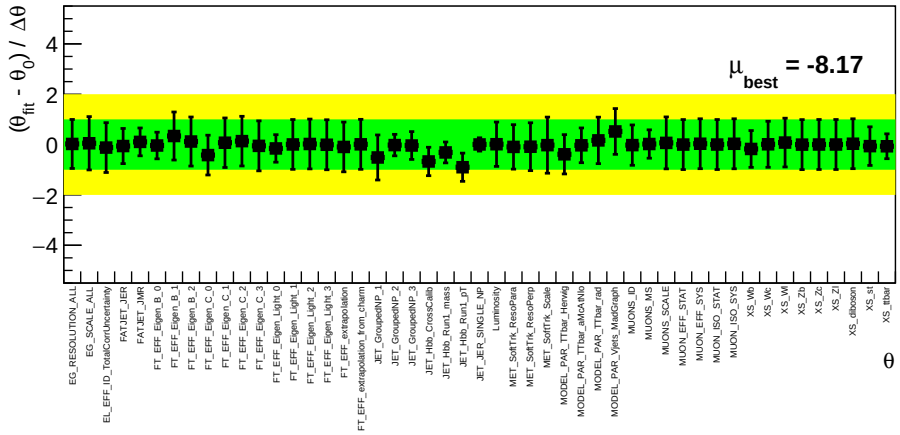

Figure 6.13: Post-fit values of nuisance parameters for the 1 lepton channel. The shaded bands correspond to the prefit uncertainty size and the error bands on the points correspond to the postfit uncertainty size.

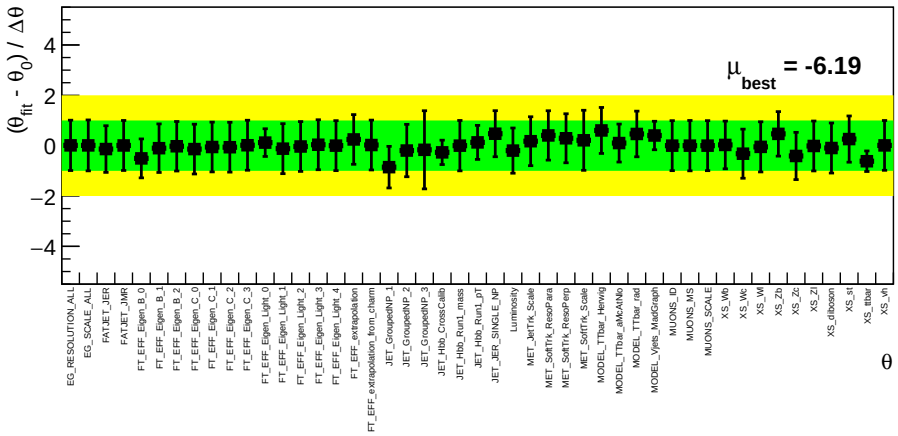

Figure 6.14: Post-fit values of nuisance parameters for the 0 lepton channel. The shaded bands correspond to the prefit uncertainty size and the error bands on the points correspond to the postfit uncertainty size.

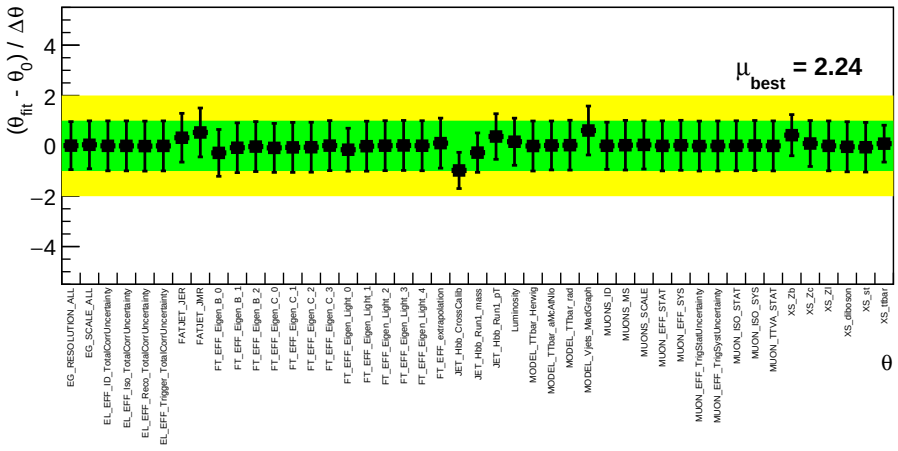

Figure 6.15: Post-fit values of nuisance parameters for the 2 lepton channel. The shaded bands correspond to the prefit uncertainty size and the error bands on the points correspond to the postfit uncertainty size.

Source	Description	Analysis Name
Electron Trigger	Efficiency SF	EL_EFF_Trigger_TotalCorrUncertainty
Electrons	Energy scale	SysEG_SCALE_ALL
Electrons	Energy resolution	SysEG_RESOLUTION_ALL
Electrons	ID efficiency SF	SysEL_EFF_ID_TotalCorrUncertainty
Muon Trigger	Efficiency SF	MUON_EFF_TrigSystUncertainty
Muons	p_T resolution MS	SysMUONS_MS
Muons	p_T resolution ID	SysMUONS_ID
Muons	p_T scale	SysMUONS_SCALE
Muons	Isolation efficiency SF	SysMUON_ISO_SYS
Muons	Isolation efficiency SF	SysMUON_ISO_STAT
Muons	Identification efficiency SF	SysMUON_EFF_SYS
Muons	Identification efficiency SF	SysMUON_EFF_STAT
MET	Soft term	SysMET_SoftTrk_ResoPerp
MET	Soft term	SysMET_SoftTrk_ResoPara
MET	Soft term	SysMET_SoftTrk_ScaleUp
Small-R Jets	JES strongly reduced	SysJET_GroupedNP_1
Small-R Jets	JES strongly reduced	SysJET_GroupedNP_2
Small-R Jets	JES strongly reduced	SysJET_GroupedNP_3
Small-R Jets	Energy resolution	SysJET_JER_SINGLE_NP
Large-R Jets	p_T scale	JET_Hbb
Large-R Jets	p_T resolution	JET_JER
Large-R Jets	Mass scale	JET_JMR
Large-R Jets	Mass resolution	JET_JMS
Track Jets	Flavor tagging scale factors	Sys_FT_EFF_Eigen_Light0
Track Jets	Flavor tagging scale factors	Sys_FT_EFF_Eigen_Light1
Track Jets	Flavor tagging scale factors	Sys_FT_EFF_Eigen_Light2
Track Jets	Flavor tagging scale factors	Sys_FT_EFF_Eigen_Light3
Track Jets	Flavor tagging scale factors	Sys_FT_EFF_Eigen_B0
Track Jets	Flavor tagging scale factors	Sys_FT_EFF_Eigen_B1
Track Jets	Flavor tagging scale factors	Sys_FT_EFF_Eigen_B2
Track Jets	Flavor tagging scale factors	Sys_FT_EFF_Eigen_C0
Track Jets	Flavor tagging scale factors	Sys_FT_EFF_Eigen_C1
Track Jets	Flavor tagging scale factors	Sys_FT_EFF_Eigen_C2
Track Jets	Flavor tagging scale factors	Sys_FT_EFF_Eigen_C3
Track Jets	Flavor tagging scale factors	Sys_FT_EFF_Eigen_extrapolation
Track Jets	Flavor tagging scale factors	Sys_FT_EFF_Eigen_extrapolation_from_charm
Modeling	$t\bar{t}$ Modeling	SysTop_Modeling
Modeling	$t\bar{t}$ RadHi/LO	SysTop_RadHi
Modeling	$t\bar{t}$ Herwig	SysTop_Herwig
Modeling	W+jets modeling	SysWjets_Modeling
Modeling	Z+jets modeling	SysZjets_Modeling
Modeling	diboson modeling	SysWW_Modeling

Table 6.2: Summary of the systematic uncertainties included in this analysis.

	1 b-tag	2 b-tags
$t\bar{t}$	201.64 ± 16.64 (0.74)	7.90 ± 1.42 (0.86)
single top	27.57 ± 7.20 (1.07)	2.07 ± 0.55 (1.08)
$W + b$	40.76 ± 11.18 (0.94)	6.96 ± 1.93 (0.93)
$W + c$	41.41 ± 11.87 (0.88)	0.64 ± 0.43 (0.71)
$W + l$	25.20 ± 7.23 (0.86)	0.10 ± 0.13 (2.64)
diboson	26.47 ± 3.72 (0.93)	3.92 ± 0.56 (0.99)
$Z + b$	89.70 ± 15.68 (1.04)	13.83 ± 2.83 (1.14)
$Z + c$	48.74 ± 13.39 (0.84)	1.06 ± 0.37 (0.84)
$Z + l$	36.43 ± 10.91 (0.86)	0.58 ± 0.33 (0.87)
backgrounds	539.45 ± 17.34 (0.85)	38.61 ± 2.98 (0.99)
data	508.00 ± 22.54	38.00 ± 6.16

Table 6.3: Expected and observed yields in the 0 lepton channel signal regions. Correlations between the expected yield uncertainty of individual backgrounds are not taken into account The ratio of postfit yield to prefit expectation is shown in parentheses.

	1 b-tag	2 b-tags
$t\bar{t}$	814.95 ± 37.75 (0.76)	59.61 ± 7.63 (0.87)
single top	89.14 ± 21.00 (0.84)	9.32 ± 2.32 (0.83)
$W + b$	78.41 ± 19.40 (0.72)	12.00 ± 3.68 (0.67)
$W + c$	87.46 ± 22.68 (0.84)	1.91 ± 0.56 (1.20)
$W + l$	57.80 ± 13.94 (0.83)	0.09 ± 0.04 (1.18)
diboson	26.21 ± 4.30 (0.96)	3.12 ± 0.49 (0.98)
$Z + b$	2.74 ± 2.25 (0.39)	0.43 ± 0.17 (0.79)
$Z + c$	0.00 ± 0.00 (0.00)	0.00 ± 0.00 (0.28)
$Z + l$	0.00 ± 0.00 (0.00)	0.00 ± 0.00 (1.15)
backgrounds	1156.71 ± 26.82 (0.77)	86.49 ± 6.63 (0.84)
data	1147.00 ± 33.87	85.00 ± 9.22

Table 6.4: Expected and observed yields in the 1 lepton channel signal regions. Correlations between the expected yield uncertainty of individual backgrounds are not taken into account The ratio of postfit yield to prefit expectation is shown in parentheses.

	1 b-tag	2 b-tags
$t\bar{t}$	8.78 ± 1.71 (0.93)	0.48 ± 0.22 (0.73)
single top	1.01 ± 0.31 (1.07)	0.05 ± 0.02 (1.04)
diboson	6.13 ± 1.42 (0.81)	1.09 ± 0.38 (0.98)
$Z + b$	38.73 ± 4.49 (0.98)	5.48 ± 0.87 (1.01)
$Z + c$	21.62 ± 5.61 (0.86)	0.18 ± 0.07 (0.85)
$Z + l$	8.37 ± 3.41 (1.03)	0.01 ± 0.02 (0.63)
backgrounds	84.63 ± 7.36 (0.93)	7.30 ± 1.03 (0.97)
data	75.00 ± 8.66	7.00 ± 2.65

Table 6.5: Expected and observed yields in the 2 lepton channel signal regions. Correlations between the expected yield uncertainty of individual backgrounds are not taken into account The ratio of postfit yield to prefit expectation is shown in parentheses.

Chapter 7

Conclusion

The Higgs boson discovered by the ATLAS and CMS collaborations in 2012 completes the discovery of the predicted standard model particles and is consistent with a standard model Higgs boson. The predicted decay modes of the Higgs have not all been experimentally observed. One of the as yet unobserved decay modes is the decay to quarks.

This thesis contains work that contributed to the search for $WH \rightarrow l\nu b\bar{b}$ using the Run 1 dataset of 20.3 fb^{-1} of data. The studies presented mostly focus on studies of the estimation of background processes, particularly the multijet background whose contribution must be derived using data driven techniques. This background is particularly challenging to model and great care must be taken when studying new techniques to improve its modelling. This analysis was not sensitive to Higgs decays consistent with the standard model but placed limits on the production cross section of this process of 4 times the standard model value for a Higgs of mass 125 GeV.

The main part of this thesis presents a summary of an analysis searching for heavy resonances that are predicted as a consequence of many BSM theories. In

order to be sensitive to high masses, selections for boosted topologies where the decay products are merged were used. In particular selections for excluding $t\bar{t}$ events were studied and are shown to have the potential to improve the sensitivity of boosted results in future studies. A benchmark model called the Heavy Vector Triplet (HVT) model is used to compare the cross section limits to theory. Two HVT models are considered. Model A has a coupling constant $g_V = 1$ and is excluded with mass $m_{V'} < 1450$ GeV in the 0 lepton channel, $m_{V'} < 1520$ GeV in the 1 lepton channel and $m_{V'} < 980$ GeV in the 2 lepton channel. Model B has a coupling constant $g_V = 3$ and is excluded up to a mass of $m_{V'} < 1760$ GeV in the 0 lepton channel, $m_{V'} < 1620$ GeV in the 1 lepton channel and $m_{V'} < 1400$ GeV in the 2 lepton channel. These limits exclude a similar mass range as the Run 1 ATLAS search and the Run 1 CMS boosted search using a much smaller dataset. There is also no evidence of the excess observed in the Run 1 CMS search.

Appendix

A Tables of Samples

DS ID	Process	Generator	$\sigma \times$ BR [nb]	k-factor	ϵ_{filter}
302341	HVT $\to WH \to l\nu qq$ model A $g_V = 1$ m 0500	MadGraph 2.2.2 + Pythia 8.186	1.24E-03	1.0	1.0
302342	HVT $\to WH \to l\nu qq$ model A $g_V = 1$ m 0600	MadGraph 2.2.2 + Pythia 8.186	6.23E-04	1.0	1.0
302343	HVT $\to WH \to l\nu qq$ model A $g_V = 1$ m 0700	MadGraph 2.2.2 + Pythia 8.186	3.45E-04	1.0	1.0
302344	HVT $\to WH \to l\nu qq$ model A $g_V = 1$ m 0800	MadGraph 2.2.2 + Pythia 8.186	2.04E-04	1.0	1.0
302345	HVT $\to WH \to l\nu qq$ model A $g_V = 1$ m 0900	MadGraph 2.2.2 + Pythia 8.186	1.27E-04	1.0	1.0
302346	HVT $\to WH \to l\nu qq$ model A $g_V = 1$ m 1000	MadGraph 2.2.2 + Pythia 8.186	8.28E-05	1.0	1.0
302347	HVT $\to WH \to l\nu qq$ model A $g_V = 1$ m 1100	MadGraph 2.2.2 + Pythia 8.186	5.55E-05	1.0	1.0
302348	HVT $\to WH \to l\nu qq$ model A $g_V = 1$ m 1200	MadGraph 2.2.2 + Pythia 8.186	3.81E-05	1.0	1.0
302349	HVT $\to WH \to l\nu qq$ model A $g_V = 1$ m 1300	MadGraph 2.2.2 + Pythia 8.186	2.67E-05	1.0	1.0
302350	HVT $\to WH \to l\nu qq$ model A $g_V = 1$ m 1400	MadGraph 2.2.2 + Pythia 8.186	1.91E-05	1.0	1.0
302351	HVT $\to WH \to l\nu qq$ model A $g_V = 1$ m 1500	MadGraph 2.2.2 + Pythia 8.186	1.39E-05	1.0	1.0
302352	HVT $\to WH \to l\nu qq$ model A $g_V = 1$ m 1600	MadGraph 2.2.2 + Pythia 8.186	1.03E-05	1.0	1.0
302353	HVT $\to WH \to l\nu qq$ model A $g_V = 1$ m 1700	MadGraph 2.2.2 + Pythia 8.186	7.64E-06	1.0	1.0
302354	HVT $\to WH \to l\nu qq$ model A $g_V = 1$ m 1800	MadGraph 2.2.2 + Pythia 8.186	5.75E-06	1.0	1.0
302355	HVT $\to WH \to l\nu qq$ model A $g_V = 1$ m 1900	MadGraph 2.2.2 + Pythia 8.186	4.37E-06	1.0	1.0
302356	HVT $\to WH \to l\nu qq$ model A $g_V = 1$ m 2000	MadGraph 2.2.2 + Pythia 8.186	3.35E-06	1.0	1.0
302357	HVT $\to WH \to l\nu qq$ model A $g_V = 1$ m 2200	MadGraph 2.2.2 + Pythia 8.186	2.01E-06	1.0	1.0
302358	HVT $\to WH \to l\nu qq$ model A $g_V = 1$ m 2400	MadGraph 2.2.2 + Pythia 8.186	1.23E-06	1.0	1.0
302359	HVT $\to WH \to l\nu qq$ model A $g_V = 1$ m 2600	MadGraph 2.2.2 + Pythia 8.186	7.66E-07	1.0	1.0
302360	HVT $\to WH \to l\nu qq$ model A $g_V = 1$ m 2800	MadGraph 2.2.2 + Pythia 8.186	4.84E-07	1.0	1.0
302361	HVT $\to WH \to l\nu qq$ model A $g_V = 1$ m 3000	MadGraph 2.2.2 + Pythia 8.186	3.10E-07	1.0	1.0
302362	HVT $\to WH \to l\nu qq$ model A $g_V = 1$ m 3500	MadGraph 2.2.2 + Pythia 8.186	1.05E-07	1.0	1.0
302363	HVT $\to WH \to l\nu qq$ model A $g_V = 1$ m 4000	MadGraph 2.2.2 + Pythia 8.186	3.72E-08	1.0	1.0
302364	HVT $\to WH \to l\nu qq$ model A $g_V = 1$ m 4500	MadGraph 2.2.2 + Pythia 8.186	1.34E-08	1.0	1.0
302365	HVT $\to WH \to l\nu qq$ model A $g_V = 1$ m 5000	MadGraph 2.2.2 + Pythia 8.186	4.85E-09	1.0	1.0
302391	HVT $\to ZH \to llqq$ model A $g_V = 1$ m0500	MadGraph 2.2.2 + Pythia 8.186	2.08E-04	1.0	1.0
302392	HVT $\to ZH \to llqq$ model A $g_V = 1$ m0600	MadGraph 2.2.2 + Pythia 8.186	1.03E-04	1.0	1.0
302393	HVT $\to ZH \to llqq$ model A $g_V = 1$ m0700	MadGraph 2.2.2 + Pythia 8.186	5.60E-05	1.0	1.0
302394	HVT $\to ZH \to llqq$ model A $g_V = 1$ m0800	MadGraph 2.2.2 + Pythia 8.186	3.28E-05	1.0	1.0
302395	HVT $\to ZH \to llqq$ model A $g_V = 1$ m0900	MadGraph 2.2.2 + Pythia 8.186	2.02E-05	1.0	1.0
302396	HVT $\to ZH \to llqq$ model A $g_V = 1$ m1000	MadGraph 2.2.2 + Pythia 8.186	1.30E-05	1.0	1.0
302397	HVT $\to ZH \to llqq$ model A $g_V = 1$ m1100	MadGraph 2.2.2 + Pythia 8.186	8.62E-06	1.0	1.0
302398	HVT $\to ZH \to llqq$ model A $g_V = 1$ m1200	MadGraph 2.2.2 + Pythia 8.186	5.88E-06	1.0	1.0
302399	HVT $\to ZH \to llqq$ model A $g_V = 1$ m1300	MadGraph 2.2.2 + Pythia 8.186	4.10E-06	1.0	1.0
302400	HVT $\to ZH \to llqq$ model A $g_V = 1$ m1400	MadGraph 2.2.2 + Pythia 8.186	2.91E-06	1.0	1.0
302401	HVT $\to ZH \to llqq$ model A $g_V = 1$ m1500	MadGraph 2.2.2 + Pythia 8.186	2.11E-06	1.0	1.0
302402	HVT $\to ZH \to llqq$ model A $g_V = 1$ m1600	MadGraph 2.2.2 + Pythia 8.186	1.54E-06	1.0	1.0
302403	HVT $\to ZH \to llqq$ model A $g_V = 1$ m1700	MadGraph 2.2.2 + Pythia 8.186	1.14E-06	1.0	1.0
302404	HVT $\to ZH \to llqq$ model A $g_V = 1$ m1800	MadGraph 2.2.2 + Pythia 8.186	8.57E-07	1.0	1.0
302405	HVT $\to ZH \to llqq$ model A $g_V = 1$ m1900	MadGraph 2.2.2 + Pythia 8.186	6.48E-07	1.0	1.0
302406	HVT $\to ZH \to llqq$ model A $g_V = 1$ m2000	MadGraph 2.2.2 + Pythia 8.186	4.94E-07	1.0	1.0
302407	HVT $\to ZH \to llqq$ model A $g_V = 1$ m2200	MadGraph 2.2.2 + Pythia 8.186	2.94E-07	1.0	1.0
302408	HVT $\to ZH \to llqq$ model A $g_V = 1$ m2400	MadGraph 2.2.2 + Pythia 8.186	1.79E-07	1.0	1.0
302409	HVT $\to ZH \to llqq$ model A $g_V = 1$ m2600	MadGraph 2.2.2 + Pythia 8.186	1.11E-07	1.0	1.0
302410	HVT $\to ZH \to llqq$ model A $g_V = 1$ m2800	MadGraph 2.2.2 + Pythia 8.186	7.01E-08	1.0	1.0
302411	HVT $\to ZH \to llqq$ model A $g_V = 1$ m3000	MadGraph 2.2.2 + Pythia 8.186	4.48E-08	1.0	1.0
302412	HVT $\to ZH \to llqq$ model A $g_V = 1$ m3500	MadGraph 2.2.2 + Pythia 8.186	1.53E-08	1.0	1.0
302413	HVT $\to ZH \to llqq$ model A $g_V = 1$ m4000	MadGraph 2.2.2 + Pythia 8.186	5.41E-09	1.0	1.0
302414	HVT $\to ZH \to llqq$ model A $g_V = 1$ m4500	MadGraph 2.2.2 + Pythia 8.186	1.96E-09	1.0	1.0
302415	HVT $\to ZH \to llqq$ model A $g_V = 1$ m5000	MadGraph 2.2.2 + Pythia 8.186	7.17E-10	1.0	1.0
302416	HVT $\to ZH \to \nu\nu qq$ model A $g_V = 1$ m0500	MadGraph 2.2.2 + Pythia 8.186	4.15E-04	1.0	1.0
302417	HVT $\to ZH \to \nu\nu qq$ model A $g_V = 1$ m0600	MadGraph 2.2.2 + Pythia 8.186	2.04E-04	1.0	1.0
302418	HVT $\to ZH \to \nu\nu qq$ model A $g_V = 1$ m0700	MadGraph 2.2.2 + Pythia 8.186	1.11E-04	1.0	1.0
302419	HVT $\to ZH \to \nu\nu qq$ model A $g_V = 1$ m0800	MadGraph 2.2.2 + Pythia 8.186	6.51E-05	1.0	1.0
302420	HVT $\to ZH \to \nu\nu qq$ model A $g_V = 1$ m0900	MadGraph 2.2.2 + Pythia 8.186	4.02E-05	1.0	1.0
302421	HVT $\to ZH \to \nu\nu qq$ model A $g_V = 1$ m1000	MadGraph 2.2.2 + Pythia 8.186	2.58E-05	1.0	1.0
302422	HVT $\to ZH \to \nu\nu qq$ model A $g_V = 1$ m1100	MadGraph 2.2.2 + Pythia 8.186	1.71E-05	1.0	1.0
302423	HVT $\to ZH \to \nu\nu qq$ model A $g_V = 1$ m1200	MadGraph 2.2.2 + Pythia 8.186	1.17E-05	1.0	1.0
302424	HVT $\to ZH \to \nu\nu qq$ model A $g_V = 1$ m1300	MadGraph 2.2.2 + Pythia 8.186	8.16E-06	1.0	1.0
302425	HVT $\to ZH \to \nu\nu qq$ model A $g_V = 1$ m1400	MadGraph 2.2.2 + Pythia 8.186	5.80E-06	1.0	1.0
302426	HVT $\to ZH \to \nu\nu qq$ model A $g_V = 1$ m1500	MadGraph 2.2.2 + Pythia 8.186	4.19E-06	1.0	1.0
302427	HVT $\to ZH \to \nu\nu qq$ model A $g_V = 1$ m1600	MadGraph 2.2.2 + Pythia 8.186	3.07E-06	1.0	1.0
302428	HVT $\to ZH \to \nu\nu qq$ model A $g_V = 1$ m1700	MadGraph 2.2.2 + Pythia 8.186	2.27E-06	1.0	1.0
302429	HVT $\to ZH \to \nu\nu qq$ model A $g_V = 1$ m1800	MadGraph 2.2.2 + Pythia 8.186	1.70E-06	1.0	1.0
302430	HVT $\to ZH \to \nu\nu qq$ model A $g_V = 1$ m1900	MadGraph 2.2.2 + Pythia 8.186	1.29E-06	1.0	1.0
302431	HVT $\to ZH \to \nu\nu qq$ model A $g_V = 1$ m2000	MadGraph 2.2.2 + Pythia 8.186	9.83E-07	1.0	1.0
302432	HVT $\to ZH \to \nu\nu qq$ model A $g_V = 1$ m2200	MadGraph 2.2.2 + Pythia 8.186	5.85E-07	1.0	1.0
302433	HVT $\to ZH \to \nu\nu qq$ model A $g_V = 1$ m2400	MadGraph 2.2.2 + Pythia 8.186	3.56E-07	1.0	1.0
302434	HVT $\to ZH \to \nu\nu qq$ model A $g_V = 1$ m2600	MadGraph 2.2.2 + Pythia 8.186	2.21E-07	1.0	1.0
302435	HVT $\to ZH \to \nu\nu qq$ model A $g_V = 1$ m2800	MadGraph 2.2.2 + Pythia 8.186	1.40E-07	1.0	1.0
302436	HVT $\to ZH \to \nu\nu qq$ model A $g_V = 1$ m3000	MadGraph 2.2.2 + Pythia 8.186	8.92E-08	1.0	1.0
302437	HVT $\to ZH \to \nu\nu qq$ model A $g_V = 1$ m3500	MadGraph 2.2.2 + Pythia 8.186	3.04E-08	1.0	1.0
302438	HVT $\to ZH \to \nu\nu qq$ model A $g_V = 1$ m4000	MadGraph 2.2.2 + Pythia 8.186	1.08E-08	1.0	1.0
302439	HVT $\to ZH \to \nu\nu qq$ model A $g_V = 1$ m4500	MadGraph 2.2.2 + Pythia 8.186	3.90E-09	1.0	1.0
302440	HVT $\to ZH \to \nu\nu qq$ model A $g_V = 1$ m5000	MadGraph 2.2.2 + Pythia 8.186	1.43E-09	1.0	1.0

Table 1: HVT samples used in the VH resonance analysis. Model A with $g_V = 1$ for a variety of resonance masses (m). The dataset ID, MC generator, production cross-sections, k-factor and filter efficiency are shown.

DS ID	Process	Generator	$\sigma \times$ BR [nb]	k-factor	ϵ_{filter}
361300	$W \to e\nu$, $0 < p_{\text{T}}^{W} < 70$ GeV, C veto & B veto	Sherpa	21.282	0.9082	8.9071E-01
361301	$W \to e\nu$, $0 < p_{\text{T}}^{W} < 70$ GeV, C filter & B Veto	Sherpa	21.38	0.9082	4.9372E-02
361302	$W \to e\nu$, $0 < p_{\text{T}}^{W} < 70$ GeV, B filter	Sherpa	21.387	0.9082	6.0335E-02
361303	$W \to e\nu$, $70 < p_{\text{T}}^{W} < 140$ GeV, C Veto & B Veto	Sherpa	0.63343	0.9082	7.2614E-01
361304	$W \to e\nu$, $70 < p_{\text{T}}^{W} < 140$ GeV, C filter & B Veto	Sherpa	0.63129	0.9082	1.6970E-01
361305	$W \to e\nu$, $70 < p_{\text{T}}^{W} < 140$ GeV, B filter	Sherpa	0.62626	0.9082	9.3115E-02
361306	$W \to e\nu$, $140 < p_{\text{T}}^{W} < 280$ GeV, C Veto & B Veto	Sherpa	0.090131	0.9082	6.7301E-01
361307	$W \to e\nu$, $140 < p_{\text{T}}^{W} < 280$ GeV, C filter & B Veto	Sherpa	0.089902	0.9082	2.0036E-01
361308	$W \to e\nu$, $140 < p_{\text{T}}^{W} < 280$ GeV, B filter	Sherpa	0.090042	0.9082	1.0370E-01
361309	$W \to e\nu$, $280 < p_{\text{T}}^{W} < 500$ GeV, C Veto & B Veto	Sherpa	0.0065313	0.9082	6.8555E-01
361310	$W \to e\nu$, $280 < p_{\text{T}}^{W} < 500$ GeV, C filter & B Veto	Sherpa	.0065434	0.9082	2.0617E-01
361311	$W \to e\nu$, $280 < p_{\text{T}}^{W} < 500$ GeV, B filter	Sherpa	.0065128	0.9082	9.4692E-02
361312	$W \to e\nu$, $500 < p_{\text{T}}^{W} < 700$ GeV, C Veto & B Veto	Sherpa	.00041774	0.9082	6.1653E-01
361313	$W \to e\nu$, $500 < p_{\text{T}}^{W} < 700$ GeV, C filter & B Veto	Sherpa	.00040599	0.9082	1.4761E-01
361314	$W \to e\nu$, $500 < p_{\text{T}}^{W} < 700$ GeV, B filter	Sherpa	4.1765E-04	0.9082	5.4242E-02
361315	$W \to e\nu$, $700 < p_{\text{T}}^{W} < 1000$ GeV, C Veto & B Veto	Sherpa	7.3374E-05	0.9082	7.1643E-01
361318	$W \to e\nu$, $1000 < p_{\text{T}}^{W} < 2000$ GeV, C Veto & B Veto	Sherpa	1.1153E-05	0.9082	5.8685E-01
361324	$W \to \mu\nu$, $0 < p_{\text{T}}^{W} < 70$ GeV, C veto & B veto	Sherpa	21.392	0.9082	8.9238E-01
361325	$W \to \mu\nu$, $0 < p_{\text{T}}^{W} < 70$ GeV, C filter & B Veto	Sherpa	21.38	0.9082	4.6934E-02
361326	$W \to \mu\nu$, $0 < p_{\text{T}}^{W} < 70$ GeV, B filter	Sherpa	21.371	0.9082	5.9494E-02
361327	$W \to \mu\nu$, $70 < p_{\text{T}}^{W} < 140$ GeV, C Veto & B Veto	Sherpa	.63461	0.9082	7.2483E-01
361328	$W \to \mu\nu$, $70 < p_{\text{T}}^{W} < 140$ GeV, C filter & B Veto	Sherpa	.63172	0.9082	1.6535E-01
361329	$W \to \mu\nu$, $70 < p_{\text{T}}^{W} < 140$ GeV, B filter	Sherpa	.63254	0.9082	9.1969E-02
361330	$W \to \mu\nu$, $140 < p_{\text{T}}^{W} < 280$ GeV, C Veto & B Veto	Sherpa	.089788	0.9082	6.8291E-01
361331	$W \to \mu\nu$, $140 < p_{\text{T}}^{W} < 280$ GeV, C filter & B Veto	Sherpa	.090096	0.9082	1.9755E-01
361332	$W \to \mu\nu$, $140 < p_{\text{T}}^{W} < 280$ GeV, B filter	Sherpa	.090322	0.9082	1.0287E-01
361333	$W \to \mu\nu$, $280 < p_{\text{T}}^{W} < 500$ GeV, C Veto & B Veto	Sherpa	.0065147	0.9082	6.1790E-01
361334	$W \to \mu\nu$, $280 < p_{\text{T}}^{W} < 500$ GeV, C filter & B Veto	Sherpa	.0064669	0.9082	1.8794E-01
361335	$W \to \mu\nu$, $280 < p_{\text{T}}^{W} < 500$ GeV, B filter	Sherpa	.0065767	0.9082	1.1282E-01
361336	$W \to \mu\nu$, $500 < p_{\text{T}}^{W} < 700$ GeV, C Veto & B Veto	Sherpa	4.0872E-04	0.9082	6.4016E-01
361337	$W \to \mu\nu$, $500 < p_{\text{T}}^{W} < 700$ GeV, C filter & B Veto	Sherpa	4.2067E-04	0.9082	2.0561E-01
361338	$W \to \mu\nu$, $500 < p_{\text{T}}^{W} < 700$ GeV, B filter	Sherpa	4.2374E-04	0.9082	2.9486E-02
361339	$W \to \mu\nu$, $700 < p_{\text{T}}^{W} < 1000$ GeV, C Veto & B Veto	Sherpa	7.6219E-05	0.9082	5.5516E-01
361340	$W \to \mu\nu$, $700 < p_{\text{T}}^{W} < 1000$ GeV, C filter & B Veto	Sherpa	7.6663E-05	0.9082	2.3782E-01
361341	$W \to \mu\nu$, $700 < p_{\text{T}}^{W} < 1000$ GeV, B filter	Sherpa	8.1099E-05	0.9082	3.3736E-02
361342	$W \to \mu\nu$, $1000 < p_{\text{T}}^{W} < 2000$ GeV, C Veto & B Veto	Sherpa	1.0488E-05	0.9082	5.1867E-01
361343	$W \to \mu\nu$, $1000 < p_{\text{T}}^{W} < 2000$ GeV, C filter & B Veto	Sherpa	9.6847E-06	0.9082	5.3716E-01
361344	$W \to \mu\nu$, $1000 < p_{\text{T}}^{W} < 2000$ GeV, B filter	Sherpa	.000010382	0.9082	2.3205E-01
361345	$W \to \mu\nu$, $p_{\text{T}}^{W} > 2000$ GeV, C Veto & B Veto	Sherpa	.000000041826	0.9082	5.2889E-01
361346	$W \to \mu\nu$, $p_{\text{T}}^{W} > 2000$ GeV, C filter & B Veto	Sherpa	5.2097E-08	0.9082	1.9407E-02
361347	$W \to \mu\nu$, $p_{\text{T}}^{W} > 2000$ GeV, B filter	Sherpa	.0000000079217	0.9082	1.928E-01
361348	$W \to \tau\nu$, $0 < p_{\text{T}}^{W} < 70$ GeV, C veto & B veto	Sherpa	21.386	0.9082	8.9141E-01
361349	$W \to \tau\nu$, $0 < p_{\text{T}}^{W} < 70$ GeV, C filter & B Veto	Sherpa	21.378	0.9082	4.8220E-02
361350	$W \to \tau\nu$, $0 < p_{\text{T}}^{W} < 70$ GeV, B filter	Sherpa	21.386	0.9082	5.9467E-02
361351	$W \to \tau\nu$, $70 < p_{\text{T}}^{W} < 140$ GeV, C Veto & B Veto	Sherpa	.63153	0.9082	7.2272E-01
361352	$W \to \tau\nu$, $70 < p_{\text{T}}^{W} < 140$ GeV, C filter & B Veto	Sherpa	.63444	0.9082	1.6764E-01
361353	$W \to \tau\nu$, $70 < p_{\text{T}}^{W} < 140$ GeV, B filter	Sherpa	.6312	0.9082	7.7419E-02
361354	$W \to \tau\nu$, $140 < p_{\text{T}}^{W} < 280$ GeV, C Veto & B Veto	Sherpa	.090227	0.9082	6.8082E-01
361355	$W \to \tau\nu$, $140 < p_{\text{T}}^{W} < 280$ GeV, C filter & B Veto	Sherpa	.089983	0.9082	1.9577E-01
361356	$W \to \tau\nu$, $140 < p_{\text{T}}^{W} < 280$ GeV, B filter	Sherpa	.089974	0.9082	1.0303E-01
361357	$W \to \tau\nu$, $280 < p_{\text{T}}^{W} < 500$ GeV, C Veto & B Veto	Sherpa	.0064488	0.9082	6.4445E-01
361358	$W \to \tau\nu$, $280 < p_{\text{T}}^{W} < 500$ GeV, C filter & B Veto	Sherpa	.0065992	0.9082	1.8110E-01
361359	$W \to \tau\nu$, $280 < p_{\text{T}}^{W} < 500$ GeV, B filter	Sherpa	.0064523	0.9082	1.4653E-01
361360	$W \to \tau\nu$, $500 < p_{\text{T}}^{W} < 700$ GeV, C Veto & B Veto	Sherpa	4.1485E-04	0.9082	5.3423E-01
361361	$W \to \tau\nu$, $500 < p_{\text{T}}^{W} < 700$ GeV, C filter & B Veto	Sherpa	4.1469E-04	0.9082	1.8010E-01
361362	$W \to \tau\nu$, $500 < p_{\text{T}}^{W} < 700$ GeV, B filter	Sherpa	.00040957	0.9082	3.4870E-02
361363	$W \to \tau\nu$, $700 < p_{\text{T}}^{W} < 1000$ GeV, C veto & B veto	Sherpa	7.9290E-05	0.9082	4.5007E-01
361364	$W \to \tau\nu$, $700 < p_{\text{T}}^{W} < 1000$ GeV, C filter & B Veto	Sherpa	.00007821	0.9082	1.6420E-01
361365	$W \to \tau\nu$, $700 < p_{\text{T}}^{W} < 1000$ GeV, B filter	Sherpa	.000080632	0.9082	2.3548E-02
361366	$W \to \tau\nu$, $1000 < p_{\text{T}}^{W} < 2000$ GeV, C veto & B veto	Sherpa	1.0483E-05	0.9082	5.7685E-01
361367	$W \to \tau\nu$, $1000 < p_{\text{T}}^{W} < 2000$ GeV, C filter & B Veto	Sherpa	.000010108	0.9082	6.1001E-02
361368	$W \to \tau\nu$, $1000 < p_{\text{T}}^{W} < 2000$ GeV, B filter	Sherpa	1.0536E-05	0.9082	1.3238E-01
361369	$W \to \tau\nu$, $p_{\text{T}}^{W} > 2000$ GeV, C veto & B veto	Sherpa	4.5746E-08	0.9082	6.2486E-01
361370	$W \to \tau\nu$, $p_{\text{T}}^{W} > 2000$ GeV, C filter & B Veto	Sherpa	4.9643E-08	0.9082	2.9935E-01
361371	$W \to \tau\nu$, $p_{\text{T}}^{W} > 2000$ GeV, B filter	Sherpa	.000000048667	0.9082	9.9696E-01

Table 2: W+jets samples used in the analysis. The dataset ID, MC generator, production crossection, k-factor and filter efficiency are shown.

DS ID	Process	Generator	$\sigma \times$ BR [nb]	k-factor	ϵ_{filter}
361372	$Z \to ee$, $0 < p_{\mathrm{T}}^{Z} < 70$ GeV, C veto & B veto	Sherpa	2.2067	9.013000E-01	7.7884E-01
361373	$Z \to ee$, $0 < p_{\mathrm{T}}^{Z} < 70$ GeV, C filter & B Veto	Sherpa	2.2058	9.013000E-01	1.4619E-01
361374	$Z \to ee$, $0 < p_{\mathrm{T}}^{Z} < 70$ GeV, B filter	Sherpa	2.2048	9.013000E-01	7.8489E-02
361375	$Z \to ee$, $70 < p_{\mathrm{T}}^{Z} < 140$ GeV, C veto & B veto	Sherpa	.075673	9.013000E-01	6.4226E-01
361376	$Z \to ee$, $70 < p_{\mathrm{T}}^{Z} < 140$ GeV, C filter & B Veto	Sherpa	.07587	9.013000E-01	2.1077E-01
361377	$Z \to ee$, $70 < p_{\mathrm{T}}^{Z} < 140$ GeV, B filter	Sherpa	.076416	9.013000E-01	1.2226E-01
361378	$Z \to ee$, $140 < p_{\mathrm{T}}^{Z} < 280$ GeV, C veto & B veto	Sherpa	1.1755E-02	9.013000E-01	6.0206E-01
361379	$Z \to ee$, $140 < p_{\mathrm{T}}^{Z} < 280$ GeV, C filter & B Veto	Sherpa	1.1508E-02	9.013000E-01	2.5335E-01
361380	$Z \to ee$, $140 < p_{\mathrm{T}}^{Z} < 280$ GeV, B filter	Sherpa	.011661	9.013000E-01	1.3657E-01
361381	$Z \to ee$, $280 < p_{\mathrm{T}}^{Z} < 500$ GeV, C veto & B veto	Sherpa	7.8842E-04	9.013000E-01	6.0463E-01
361382	$Z \to ee$, $280 < p_{\mathrm{T}}^{Z} < 500$ GeV, C filter & B Veto	Sherpa	.00084681	9.013000E-01	2.1611E-01
361383	$Z \to ee$, $280 < p_{\mathrm{T}}^{Z} < 500$ GeV, B filter	Sherpa	.00086361	9.013000E-01	1.1785E-01
361384	$Z \to ee$, $500 < p_{\mathrm{T}}^{Z} < 700$ GeV, C veto & B veto	Sherpa	5.1808E-05	9.013000E-01	5.4617E-01
361385	$Z \to ee$, $500 < p_{\mathrm{T}}^{Z} < 700$ GeV, C filter & B Veto	Sherpa	5.3763E-05	9.013000E-01	1.1778E-01
361386	$Z \to ee$, $500 < p_{\mathrm{T}}^{Z} < 700$ GeV, B filter	Sherpa	5.6362E-05	9.013000E-01	1.1746E-01
361387	$Z \to ee$, $700 < p_{\mathrm{T}}^{Z} < 1000$ GeV, C veto & B veto	Sherpa	1.0377E-05	9.013000E-01	5.3246E-01
361388	$Z \to ee$, $700 < p_{\mathrm{T}}^{Z} < 1000$ GeV, C filter & B Veto	Sherpa	.000010064	9.013000E-01	2.5809E-01
361389	$Z \to ee$, $700 < p_{\mathrm{T}}^{Z} < 1000$ GeV, B filter	Sherpa	.000010301	9.013000E-01	1.4638E-02
361390	$Z \to ee$, $1000 < p_{\mathrm{T}}^{Z} < 2000$ GeV, C veto & B veto	Sherpa	.000001356	9.013000E-01	5.3809E-01
361391	$Z \to ee$, $1000 < p_{\mathrm{T}}^{Z} < 2000$ GeV, C filter & B Veto	Sherpa	1.4825E-06	9.013000E-01	-4.6726E-01
361392	$Z \to ee$, $1000 < p_{\mathrm{T}}^{Z} < 2000$ GeV, B filter	Sherpa	1.3407E-06	9.013000E-01	6.7971E-03
361393	$Z \to ee$, $p_{\mathrm{T}}^{Z} > 2000$ GeV, C veto & B veto	Sherpa	.0000000061317	9.013000E-01	3.4161E-01
361394	$Z \to ee$, $p_{\mathrm{T}}^{Z} > 2000$ GeV, C filter & B Veto	Sherpa	.0000000077689	9.013000E-01	3.932E-01
361395	$Z \to ee$, $p_{\mathrm{T}}^{Z} > 2000$ GeV, B filter	Sherpa	.0000000093603	9.013000E-01	9.9696E-01
361396	$Z \to \mu\mu$, $0 < p_{\mathrm{T}}^{Z} < 70$ GeV, C veto & B veto	Sherpa	2.2057	9.013000E-01	7.7824E-01
361397	$Z \to \mu\mu$, $0 < p_{\mathrm{T}}^{Z} < 70$ GeV, C filter & B Veto	Sherpa	2.2055	9.013000E-01	1.4120E-01
361398	$Z \to \mu\mu$, $0 < p_{\mathrm{T}}^{Z} < 70$ GeV, B filter	Sherpa	2.2028	9.013000E-01	7.8596E-02
361399	$Z \to \mu\mu$, $70 < p_{\mathrm{T}}^{Z} < 140$ GeV, C veto & B veto	Sherpa	.075889	9.013000E-01	6.4618E-01
361400	$Z \to \mu\mu$, $70 < p_{\mathrm{T}}^{Z} < 140$ GeV, C filter & B Veto	Sherpa	.076179	9.013000E-01	2.1400E-01
361401	$Z \to \mu\mu$, $70 < p_{\mathrm{T}}^{Z} < 140$ GeV, B filter	Sherpa	.075957	9.013000E-01	1.2446E-01
361402	$Z \to \mu\mu$, $140 < p_{\mathrm{T}}^{Z} < 280$ GeV, C veto & B veto	Sherpa	.011621	9.013000E-01	5.9966E-01
361403	$Z \to \mu\mu$, $140 < p_{\mathrm{T}}^{Z} < 280$ GeV, C filter & B Veto	Sherpa	1.1623E-02	9.013000E-01	2.3279E-01
361404	$Z \to \mu\mu$, $140 < p_{\mathrm{T}}^{Z} < 280$ GeV, B filter	Sherpa	1.1675E-02	9.013000E-01	1.3106E-01
361405	$Z \to \mu\mu$, $280 < p_{\mathrm{T}}^{Z} < 500$ GeV, C veto & B veto	Sherpa	.00086315	9.013000E-01	5.6559E-01
361406	$Z \to \mu\mu$, $280 < p_{\mathrm{T}}^{Z} < 500$ GeV, C filter & B Veto	Sherpa	.00086721	9.013000E-01	1.4855E-01
361407	$Z \to \mu\mu$, $280 < p_{\mathrm{T}}^{Z} < 500$ GeV, B filter	Sherpa	.00086299	9.013000E-01	-5.9687E-02
361408	$Z \to \mu\mu$, $500 < p_{\mathrm{T}}^{Z} < 700$ GeV, C veto & B veto	Sherpa	5.4434E-05	9.013000E-01	5.1198E-01
361409	$Z \to \mu\mu$, $500 < p_{\mathrm{T}}^{Z} < 700$ GeV, C filter & B Veto	Sherpa	.000056231	9.013000E-01	2.0911E-01
361410	$Z \to \mu\mu$, $500 < p_{\mathrm{T}}^{Z} < 700$ GeV, B filter	Sherpa	5.4956E-05	9.013000E-01	1.2801E-01
361411	$Z \to \mu\mu$, $700 < p_{\mathrm{T}}^{Z} < 1000$ GeV, C veto & B veto	Sherpa	8.4073E-06	9.013000E-01	7.5718E-01
361412	$Z \to \mu\mu$, $700 < p_{\mathrm{T}}^{Z} < 1000$ GeV, C filter & B Veto	Sherpa	.0000098594	9.013000E-01	1.9152E-01
361413	$Z \to \mu\mu$, $700 < p_{\mathrm{T}}^{Z} < 1000$ GeV, B filter	Sherpa	.000010204	9.013000E-01	6.6507E-02
361414	$Z \to \mu\mu$, $1000 < p_{\mathrm{T}}^{Z} < 2000$ GeV, C veto & B veto	Sherpa	1.2484E-06	9.013000E-01	4.9980E-01
361415	$Z \to \mu\mu$, $1000 < p_{\mathrm{T}}^{Z} < 2000$ GeV, C filter & B Veto	Sherpa	1.3946E-06	9.013000E-01	2.7664E-01
361416	$Z \to \mu\mu$, $1000 < p_{\mathrm{T}}^{Z} < 2000$ GeV, B filter	Sherpa	1.4081E-06	9.013000E-01	7.2108E-02
361417	$Z \to \mu\mu$, $p_{\mathrm{T}}^{Z} > 2000$ GeV, C veto & B veto	Sherpa	6.6745E-09	9.013000E-01	1.0242E+00
361418	$Z \to \mu\mu$, $p_{\mathrm{T}}^{Z} > 2000$ GeV, C filter & B Veto	Sherpa	.0000000067807	9.013000E-01	9.9696E-01
361419	$Z \to \mu\mu$, $p_{\mathrm{T}}^{Z} > 2000$ GeV, B filter	Sherpa	.000000012968	9.013000E-01	2.466E-01
361420	$Z \to \tau\tau$,$0 < p_{\mathrm{T}}^{Z} < 70$ GeV, C Veto B Veto	Sherpa	2.196500E+03	9.013000E-01	7.781400E-01
361421	$Z \to \tau\tau$,$0 < p_{\mathrm{T}}^{Z} < 70$ GeV, C Filter B Veto	Sherpa	2.204100E+03	9.013000E-01	1.423350E-01
361422	$Z \to \tau\tau$,$0 < p_{\mathrm{T}}^{Z} < 70$ GeV, B Filter	Sherpa	2.205100E+03	9.013000E-01	7.921500E-02
361423	$Z \to \tau\tau$,$70 < p_{\mathrm{T}}^{Z} < 140$ GeV, C Veto B Veto	Sherpa	7.632200E+01	9.013000E-01	6.479450E-01
361424	$Z \to \tau\tau$,$70 < p_{\mathrm{T}}^{Z} < 140$ GeV, C Filter B Veto	Sherpa	7.600400E+01	9.013000E-01	2.220030E-01
361425	$Z \to \tau\tau$,$70 < p_{\mathrm{T}}^{Z} < 140$ GeV, B Filter	Sherpa	7.636900E+01	9.013000E-01	1.312250E-01
361426	$Z \to \tau\tau$,$140 < p_{\mathrm{T}}^{Z} < 280$ GeV, C Veto B Veto	Sherpa	1.156900E+01	9.013000E-01	6.145030E-01
361427	$Z \to \tau\tau$,$140 < p_{\mathrm{T}}^{Z} < 280$ GeV, C Filter B Veto	Sherpa	1.164900E+01	9.013000E-01	2.417050E-01
361428	$Z \to \tau\tau$,$140 < p_{\mathrm{T}}^{Z} < 280$ GeV, B Filter	Sherpa	1.161200E+01	9.013000E-01	1.420800E-01
361429	$Z \to \tau\tau$,$280 < p_{\mathrm{T}}^{Z} < 500$ GeV, C Veto B Veto	Sherpa	8.697300E-01	9.013000E-01	5.810190E-01
361430	$Z \to \tau\tau$,$280 < p_{\mathrm{T}}^{Z} < 500$ GeV, C Filter B Veto	Sherpa	8.702000E-01	9.013000E-01	2.557750E-01
361431	$Z \to \tau\tau$,$280 < p_{\mathrm{T}}^{Z} < 500$ GeV, B Filter	Sherpa	8.751400E-01	9.013000E-01	1.588590E-01
361432	$Z \to \tau\tau$,$500 < p_{\mathrm{T}}^{Z} < 700$ GeV, C Veto B Veto	Sherpa	5.580600E-02	9.013000E-01	5.639030E-01
361433	$Z \to \tau\tau$,$500 < p_{\mathrm{T}}^{Z} < 700$ GeV, C Filter B Veto	Sherpa	5.507500E-02	9.013000E-01	2.704310E-01
361434	$Z \to \tau\tau$,$500 < p_{\mathrm{T}}^{Z} < 700$ GeV, B Filter	Sherpa	5.514700E-02	9.013000E-01	1.704540E-01
361435	$Z \to \tau\tau$,$700 < p_{\mathrm{T}}^{Z} < 1000$ GeV, C Veto B Veto	Sherpa	9.514300E-03	9.013000E-01	5.601840E-01
361436	$Z \to \tau\tau$,$700 < p_{\mathrm{T}}^{Z} < 1000$ GeV, C Filter B Veto	Sherpa	9.874000E-03	9.013000E-01	2.984140E-01
361437	$Z \to \tau\tau$,$700 < p_{\mathrm{T}}^{Z} < 1000$ GeV, B Filter	Sherpa	1.047700E-02	9.013000E-01	1.801180E-01
361438	$Z \to \tau\tau$,$1000 < p_{\mathrm{T}}^{Z} < 2000$ GeV, C Veto B Veto	Sherpa	1.354400E-03	9.013000E-01	5.636100E-01
361439	$Z \to \tau\tau$,$1000 < p_{\mathrm{T}}^{Z} < 2000$ GeV, C Filter B Veto	Sherpa	1.260900E-03	9.013000E-01	3.482770E-01
361440	$Z \to \tau\tau$,$1000 < p_{\mathrm{T}}^{Z} < 2000$ GeV, B Filter	Sherpa	1.354900E-03	9.013000E-01	1.684620E-01
361441	$Z \to \tau\tau$,$p_{\mathrm{T}}^{Z} > 2000$ GeV, C Veto B Veto	Sherpa	6.113300E-06	9.013000E-01	5.954060E-01
361442	$Z \to \tau\tau$,$p_{\mathrm{T}}^{Z} > 2000$ GeV, C Filter B Veto	Sherpa	6.497900E-06	9.013000E-01	3.599530E-01
361443	$Z \to \tau\tau$,$p_{\mathrm{T}}^{Z} > 2000$ GeV, B Filter	Sherpa	9.757200E-06	9.013000E-01	2.508460E-01

Table 3: Z+jets samples used in the analysis. The dataset ID, MC generator, production crossection, k-factor and filter efficiency are shown.

Table 4: $Z \to \nu\nu$+jets samples used in the analysis. The dataset ID, MC generator, production crossection, k-factor and filter efficiency are shown.

DS ID	Process	Generator	$\sigma \times$ BR [pb]	k-factor	ϵ_{filter}
361444	$Z \to \nu\nu$, $0 < p_{\text{T}}^{Z} < 70$ GeV, C veto and B veto	Sherpa	1.194e+04	0.9374	0.7785
361445	$Z \to \nu\nu$, $0 < p_{\text{T}}^{Z} < 70$ GeV, C filter and B veto	Sherpa	1.194e+04	0.9374	0.1401
361446	$Z \to \nu\nu$, $0 < p_{\text{T}}^{Z} < 70$ GeV, B filter	Sherpa	1.194e+04	0.9374	0.0800
361447	$Z \to \nu\nu$, $70 < p_{\text{T}}^{Z} < 140$ GeV, C veto and B veto	Sherpa	428.4	0.9374	0.6496
361448	$Z \to \nu\nu$, $70 < p_{\text{T}}^{Z} < 140$ GeV, C filter and B veto	Sherpa	428.4	0.9374	0.2184
361449	$Z \to \nu\nu$, $70 < p_{\text{T}}^{Z} < 140$ GeV, B filter	Sherpa	428.4	0.9374	0.1328
361450	$Z \to \nu\nu$, $140 < p_{\text{T}}^{Z} < 280$ GeV, C veto B veto	Sherpa	65.79	0.9374	0.6138
361451	$Z \to \nu\nu$, $140 < p_{\text{T}}^{Z} < 280$ GeV, C filter and B veto	Sherpa	65.79	0.9374	0.2390
361452	$Z \to \nu\nu$, $140 < p_{\text{T}}^{Z} < 280$ GeV, B filter	Sherpa	65.79	0.9374	0.1477
361453	$Z \to \nu\nu$, $280 < p_{\text{T}}^{Z} < 500$ GeV, C veto and B veto	Sherpa	4.847	0.9374	0.5857
361454	$Z \to \nu\nu$, $280 < p_{\text{T}}^{Z} < 500$ GeV, C filter and B veto	Sherpa	4.847	0.9374	0.2606
361455	$Z \to \nu\nu$, $280 < p_{\text{T}}^{Z} < 500$ GeV, B filter	Sherpa	4.847	0.9374	0.1617
361456	$Z \to \nu\nu$, $500 < p_{\text{T}}^{Z} < 700$ GeV, C veto and B veto	Sherpa	0.3006	0.9374	0.5550
361457	$Z \to \nu\nu$, $500 < p_{\text{T}}^{Z} < 700$ GeV, C filter and B veto	Sherpa	0.3006	0.9374	0.2749
361458	$Z \to \nu\nu$, $500 < p_{\text{T}}^{Z} < 700$ GeV, B filter	Sherpa	0.3006	0.9374	0.1649
361459	$Z \to \nu\nu$, $700 < p_{\text{T}}^{Z} < 1000$ GeV, C veto and B veto	Sherpa	0.05493	0.9374	0.5577
361460	$Z \to \nu\nu$, $700 < p_{\text{T}}^{Z} < 1000$ GeV, C filter and B veto	Sherpa	0.05493	0.9374	0.3039
361461	$Z \to \nu\nu$, $700 < p_{\text{T}}^{Z} < 1000$ GeV, B filter	Sherpa	0.05493	0.9374	0.1631
361462	$Z \to \nu\nu$, $1000 < p_{\text{T}}^{Z} < 2000$ GeV, C veto and B veto	Sherpa	0.007663	0.9374	0.5347
361463	$Z \to \nu\nu$, $1000 < p_{\text{T}}^{Z} < 2000$ GeV, C filter and B veto	Sherpa	0.007663	0.9374	0.3122
361464	$Z \to \nu\nu$, $1000 < p_{\text{T}}^{Z} < 2000$ GeV, B filter	Sherpa	0.007663	0.9374	0.1972
361465	$Z \to \nu\nu$, $p_{\text{T}}^{Z} > 2000$ GeV, C veto and B veto	Sherpa	3.402e-05	0.9374	0.5436
361466	$Z \to \nu\nu$, $p_{\text{T}}^{Z} > 2000$ GeV, C filter and B veto	Sherpa	3.402e-05	0.9374	0.3456
361467	$Z \to \nu\nu$, $p_{\text{T}}^{Z} > 2000$ GeV, B filter	Sherpa	3.402e-05	0.9374	0.2157

DS ID	Process	Generator	$\sigma \times$ BR [fb]	k-factor	ϵ_{filter}
410000	non-all-had $t\bar{t}$	Powheg+Pythia 8	377.9932	1.1949	1
410011	Single top t-chan lt	Powheg+Pythia 8	0.043739	1.0094	1
410012	Single top t-chan $l\bar{t}$	Powheg+Pythia 8	0.025778	1.0193	1
410013	Single top Wt incl t	Powheg+Pythia 8	0.034009	1.054	1
410014	Single top Wt incl $\bar{t}$	Powheg+Pythia 8	0.033989	1.054	1

Table 5: $t\bar{t}$ and single t samples used in the analysis. The dataset ID, MC generator, production crossection, k-factor and filter efficiency are shown.

DS ID	Process	Generator	$\sigma \times$ BR [fb]	k-factor	ϵ_{filter}
361063	llll	Sherpa	12.764	1.0	1.0
361064	lllvSFMinus	Sherpa	1.8442	1.0	1.0
361065	lllvOFMinus	Sherpa	3.6254	1.0	1.0
361064	lllvSFPlus	Sherpa	2.5618	1.0	1.0
361065	lllvOFPlus	Sherpa	5.0248	1.0	1.0
361066	llvv	Sherpa	14.0	1.0	1.0
361081	WplvWmqq	Sherpa	25.995	1.0	1.0
361082	WpqqWmlv	Sherpa	25.974	1.0	1.0
361083	WlvZqq	Sherpa	12.543	1.0	1.0
361084	WqqZlv	Sherpa	3.7583	1.0	1.0
361085	WqqZvv	Sherpa	7.5141	1.0	1.0
361086	ZqqZll	Sherpa	16.59	1.0	0.1425
361087	ZqqZvv	Sherpa	16.492	1.0	0.281
361088	lvvv	Sherpa	3.4001	1.0	1.0
361089	vvvv	Sherpa	0.65967	1.0	1.0

Table 6: Diboson samples used in the analysis. The dataset ID, MC generator, production crossection, k-factor and filter efficiency are shown.

B VH Resonances Auxilliary Plots

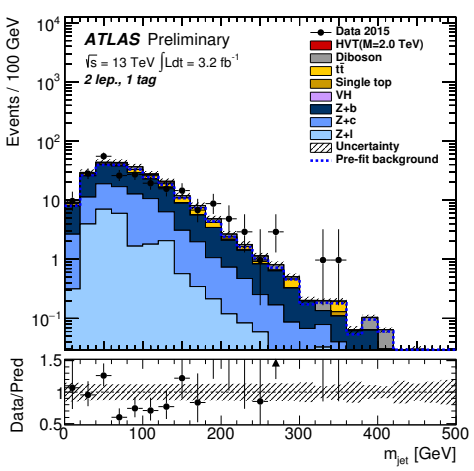

(a) 0 lepton

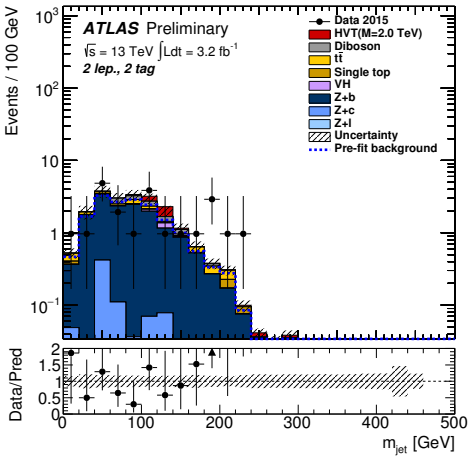

(b) 1 lepton

Figure 1: Postfit plots of the signal regions used to set limits. The blue band represents the prefit MC prediction, the signal is normalised to the 95% CL upper limit.

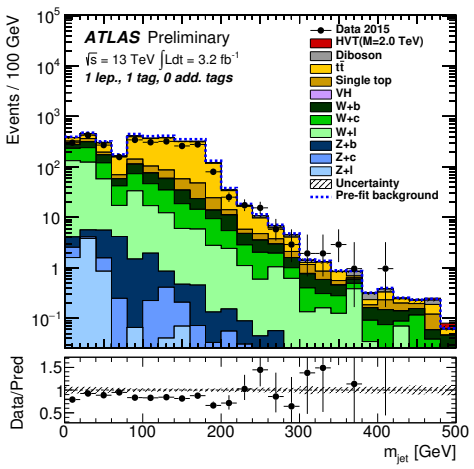

(a) 0 lepton

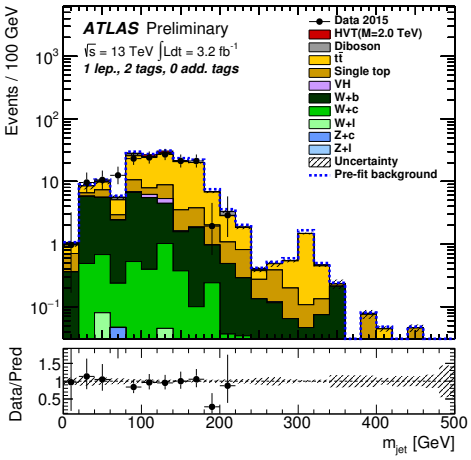

(b) 1 lepton

Figure 2: Postfit plots of the signal regions used to set limits. The blue band represents the prefit MC prediction, the signal is normalised to the 95% CL upper limit.

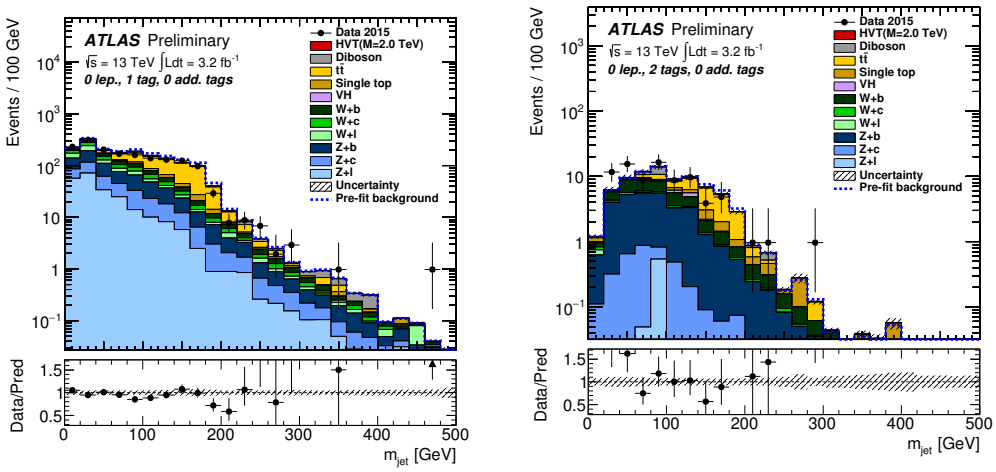

(a) 0 lepton

(b) 1 lepton

Figure 3: Postfit plots of the signal regions used to set limits. The blue band represents the prefit MC prediction, the signal is normalised to the 95% CL upper limit.

C Hbb Analysis Auxilliary Plots

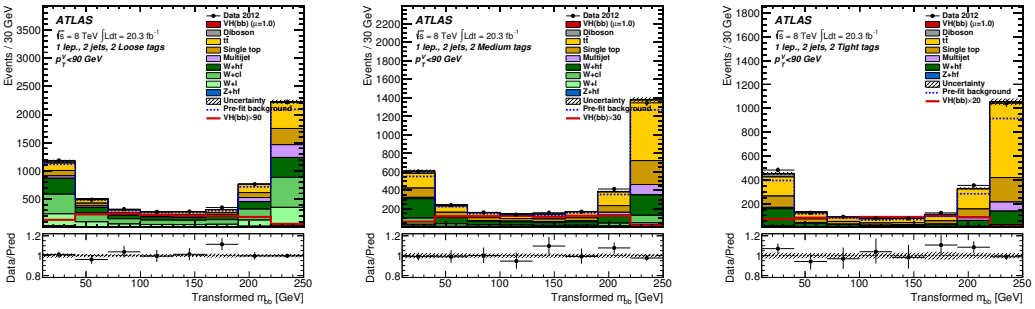

Figure 4: Postfit transformed dijet mass distribution in the 2 jet, $0 < p_T^W < 90$ region with 2L tag (left), 2M tag (middle) and 2T tag (left) jets. The dashed blue line represents the prefit background estimation.

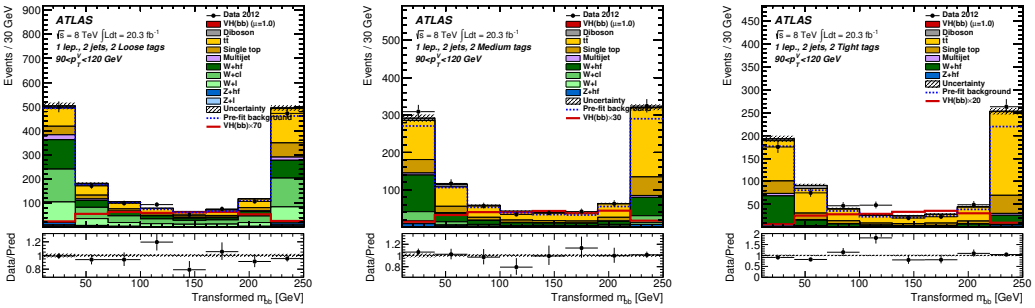

Figure 5: Transformed dijet mass distribution in the 2 jet, $90 < p_T^W < 120$ region with 2L tag (left), 2M tag (middle) and 2T tag (left) jets. The dashed blue line represents the prefit background estimation.

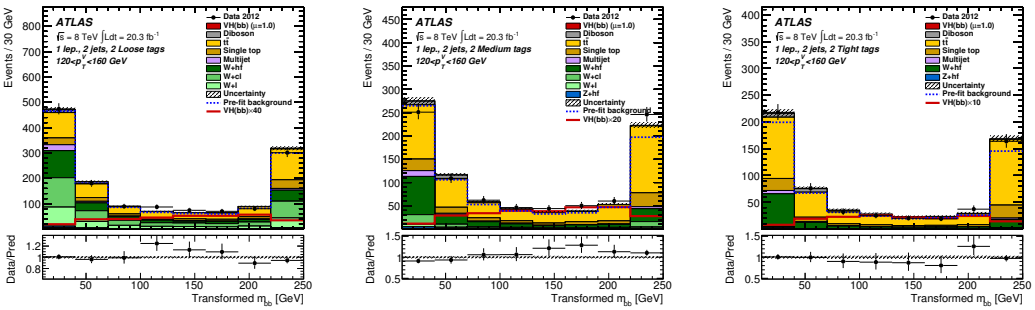

Figure 6: Transformed dijet mass distribution in the 2 jet, $120 < p_T^W < 160$ region with 2L tag (left), 2M tag (middle) and 2T tag (left) jets. The dashed blue line represents the prefit background estimation.

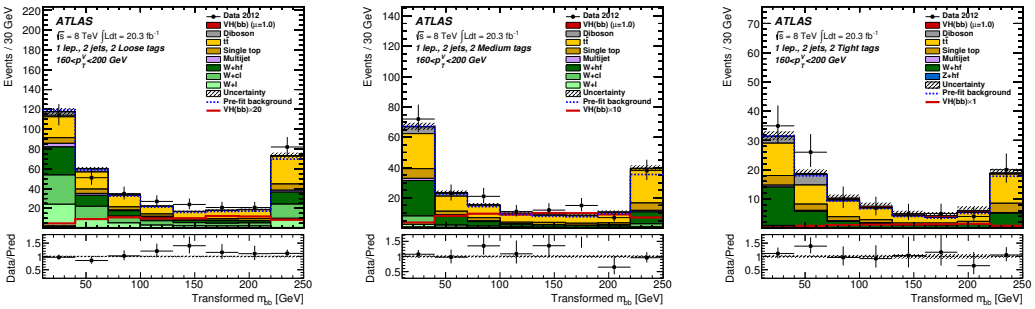

Figure 7: Transformed dijet mass distribution in the 2 jet, $160 < p_T^W < 200$ region with 2L tag (left), 2M tag (middle) and 2T tag (left) jets. The dashed blue line represents the prefit background estimation.

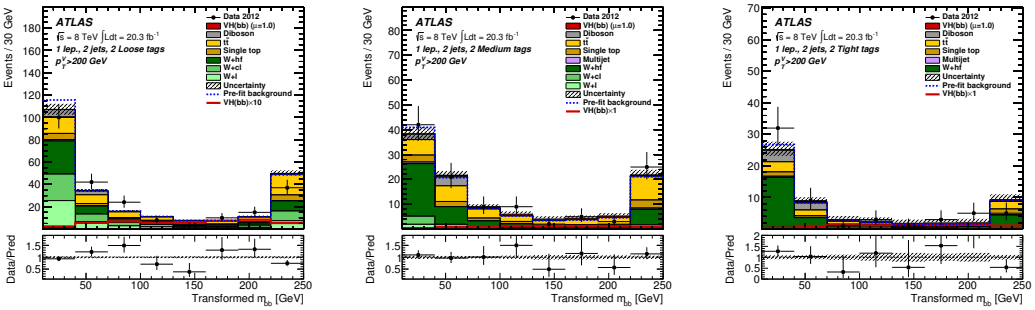

Figure 8: Transformed dijet mass distribution in the 2 jet, $p_T^W > 200$ region with 2L tag (left), 2M tag (middle) and 2T tag (left) jets. The dashed blue line represents the prefit background estimation.

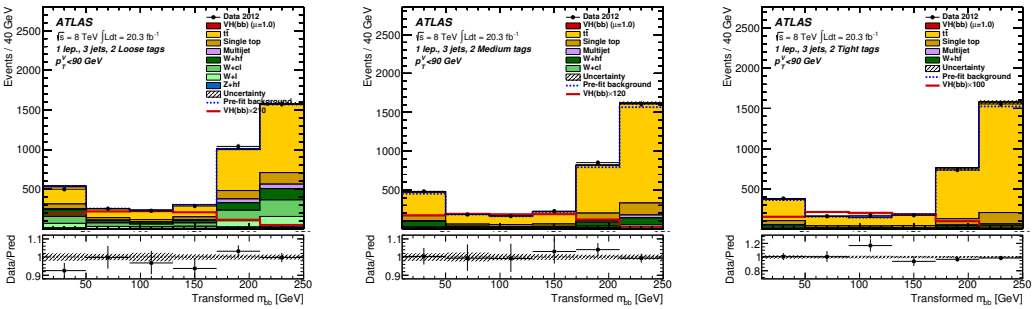

Figure 9: Postfit transformed dijet mass distribution in the 3 jet, $0 < p_T^W < 90$ region with 2L tag (left), 2M tag (middle) and 2T tag (right) jets. The dashed blue line represents the prefit background estimation.

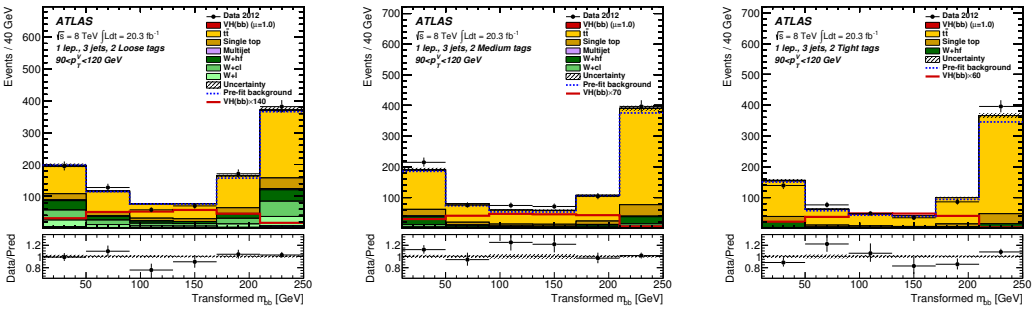

Figure 10: Transformed dijet mass distribution in the 3 jet, $90 < p_T^W < 120$ region with 2L tag (left), 2M tag (middle) and 2T tag (right) jets. The dashed blue line represents the prefit background estimation.

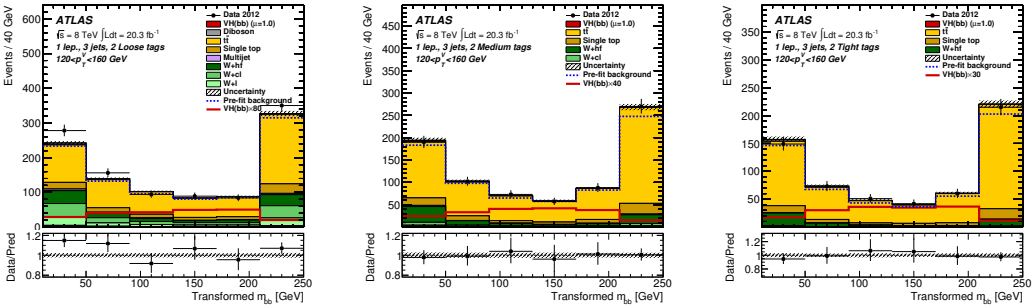

Figure 11: Transformed dijet mass distribution in the 3 jet, $120 < p_T^W < 160$ region with 2L tag (left), 2M tag (middle) and 2T tag (right) jets. The dashed blue line represents the prefit background estimation.

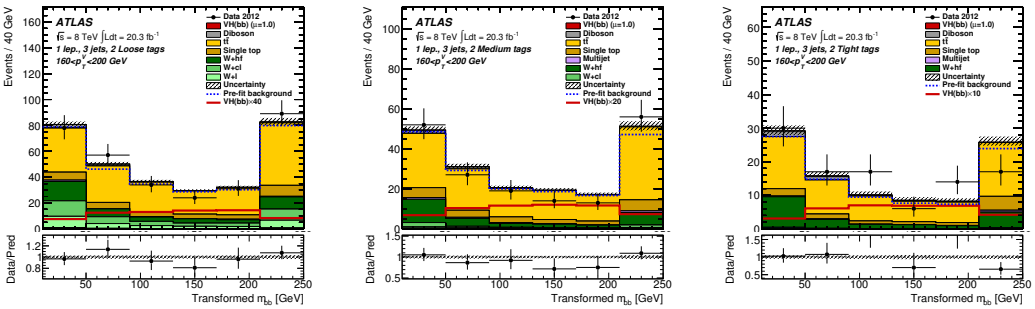

Figure 12: Transformed dijet mass distribution in the 3 jet, $160 < p_T^W < 200$ region with 2L tag (left), 2M tag (middle) and 2T tag (right) jets. The dashed blue line represents the prefit background estimation.

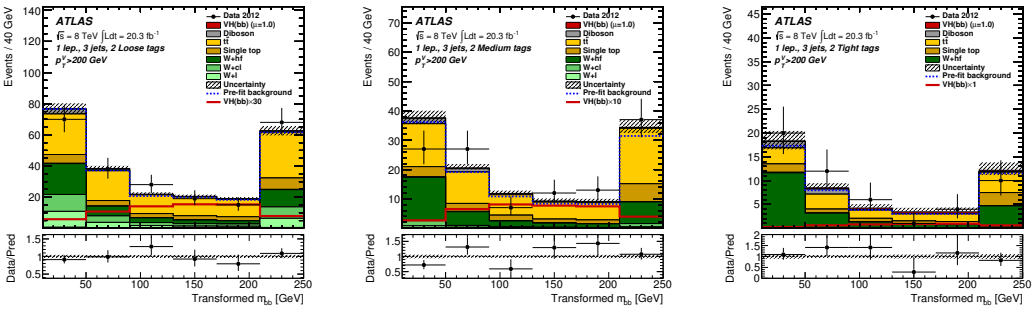

Figure 13: Transformed dijet mass distribution in the 3 jet, $p_T^W > 200$ region with 2L tag (left), 2M tag (middle) and 2T tag (right) jets. The dashed blue line represents the prefit background estimation.

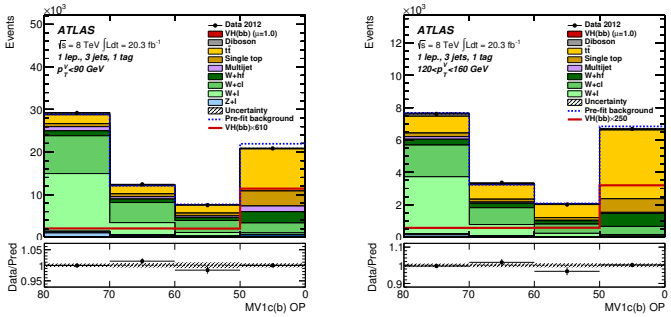

Figure 14: Postfit transformed MV1c distribution in the 2 jet, 1 tag region with $p_T^W < 120$ (left) and $p_T^W > 120$ (right). The dashed blue line represents the prefit background estimation.

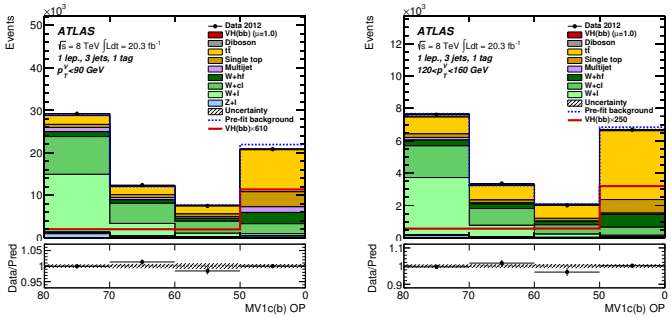

Figure 15: Postfit transformed MV1c distribution in the 3 jet, 1 tag region with $p_T^W < 120$ (left) and $p_T^W > 120$ (right). The dashed blue line represents the prefit background estimation.

Bibliography

[1] Tilman Plehn. Lectures on LHC Physics. *Lect. Notes Phys.*, 844:1–193, 2012.

[2] J R Andersen et al. Handbook of LHC Higgs Cross Sections: 3. Higgs Properties. 2013.

[3] W.J. Stirling. private communication.

[4] A. D. Martin, W. J. Stirling, R. S. Thorne, and G. Watt. Parton distributions for the LHC. *Eur. Phys. J.*, C63:189–285, 2009.

[5] Christiane Lefvre. The CERN accelerator complex. Complexe des acclrateurs du CERN technical report. Dec 2008.

[6] Atlas luminosity public results. `https://twiki.cern.ch/twiki/bin/view/AtlasPublic/LuminosityPublicResults`. Accessed: 2016-02-16.

[7] Atlas luminosity public results run 2. `https://twiki.cern.ch/twiki/bin/view/AtlasPublic/LuminosityPublicResultsRun2`. Accessed: 2016-02-16.

[8] Georges Aad et al. The ATLAS Experiment at the CERN Large Hadron Collider. *J. Instrum.*, 3:S08003. 437 p, 2008.

[9] M Capeans, G Darbo, K Einsweiller, M Elsing, T Flick, M Garcia-Sciveres, C Gemme, H Pernegger, O Rohne, and R Vuillermet. ATLAS Insertable B-Layer Technical Design Report. Technical Report CERN-LHCC-2010-013. ATLAS-TDR-19, CERN, Geneva, Sep 2010.

[10] Electron efficiency measurements with the ATLAS detector using the 2012 LHC proton-proton collision data. Technical Report ATLAS-CONF-2014-032, CERN, Geneva, Jun 2014.

[11] Georges Aad et al. Measurement of the muon reconstruction performance of the ATLAS detector using 2011 and 2012 LHC protonproton collision data. *Eur. Phys. J.*, C74(11):3130, 2014.

[12] Monte Carlo Calibration and Combination of In-situ Measurements of Jet Energy Scale, Jet Energy Resolution and Jet Mass in ATLAS. Technical Report ATLAS-CONF-2015-037, CERN, Geneva, Aug 2015.

[13] Jet global sequential corrections with the ATLAS detector in proton-proton collisions at sqrt(s) = 8 TeV. Technical Report ATLAS-CONF-2015-002, CERN, Geneva, Mar 2015.

[14] Jason Veatch, Benjamin Philip Nachman, and Ruchika Nayyar. Measurement of the jet mass scale and resolution uncertainty for large radius jets at $\sqrt{s}$ = 8 TeV using the ATLAS detector. Technical Report ATLAS-COM-CONF-2016-001, CERN, Geneva, Jan 2015. The original COM-PHYS discussion can be found here: https://cds.cern.ch/record/2110972/comments?ln=en.

[15] Calibration of the performance of b-tagging for c and light-flavour jets in the 2012 ATLAS data. Technical Report ATLAS-CONF-2014-046, CERN, Geneva, Jul 2014.

[16] Calibration of b-tagging using dileptonic top pair events in a combinatorial likelihood approach with the ATLAS experiment. Technical Report ATLAS-CONF-2014-004, CERN, Geneva, Feb 2014.

[17] Expected performance of the ATLAS b-tagging algorithms in Run-2. Technical Report ATL-PHYS-PUB-2015-022, CERN, Geneva, Jul 2015.

[18] Expected performance of missing transverse momentum reconstruction for the ATLAS detector at $\sqrt{s} = 13$ TeV. Technical Report ATL-PHYS-PUB-2015-023, CERN, Geneva, Jul 2015.

[19] K. A. Olive et al. Review of Particle Physics. *Chin. Phys.*, C38:090001, 2014.

[20] F Ahmadov, AM Da Palma, L Alio, BMM Allbrooke, T Bristow, D Buescher, A Buzatu, Y Coadou, P Conde Muio, C Debenedetti, Y Enari, G Facini, W Fisher, P Francavilla, G Gaycken, J Gentil, R Goncalo, G Gonzalez Parra, HM Gray, JF Grivaz, C Gwilliam, S Hageboeck, G Halladjian, M Jackson, D Jamin, R Jansky, K Kiuchi, V Kostyukhin, K Lohwasser, D Lopez Mateos, U Mallik, J Maneira, G Marchiori, M Martinez Perez, A Mehta, K Mercurio, K Mochizuki, N Morange, Y Ming, P Mullen, Y Nagai, J Nielsen, I Ochoa, A Palma, C Pandini, R Pedro, G Piacquadio, M Proissl, T Ravenscroft, P Rose, T Scanlon, E Schopf, S Shaw, B Smart, V Sorin, M Sousa, F Sforza, J Therhaag, PD Thompson, L Vacavant, J Wang, C Wang, S Wang, C Weiser, R Zaidan, and L Zhang. Supporting Document for the Search for

the bb decay of the Standard Model Higgs boson in associated (W/Z)H production with the ATLAS detector. Technical Report ATL-COM-PHYS-2014-051, CERN, Geneva, Jan 2014.

[21] Michael E Peskin and Daniel V Schroeder. *An Introduction to Quantum Field Theory; 1995 ed.* Westview, Boulder, CO, 1995. Includes exercises.

[22] Emmy Noether and M. A. Tavel. Invariant variation problems. 1918.

[23] Jun John Sakurai. *Modern quantum mechanics; rev. ed.* Addison-Wesley, Reading, MA, 1994.

[24] Kaustubh Agashe, Roberto Contino, and Alex Pomarol. The Minimal composite Higgs model. *Nucl.Phys.*, B719:165–187, 2005.

[25] Duccio Pappadopulo, Andrea Thamm, Riccardo Torre, and Andrea Wulzer. Heavy Vector Triplets: Bridging Theory and Data. *JHEP*, 09:060, 2014.

[26] John C. Collins, Davison E. Soper, and George F. Sterman. Factorization of Hard Processes in QCD. *Adv. Ser. Direct. High Energy Phys.*, 5:1–91, 1989.

[27] Richard Keith Ellis, William James Stirling, and Bryan R Webber. *QCD and Collider Physics*. Cambridge monographs on particle physics, nuclear physics, and cosmology. Cambridge Univ. Press, Cambridge, 2003. Photography by S. Vascotto.

[28] M. A. Dobbs, S. Frixione, E. Laenen, K. Tollefson, H. Baer, E. Boos, B. Cox, R. Engel, W. Giele, J. Huston, S. Ilyin, B. Kersevan, F. Krauss, Y. Kurihara, L. Lonnblad, F. Maltoni, M. Mangano, S. Odaka, P. Richardson, A. Ryd, T. Sjostrand, P. Skands, Z. Was, B. R. Webber, and D. Zeppenfeld. Les

houches guidebook to monte carlo generators for hadron collider physics, 2004.

[29] Georges Aad et al. Observation of a new particle in the search for the Standard Model Higgs boson with the ATLAS detector at the LHC. *Phys. Lett.*, B716:1–29, 2012.

[30] Georges Aad et al. Combined Measurement of the Higgs Boson Mass in pp Collisions at $\sqrt{s} = 7$ and 8 TeV with the ATLAS and CMS Experiments. *Phys. Rev. Lett.*, 114:191803, 2015.

[31] Georges Aad et al. Study of the spin and parity of the Higgs boson in diboson decays with the ATLAS detector. *Eur. Phys. J.*, C75(10):476, 2015. [Erratum: Eur. Phys. J.C76,no.3,152(2016)].

[32] Georges Aad et al. Observation and measurement of Higgs boson decays to WW* with the ATLAS detector. *Phys. Rev.*, D92(1):012006, 2015.

[33] Georges Aad et al. Search for a new resonance decaying to a W or Z boson and a Higgs boson in the $\ell\ell/\ell\nu/\nu\nu+b\bar{b}$ final states with the ATLAS detector. *Eur. Phys. J.*, C75(6):263, 2015.

[34] Search for massive WH resonances decaying to $\ell\nu\mathrm{b\bar{b}}$ final state in the boosted regime at $\sqrt{s} = 8\,\mathrm{TeV}$. Technical Report CMS-PAS-EXO-14-010, CERN, Geneva, 2015.

[35] Lyndon R Evans and Philip Bryant. LHC Machine. *J. Instrum.*, 3:S08001. 164 p, 2008. This report is an abridged version of the LHC Design Report (CERN-2004-003).

[36] Georges Aad et al. Performance of the ATLAS Trigger System in 2010. *Eur. Phys. J.*, C72:1849, 2012.

[37] G. Aad et al. The ATLAS Simulation Infrastructure. *Eur. Phys. J.*, C70:823–874, 2010.

[38] S. Agostinelli et al. GEANT4: A Simulation toolkit. *Nucl. Instrum. Meth.*, A506:250–303, 2003.

[39] Kathryn Grimm, Federico Meloni, Simone Pagan Griso, Kirill Prokofiev, Matthew Scott Rudolph, Andreas Wildauer, and David Ren-hwa Yu. Reconstruction of primary vertices in Run I proton-proton collisions at the LHC. Technical Report ATL-COM-INDET-2015-004, CERN, Geneva, Jan 2015. Support note for ATL-COM-INDET-2015-002.

[40] The Optimization of ATLAS Track Reconstruction in Dense Environments. Technical Report ATL-PHYS-PUB-2015-006, CERN, Geneva, Mar 2015.

[41] Performance of the ATLAS Electron and Photon Trigger in p-p Collisions at sqrts = 7 TeV in 2011. Technical Report ATLAS-CONF-2012-048, CERN, Geneva, May 2012.

[42] Georges Aad et al. Electron reconstruction and identification efficiency measurements with the ATLAS detector using the 2011 LHC proton-proton collision data. *Eur. Phys. J.*, C74(7):2941, 2014.

[43] Improved electron reconstruction in ATLAS using the Gaussian Sum Filter-based model for bremsstrahlung. Technical Report ATLAS-CONF-2012-047, CERN, Geneva, May 2012.

[44] Georges Aad et al. Performance of the ATLAS muon trigger in pp collisions at $\sqrt{s} = 8$ TeV. *Eur. Phys. J.*, C75:120, 2015.

[45] Peter Loch, Sven Menke, Pierre-Antoine Delsart, Christopher John Young, Zach Marshall, and Bradley Axen. Topological cell clustering in the ATLAS calorimeters and its performance in LHC Run I. Technical Report ATL-COM-PHYS-2014-1439, CERN, Geneva, Nov 2014.

[46] Matteo Cacciari, Gavin P. Salam, and Gregory Soyez. The Anti-k(t) jet clustering algorithm. *JHEP*, 04:063, 2008.

[47] Identification of boosted, hadronically-decaying W and Z bosons in $\sqrt{s} = 13$ TeV Monte Carlo Simulations for ATLAS. Technical Report ATL-PHYS-PUB-2015-033, CERN, Geneva, Aug 2015.

[48] Georges Aad et al. Performance of jet substructure techniques for large-R jets in proton-proton collisions at $\sqrt{s} = 7$ TeV using the ATLAS detector. *JHEP*, 09:076, 2013.

[49] Flavor Tagging with Track Jets in Boosted Topologies with the ATLAS Detector. Technical Report ATL-PHYS-PUB-2014-013, CERN, Geneva, Aug 2014.

[50] Matteo Cacciari and Gavin P. Salam. Pileup subtraction using jet areas. *Phys. Lett.*, B659:119–126, 2008.

[51] Matteo Cacciari, Gavin P. Salam, and Gregory Soyez. The Catchment Area of Jets. *JHEP*, 04:005, 2008.

[52] Georges Aad et al. Characterisation and mitigation of beam-induced backgrounds observed in the ATLAS detector during the 2011 proton-proton run. *JINST*, 8:P07004, 2013.

[53] Bogdan Malaescu, Dag Ingemar Gillberg, Michael Begel, Reina Camacho Toro, Joe Taenzer, James Lacey, Sabine Lammers, David Lopez Mateos, Cigdem Issever, Zach Marshall, Andrew Pilkington, Frederik Ruehr, Craig Sawyer, Pavel Starovoitov, Michel Vetterli, and Christopher John Young. Determination of jet calibration and energy resolution in proton-proton collisions at $\sqrt{s} = 8$ TeV using the ATLAS detector. Technical Report ATL-COM-PHYS-2015-1086, CERN, Geneva, Sep 2015.

[54] Commissioning of the ATLAS high-performance b-tagging algorithms in the 7 TeV collision data. Technical Report ATLAS-CONF-2011-102, CERN, Geneva, Jul 2011.

[55] M Bellomo, N Bruscino, G Brooijmans, D Duda, Y Enari, F Filthaut, S Fleischmann, M Kagan, T Kawamoto, A Kobayashi, P Mattig, T Scanlon, A Schwartzman, N Tannoury, E Thompson, W Van Den Wollenberg, Q Zeng, and L Zhou. Flavor Tagging with Track Jets in Boosted Topologies with the ATLAS Detector. Technical Report ATL-COM-PHYS-2014-752, CERN, Geneva, Jun 2014.

[56] Search for Diphoton Events with Large Missing Transverse Momentum in 8 TeV pp Collision Data with the ATLAS Detector. Technical Report ATLAS-CONF-2014-001, CERN, Geneva, Jan 2014.

[57] Georges Aad et al. Search for the $b\bar{b}$ decay of the Standard Model Higgs boson in associated $(W/Z)H$ production with the ATLAS detector. *JHEP*, 01:069, 2015.

[58] Duccio Pappadopulo, Andrea Thamm, Riccardo Torre, and Andrea Wulzer. Heavy Vector Triplets: Bridging Theory and Data. *JHEP*, 09:060, 2014.

[59] J. Alwall, R. Frederix, S. Frixione, V. Hirschi, F. Maltoni, O. Mattelaer, H. S. Shao, T. Stelzer, P. Torrielli, and M. Zaro. The automated computation of tree-level and next-to-leading order differential cross sections, and their matching to parton shower simulations. *JHEP*, 07:079, 2014.

[60] Torbjorn Sjostrand, Stephen Mrenna, and Peter Z. Skands. A Brief Introduction to PYTHIA 8.1. *Comput. Phys. Commun.*, 178:852–867, 2008.

[61] T. Gleisberg, Stefan. Hoeche, F. Krauss, M. Schonherr, S. Schumann, F. Siegert, and J. Winter. Event generation with SHERPA 1.1. *JHEP*, 02:007, 2009.

[62] Kirill Melnikov and Frank Petriello. Electroweak gauge boson production at hadron colliders through O(alpha(s)**2). *Phys. Rev.*, D74:114017, 2006.

[63] Hung-Liang Lai, Marco Guzzi, Joey Huston, Zhao Li, Pavel M. Nadolsky, Jon Pumplin, and C. P. Yuan. New parton distributions for collider physics. *Phys. Rev.*, D82:074024, 2010.

[64] Paolo Nason. A New method for combining NLO QCD with shower Monte Carlo algorithms. *JHEP*, 11:040, 2004.

[65] Stefano Frixione, Paolo Nason, and Carlo Oleari. Matching NLO QCD computations with Parton Shower simulations: the POWHEG method. *JHEP*, 11:070, 2007.

[66] Simone Alioli, Paolo Nason, Carlo Oleari, and Emanuele Re. A general framework for implementing NLO calculations in shower Monte Carlo programs: the POWHEG BOX. *JHEP*, 06:043, 2010.

[67] J. Pumplin, D. R. Stump, J. Huston, H. L. Lai, Pavel M. Nadolsky, and W. K. Tung. New generation of parton distributions with uncertainties from global QCD analysis. *JHEP*, 07:012, 2002.

[68] Micha Czakon, Paul Fiedler, and Alexander Mitov. Total Top-Quark Pair-Production Cross Section at Hadron Colliders Through $O(\frac{4}{S})$. *Phys. Rev. Lett.*, 110:252004, 2013.

[69] Nikolaos Kidonakis. Next-to-next-to-leading-order collinear and soft gluon corrections for t-channel single top quark production. *Phys. Rev.*, D83:091503, 2011.

[70] John M. Campbell and R. K. Ellis. MCFM for the Tevatron and the LHC. *Nucl. Phys. Proc. Suppl.*, 205-206:10–15, 2010.

[71] David Krohn, Jesse Thaler, and Lian-Tao Wang. Jet Trimming. *JHEP*, 02:084, 2010.

[72] W.J. Stirling. private communication.

[73] Andreas Hoecker, Peter Speckmayer, Joerg Stelzer, Jan Therhaag, Eckhard von Toerne, and Helge Voss. TMVA: Toolkit for Multivariate Data Analysis. *PoS*, ACAT:040, 2007.

[74] Identification of boosted, hadronically-decaying W and Z bosons in $\sqrt{s} = 13$ TeV Monte Carlo Simulations for ATLAS. Technical Report ATL-PHYS-PUB-2015-033, CERN, Geneva, Aug 2015.

[75] Georges Aad et al. Performance of b-Jet Identification in the ATLAS Experiment. 2015.

[76] Georges Aad et al. Measurements of the W production cross sections in association with jets with the ATLAS detector. *Eur. Phys. J.*, C75(2):82, 2015.

[77] Georges Aad et al. Measurement of the differential cross-section of highly boosted top quarks as a function of their transverse momentum in $\sqrt{s} =$ 8 TeV proton-proton collisions using the ATLAS detector. *Phys. Rev.*, D93(3):032009, 2016.

[78] Glen Cowan, Kyle Cranmer, Eilam Gross, and Ofer Vitells. Asymptotic formulae for likelihood-based tests of new physics. *Eur. Phys. J.*, C71:1554, 2011. [Erratum: Eur. Phys. J.C73,2501(2013)].

[79] Kyle Cranmer, George Lewis, Lorenzo Moneta, Akira Shibata, and Wouter Verkerke. HistFactory: A tool for creating statistical models for use with RooFit and RooStats. Technical Report CERN-OPEN-2012-016, New York U., New York, Jan 2012.